Vibrational Dynamics in Water From the Molecule's Perspective

by

Joel David Eaves

Submitted to the Department of Chemistry
in partial fulfillment of the requirements for the degree of

Doctor of Philosophy

at the

MASSACHUSETTS INSTITUTE OF TECHNOLOGY

February 2005

Author .....
Department of Chemistry
November 12, 2004

Certified by .....
Andrei Tokmakoff
Associate Professor
Thesis Supervisor

Accepted by .....
Robert W. Field
Chairman, Departmental Committee on Graduate Students

Vibrational Dynamics in Water From the Molecule's Perspective

by

Joel David Eaves

Submitted to the Department of Chemistry
on November 12, 2004, in partial fulfillment of the
requirements for the degree of
Doctor of Philosophy

Abstract

Liquid water is a fascinating substance, ubiquitous in chemistry, physics, and biology. Its remarkable physical and chemical properties stem from the intricate network of hydrogen bonds that connect molecular participants. The structures and energetics of the network can explain the physical properties of the substance on macroscopic length scales, but the events that initiate many chemical reactions in water occur on the time scales of $\approx 0.1 - 1$ picosecond. The experimental challenges of measuring specific molecular motions on this time scale are formidable.

The absorption frequency of the OH stretch of HOD in liquid D_2O is sensitive to the hydrogen bonding and molecular environment of the liquid. Ultrafast IR experiments endeavor to measure fluctuations in the hydrogen bond network by measuring spectral fluctuations on femtosecond time scales, but the data do not easily lend themselves to a direct microscopic interpretation. Computer simulations of empirical models, however, offer explicit microscopic detail but must be adapted to include a quantum mechanical vibration. I have developed methods in computer simulation to relate spectral fluctuations of the OH stretch in liquid D_2O to explicit microscopic information. The experiments also inform the simulation by providing important quantitative data about the fidelity and accuracy of a chosen molecular model, and help build a qualitative picture of hydrogen bonding in water.

Our atomistic model reveals that ultrafast experiments of HOD in liquid D_2O measure transient fluctuations of the liquid's electric field. On the fastest time scales, localized fluctuations drive dephasing, while on longer time scales larger scale molecular reorganization destroys vibrational coherence. Because electric fields drive vibrational dephasing, the frequency of the OH stretch is particularly sensitive to the microscopic details of the molecular potential. With collaborators, I have examined the accuracy of emerging fluctuating charge models for water and the role that molec-

ular polarizability plays in the vibrational spectroscopy.

In liquid water at ambient conditions, roughly 90 % of the hydrogen bonds are intact. I have examined the fates and the fundamental chemical nature of the remaining 10 % of the "broken" hydrogen bonds. We consider two reaction mechanisms that describe how hydrogen bonds change partners. In the first scenario, broken hydrogen bonds exist in stable chemical equilibrium with intact hydrogen bonds. In an alternate scenario, the broken hydrogen bond is not a meta-stable chemical state but instead a species that molecules visit during natural equilibrium fluctuations or when trading hydrogen bonding partners. I show how the methods of condensed phase reaction dynamics can be directly applied to vibrational spectroscopy of reactive systems and how experimental 2D IR spectra can distinguish between the two mechanistic scenarios. Our data support the notion that broken hydrogen bonds are an intrinsically unstable species in water and return to form hydrogen bonds on the time scale of intermolecular motions.

Thesis Supervisor: Andrei Tokmakoff
Title: Associate Professor

Acknowledgments

I happened upon science almost by accident, and have been guided to success by many wonderful and supportive people. I extend my gratitude to these exceptional individuals who have enriched my life. My parents, John and Linda Eaves, are two of the most compassionate and intelligent people I have ever met. Ever since I was old enough to ask "why?," they indulged my curiosity and nurtured my inquisitive spirit. I am fortunate to have inherited at least some of my father's remarkable scientific talents.

I am privileged to have learned from many gifted mentors. My high school chemistry teacher, who dubbed me a "physical chemist" when I was 17, piqued my interest in chemistry. I recall my time at the University of Wisconsin fondly. Here I learned from many gifted professors, particularly Fleming Crim, Jim Skinner, Ned Sibert, Dieter Zeppenfeld, Thad Walker, Jean-Marc Vanden-Broeck, and Alexander Nagel. Fleming Crim, my undergraduate advisor, has been a wonderful mentor and singular human being. I gratefully acknowledge the many opportunities that he has offered me. While a member of his group, I learned from him and his many graduate students and post–docs, particularly Christopher Cheatum and Dieter Bingemann, who taught me how to formulate scientific questions and fostered my physical intuition. Andrei Tokmakoff, my Ph.D. advisor, has been a great source of creative ideas and an outstanding teacher. His bold approach to science has been refreshing and inspiring. The Tokmakoff group has been an amazing place to work and do science. I have learned something from every member of the group, but am particularly grate-

ful of the conversations I have had and the discoveries I have made with Christopher Fecko and Joseph Loparo. Phillip Geissler, the most geographically distant member of "Team Water," has had a profound influence on my life and development as a scientist. He has taught me many invaluable practical and fundamental lessons, and has become a fast friend.

I gratefully acknowledge the support of my closest friends, Andrew Low, Isaac Sparks, Arianna Melzger, Allin Chung, Joe Loparo, Reed Arnos, Effie Tsu, Darius Torchinsky and my sister Emily, who never quite rolled their eyes when I needed to express my frustration in my characteristically sardonic tones. I am also thankful for the love and support that Jessica Masarek has given me over many years. Lastly, I would like to thank my grandmother, Fay Burns, who would have taken great pleasure in knowing that she had passed on some of her earnest and discipline to her grandson.

Contents

List of Figures

List of Tables

Chapter 1

Introduction

"Whiskey is for drinking. Water is for fighting over."

– Mark Twain, in a prophetic memorandum to the water community

1.1 Water is a prickly pear

Felix Franks once said, "Out of all the known liquids, water is probably the most studied and least understood." [3] That oft-quoted punctual phrase is the sound-bite version of what drives an active community of researchers and the research ideas explored in this thesis. The Gordon Research Conference on water is a biennial August meeting that draws the crowds from all over the world to Holderness, New Hampshire so that scientists can spend a week sharing their ideas and research on water. While this conference may sound like an Eden of scientific indulgement, as it turns out, the water community is a shark pond. The water conference is a grueling meeting, punctuated by vigorous theatrical discussions and stentorian arguments that

feature the most prominent names in experimental and theoretical physical chemistry. As an observer I have noted that this conference, and indeed the study of water, seems to bring out the worst in people.

The reason why water is the center of a competitive research environment is that, even after millennia of philosophical pondering and rigorous scientific inquiry there are still important but unanswered questions about the physical and chemical properties of liquid water. Detailed questions about how water solvates reactants and products in chemical reactions and how it interacts with proteins and nucleic acids form contemporary areas of research that straddle fields of biology, chemistry, and physics. The answer to such fundamental questions will help us not only predict how chemical and physical change occurs in water, but will also provide a better understanding of the microscopic beginnings of life on earth.

1.2 A rebel in the family of liquids

Comparing water to "normal" or simple liquids is a bit like comparing the behavior of chimpanzees to (most) human beings. Unlike most liquids, liquid water expands when it freezes, solvates most chemicals but repels oil, flows more freely when squeezed, and has an anomalously high melting and boiling point for a low molecular weight substance. These phenomena have a common microscopic origin. In most liquids, the mutual repulsion of atoms and molecules determine the structure of the liquid, but in water the mutual attractions between molecules are what dominate.

The hydrogen bond was conceived in the early part of the 20^{th} century. Mau-

rice Huggins, an undergraduate in Gilbert Lewis' lab, proposed a strong attraction between oxygen and hydrogen atoms to account for an aspect of bonding in organic chemistry [3]. Lewis invented the phrase "hydrogen bond" to describe these connections that were an order of magnitude stronger than typical intermolecular attractions ($\approx$ 1 kJ/mol) but not as strong as covalent bonds ($\approx$ 100-1000 kJ/mol). Two of Lewis' colleagues, Latimer and Rodebush, thought that the hydrogen bond might be the origin of water's mysterious properties. In his seminal work on chemical bonding [1], the great chemist Linus Pauling theorized that the majority of the bonding strength for the hydrogen bond in water was primarily electrostatic, and not derived by partial electron sharing.

Hydrogen bonds between water molecules are the intricate and specific connections that give the substance its unique physical and chemical properties. At ambient conditions, water molecules readily form hydrogen bonds. Each molecule can donate two hydrogen bonds, one for each hydrogen, and accept two hydrogen bonds to the oxygen atom. The water molecules sit at the vertex of linked tetrahedra. The tetrahedral architecture of hydrogen bond connections is nearly unique to water and permits an extended network of hydrogen bond connections to extend throughout space [19]. The structure of simple liquids looks similar to that of a dense gas, but the structure of liquid water, at least locally, bears more resemblance to that of a crystal.

[1] *The Nature of the Chemical Bond* (1939)

1.3 Adventures *in silico*

Molecular dynamics simulations (MD) have been indispensable tools that connect experimentally observed phenomena to their microscopic origins. MD simulations are a computer model of the microscopic world that gives the researcher direct access to atomistic detail. In MD simulations, one solves for the equations of motion for atoms interacting through an empirical potential energy. In a corollary to Pauling's picture of the hydrogen bond, conventional water potentials represent the forces of hydrogen bonding with pure electrostatics. The virtues of MD simulations were evident early in the history of computer simulation, when Rahman and Stillinger [17] performed the first MD simulations of liquid water. From their simulations, they computed many available experimental quantities with remarkable quantitative accuracy. More importantly, the obvious microscopic detail provided a qualitative picture for the structure of water. At the time these simulations were done, there were competing ideas for the structure of liquid water that all made consistent predictions with available thermodynamic, x-ray and neutron scattering data [6]. The "mixture models" envisioned the structure of the liquid as a heterogeneous mixture of molecular icebergs floating in a sea of broken hydrogen bonds. The "distorted" or "random network" models accounted for the difference between the liquid and solid by conjecturing that the liquid maintains a similar hydrogen bond structure to ice, but that these bonds are frequently distorted and deformed. Stillinger's [19] simulations showed, in no uncertain terms, that the random network models provided a qualitatively accurate picture of water.

1.4 The liquid state speed record

One reason why the mixture models and random network models of water were consistent with available experimental data is that few of these data are sensitive to the motions of individual water molecules. The hydrogen bond network is pliable and the intermolecular dynamics are fast. For example, librations, or frustrated rotations of molecules hold the liquid state speed record with a period of $\approx$ 60 femtoseconds (fs) [2]. Intermolecular motions of most liquids at ambient conditions are considerably slower ($\approx$ 0.5-1 picosecond (ps)).

In the last decade, advances in ultrafast laser technology have made time scales on the order of 10 fs directly accessible to experiments. In an ultrafast experiment, one prepares a dilute solution of a probe molecule in the liquid host. The absorption frequency of the probe molecule is sensitive to the liquid's molecular environment. Ultrafast spectroscopies of liquids typically use three coherent laser pulses separated by controlled time delays to measure how the absorption frequency changes as the liquid undergoes natural equilibrium fluctuations. This phenomenon is called "spectral diffusion," because the absorption frequency of the probe molecule appears to undergo a stochastic walk commensurate with the environmental fluctuations. Ultrafast experiments that use three pulses to interrogate the liquid are called called third-order nonlinear spectroscopies, and they can observe changes in the molecular environment on the time scale of $\approx$ 100 fs – close to the time scale of the fastest in-

[2] In H_2O, the librations show a resonance at $\approx 600\ cm^{-1}$, which is higher than $k_BT = 200\ cm^{-1}$ at room temperature. For some observables, the quantum mechanics of the librations becomes important.

termolecular motions. Solvation dynamics experiments in water, for example, study how water solvates a dye molecule. Upon electronic excitation the dye molecule enters a new electronic state with a different charge distribution than the ground state. The water solvent reorganizes around the new charge distribution, and the absorption frequency changes as the solvent reorganizes. Solvation dynamics experiments have revealed that the librations of water molecules play a critical role in solvation, dissipating nearly 60-70 % of the excess solvation energy within $\approx$ 100 fs [7, 10].

1.5 The molecule's perspective

Solvation dynamics studies elucidate solvation properties in water but do so by inferring how the solvent reorganizes around an extrinsic probe. Often the chromophore molecule is much larger than a water molecule and the excited electronic state is delocalized, so the solvent motions these experiments probe are not particularly sensitive to the motions of individual molecules in hydrogen bonds. In a dilute solution of HOD in liquid D_2O, the HOD molecule becomes a native molecular probe – a way to measure equilibrium fluctuations as the molecules in the liquid experience them. The vibrational transitions of the OH stretch play the role of the electronic chromophore, but the environment being interrogated is more specific.

The OH stretch frequency is sensitive to the hydrogen bonding environment in the liquid. Rundle's [14] and Badger's [1] earlier work motivated Novak [15], who summarized the relationship between the interatomic oxygen length and the hydride stretch frequency in hydrogen bonding crystals by comparing IR absorption frequencies to

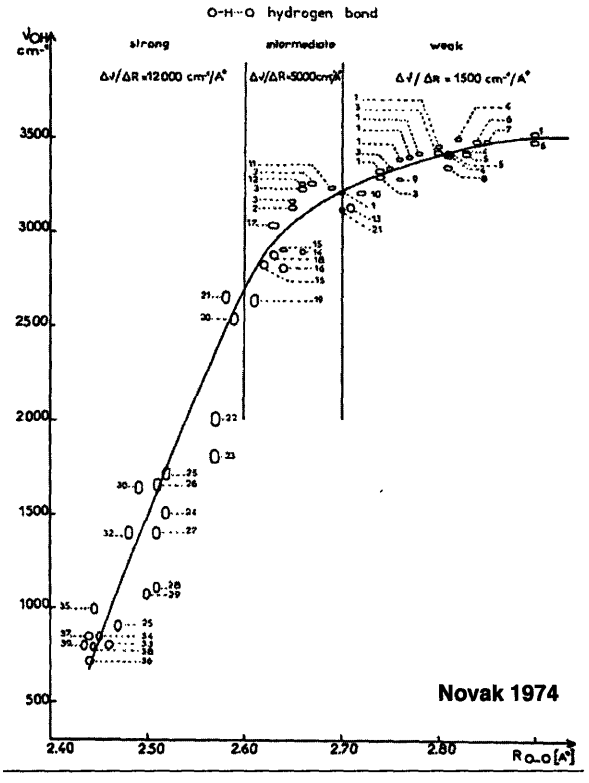

Figure 1-1: ω_{OH} vs. R_{OO} for hydrogen bonding crystals from Novak [15]. Water is in the region of "weak" to "intermediate" hydrogen bonds, with a R_{OO} distance of $\approx$ 2.8 Å. This graph inspired many time-resolved IR experiments that tried to measure the equilibrium fluctuations of directly R_{OO} by probing the relaxations of ω_{OH} [4, 8, 9, 20].

interatomic O$\cdots$O distances between hydrogen bonded pairs (R_{OO}) measured with x-ray crystallography (Figure 1-1). Novak's plot inspired a number of nonlinear ultrafast IR pump-probe spectroscopic studies of HOD in liquid D_2O. Those experiments [4, 8, 9, 20] endeavored to observe the fluctuations of R_{OO} directly by measuring the spectral relaxation of the OH stretch. These experiments, and similar experiments by our group, provide important new quantitative information about dynamics in liquid water on the time scales of intermolecular motions.

MD simulations are my primary tools for relating spectral dynamics to their mi-

croscopic origin. Chapter 2 describes third order nonlinear spectroscopies in detail and explains the protocol I developed to compute OH frequency fluctuations and nonlinear spectroscopic signals from MD simulations. In this chapter I also compare the predictions of MD simulations to the experimentally determined absorption line shape and equilibrium time correlation function (TCF) for the OH stretch frequency (ω_{OH}).

The coupling between the vibrations of the molecule and the remainder of the liquid should be strong enough to observe fluctuations in the liquid, but not so strong that making a vibrational excitation drives the system far from equilibrium. Onsager's regression hypothesis states that in the "linear response" regime[5, 18, 22], small perturbations prepared by an external source are indistinguishable from natural fluctuations at equilibrium. Chapter 3 examines linear response of the HOD molecule explicitly by comparing the rate that a nonequilibrium vibrational excitation returns to equilibrium to the TCF of equilibrium frequency fluctuations.

Novak's relationship (Figure 1-1) shapes how we think about spectroscopy in the liquid state of water, but building empirical relationships between molecular structure from vibrational spectra is an old idea [2]. In Chapter 4, I relate ω_{OH} to a set of physically motivated order parameters, and assign a microscopic origin to the fluctuations of ω_{OH} that experiments measure.

Conventional water potentials for MD simulations approximate charges on the molecules as fixed, but in real systems with explicit electronic degrees of freedom, they are mobile. We have worked with collaborators at Columbia University to develop methods for computing IR spectroscopies in contemporary polarizable models. In

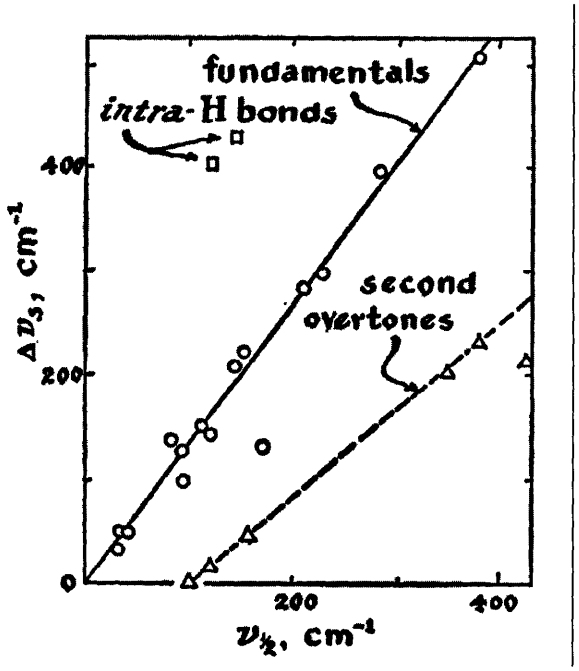

Figure 1-2: IR absorption frequency shift from the gas phase vs. full width at half maximum for hydrogen bonding compounds from Pimentel [16]. Stronger hydrogen bonding red shifts frequencies and also broadens the width of the absorption. 2D IR experiments acquire absorption frequency and width simultaneously.

Chapter 5 we compare results for IR spectroscopy to predictions from fixed charge and fluctuating charge water models. Data from IR spectroscopy is directly useful for examining the role of molecular polarizability on molecular length scales in liquid water and also provides important data to improve upon the microscopic details of empirical water models.

In the liquid, 90 % of the water molecules are engaged in three out of four possible hydrogen bonds. At any instant in time, the remaining available hydrogen bonds are thus "broken." In hydrogen bonding compounds, the width of the absorption line and

red shift increases with the hydrogen bonding strength (Figure 1-2) [16]. Two dimensional IR spectroscopy measures the line shape of the excitation as a function of the preparation frequency. Chapter 6 uses the concepts developed for reaction dynamics in complex systems to relate the dynamics of the absorption frequency measured in ultrafast IR experiments to the hydrogen bond. We consider two scenarios for hydrogen bond rearrangements in water. In one scenario, broken hydrogen bonds are stable chemical species that form an equilibrium with intact hydrogen bonds. Hydrogen bonds change partners by entering into the broken state before finding a new partner [13, 12, 11, 21]. In the second scenario, broken hydrogen bonds are an intrinsically unstable molecular species that appear either as fluctuations of a hydrogen bonded pair or as a transition state that molecules visit when changing hydrogen bond partners.

Bibliography

[1] Richard M. Badger. The relation between the energy of a hydrogen bond and the frequencies of the O – H bands. *Journal of Chemical Physics*, 8:288–9, 1940.

[2] R.M Badger. A relation between internuclear distances and bond force constants. *Journal of Chemical Physics*, 3:710, 1934.

[3] Philip Ball. *Life's Matrix: A Biography of Water.* University of California Press, Berkeley and Los Angeles, 2001.

[4] S. Bratos, G. M. Gale, G. Gallot, F. Hache, N. Lascoux, and J. Cl. Leicknam.

Motion of hydrogen bonds in diluted HDO/D_2O solutions: Direct probing with 150 fs resolution. *Phys. Rev. E*, 61(5):5211–5217, 2000.

[5] David Chandler. *Introduction to modern statistical mechanics.* Oxford University Press (New York), 1987.

[6] D. Eisenberg and W. Kauzman. *The structure and properties of water.* Oxford University Press, 1969.

[7] G.R. Fleming and M. Cho. Chromophore-solvent dynamics. *Annu. Rev. Phys. Chem.*, 47:109–34, 1996.

[8] G. M. Gale, G. Gallot, F. Hache, N. Lascoux, S. Bratos, and J-Cl. Leicknam. Femtosecond dynamics of hydrogen bonds in liquid water: A real time study. *Phys. Rev. Lett.*, page 1068, 1999.

[9] Michel F. Kropman, Han-KWang Nienhuys, Sander Woutersen, and Huib J. Bakker. Vibrational relaxation and hydrogen-bond dynamics of $HDO:H_2O$. *J. Phys. Chem. A*, 105:4622–4626, 2001.

[10] M. J. Lang, X. J. Jordanides, X. Song, and G. R. Fleming. Aqueous solvation studied by photon echo spectroscopy. *J. Chem. Phys.*, 110:5884–5892, 1999.

[11] Alenka Luzar. Resoluving the hydrogen bond conundrum. *J. Chem. Phys.*, 113(23):10663–10675, 2000. And references therein.

[12] Alenka Luzar and David Chandler. Effect of environment on hydrogen bond dynamics in liquid water. *Physical Review Letters*, 76:928–31, 1996.

[13] Alenka Luzar and David Chandler. Hydrogen-bond kinetics in liquid water. *Nature (London)*, 379:55–7, 1996.

[14] Kazuo Nakamoto, Marvin Margoshes, and R.E. Rundle. Stretching frequencies as a function of distances in hydrogen bonds. *Journal of the Americal Chemical Society*, 77:4670–4677, 1955.

[15] A. Novak. Hydrogen bonding in solids. correlation of spectroscopic and crystallographic data. In J. D Dunitz, P. Hemmerich, R. H. Holm, J. A. Ibers, C. K. Jorgenson, J. B. Neilands, D. Reinen, and R. J. P. Williams, editors, *Structure and Bonding*, volume 18, pages 177–216. Springer-Verlag, New York, 1974.

[16] G. C. Pimentel and A.L. McClellan. *The Hydrogen Bond.* Freeman Press, San Fransisco, 1960.

[17] Aneesur Rahman and Frank H. Stillinger. Molecular dynamics study of liquid water. *J. Chem. Phys.*, 55:3336–3359, 1971.

[18] Linda E. Reichl. *A Modern Course in Statistical Physics.* John Wiley and Sons-Interscience, 2nd edition, 1992.

[19] Frank H. Stillinger. Water revisited. *Science*, 209(4455):451–457, 1980.

[20] S. Woutersen and H. J. Bakker. Hydrogen bond in liquid water as a brownian oscillator. *Phys. Rev. Lett.*, 83:2077–2081, 1999.

[21] Huafeng Xu, Harry A. Stern, and B.J. Berne. Can water polarizability be ignored in hydrogen bond kinetics? *J. Phys. Chem. B*, 106:2054–2060, 2002.

[22] Robert Zwanzig. *Nonequilibrium statistical mechanics.* Oxford University Press (New York), 2001.

Chapter 2

Methods

Nonlinear IR spectroscopy is a powerful tool, useful for measuring how fluctuations in molecular environments change the IR absorption frequency of a probe molecule in a liquid host. The experimental data are often so complicated that only detailed modeling can extract microscopic information. Classical MD simulations are explicit computer models of the microscopic environment of a liquid and are one route to microscopic insight when it is not directly available from experimental data. Classical MD simulations use an empirical molecular potential energy function and Newton's equation of motion to describe the evolution of a set of simulated atomic positions and have to be adapted to include the quantum mechanical vibrations of the probe molecule. All of the characteristic frequencies of the translations and rotations of molecules in water are near or below thermal energies (except for the librations) and are slow on the time scale of nuclear vibrational motion, but the vibrations are an order of magnitude faster. In the language of quantum mechanics, there is an adiabatic separation of time scales between the fast vibrational motions and

the slower (classical) molecular translations and rotations that makes calculating vibrational spectroscopy from classical MD simulations feasible.

In this chapter I summarize the formalism of third-order nonlinear spectroscopy and describe the methods we have developed to compute IR absorption frequencies from configurations in an MD simulation and compare the calculations to experiments. Section 2.1 is an outline of nonlinear IR experiments and introduces the third order nonlinear response function, $\boldsymbol{R}^{(3)}(\tau_1, T, \tau_3)$. Section 2.2 reviews how to use time-dependent perturbation theory on a microscopic Hamiltonian to obtain $\boldsymbol{R}^{(3)}(\tau_1, T, \tau_3)$. Section 2.3 describes how we have used the adiabatic separation between the quantal vibration and classical degrees of freedom to obtain nonlinear response functions from MD simulations. The subsection 2.3.2 introduces double-sided Feynman diagrams, which are a popular method of representing mathematical terms in the expansion of the response function pictorially, and shows how to compute them from MD simulation. Section 2.4 is a detailed explanation of the algorithms I have used to write the MD program and gives the specific parameters used in the simulations. Section 2.5 applies the adiabatic protocol developed in Section 2.2 to compute vibrational spectra for HOD in D_2O and compares results to recent linear and nonlinear IR experiments.

2.1 The nonlinear IR experiment

Nonlinear IR spectroscopy is a four wave mixing experiment where three input fields generate a fourth signal field that emerges in a prescribed phase-matched direction. Figure 2-1 is a diagram of the experiment in the traditional "boxcar" phase-matching

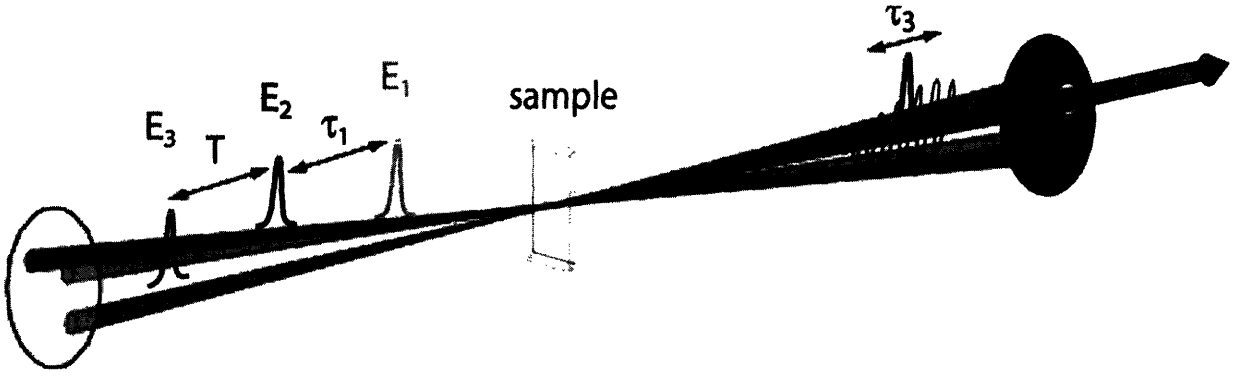

Figure 2-1: Diagram of pulse timings and phase-matching in a nonlinear IR experiment. In the boxcar geometry, the electric fields, delayed by timings τ_1 and T, create a polarization in the sample that radiates a signal (pink) field that emerges in the empty corner of the boxcar. T is called the "waiting time." The solid black line is a heterodyning field that overlaps with the signal field during the time delay τ_3 and measures the signal field interferometrically on a detector placed in the output plane.

direction. Three laser fields interrogate the sample during sequential delay times τ_1, and T, after which the liquid sample emits a signal during the detection time τ_3. The detector measures the signal emerging with wavevector $\boldsymbol{k}_p$, after having probed the system with wavevectors $\boldsymbol{k}_1, \boldsymbol{k}_2$ and $\boldsymbol{k}_3$. For well-separated pulses in the boxcar geometry (see Figure 2-1), there are two important phase matched wavevectors

$$\boldsymbol{k}_{\mathrm{R}} = -\boldsymbol{k}_1 + \boldsymbol{k}_2 + \boldsymbol{k}_3, \tag{2.1}$$

$$\boldsymbol{k}_{\mathrm{NR}} = \boldsymbol{k}_1 - \boldsymbol{k}_2 + \boldsymbol{k}_3,$$

where $\boldsymbol{k}_{\mathrm{R}}$ is called the "rephasing" or echo wavevector, and $\boldsymbol{k}_{\mathrm{NR}}$ the "non-rephasing" wavevector. In practice, one generates these two signals by exchanging the arrival times of pulses E_1 and E_2 in the experiment.

The laser pulses create a nonlinear polarization, $\mathcal{P}^{(NL)}(\boldsymbol{r}, t)$, in the sample that radiates a signal field, $\mathcal{E}_s(\boldsymbol{r}, t)$. Because the envelope is longer in duration than the inverse of the carrier frequency, we make the slowly-varying envelope approximation,

$$\mathcal{E}_s(\boldsymbol{r}, t) = e^{i(\boldsymbol{k}_s \cdot \boldsymbol{r} - \omega_s t)} \boldsymbol{E}_s(\boldsymbol{r}, t) + c.c., \tag{2.2}$$

$$\mathcal{P}^{(NL)}(\boldsymbol{r}, t) = e^{i(\boldsymbol{k}_p \cdot \boldsymbol{r} - \omega_p t)} \boldsymbol{P}^{(NL)}(\boldsymbol{r}, t) + c.c. \tag{2.3}$$

where Eq. 2.3 defines the amplitudes and envelope functions in relation to the real fields and polarizations. In appropriate units, the signal field is the time derivative of the polarization [6]

$$\boldsymbol{E}_s(\boldsymbol{r}, t) = -\frac{\partial \boldsymbol{P}^{(NL)}(\boldsymbol{r}, t)}{\partial t}. \tag{2.4}$$

In the frequency domain, Eq. 2.4 is

$$\boldsymbol{E}_s(\boldsymbol{r},\omega) = i\omega \boldsymbol{P}^{(NL)}(\boldsymbol{r},\omega). \tag{2.5}$$

Because $i = e^{\frac{\pi}{4}}$, the signal field radiates in quadrature to the polarization.

The third order polarization can be written in terms of the third order nonlinear response function $\boldsymbol{R}^{(3)}(\tau_1, T, \tau_3)$ as

$$\mathcal{P}^{(3)}(t) = \int_0^\infty d\tau_3 \int_0^\infty dT \int_0^\infty d\tau_1 \, \boldsymbol{R}^{(3)}(\tau_1, T, \tau_3) : \tag{2.6}$$
$$\mathcal{E}(\boldsymbol{r}, t-\tau_3)\mathcal{E}(\boldsymbol{r}, t-\tau_3-T)\mathcal{E}(\boldsymbol{r}, t-\tau_3-T-\tau_1).$$

2.2 The formalism of nonlinear spectroscopy

$\boldsymbol{R}^{(3)}(\tau_1, T, \tau_3)$ describes the material response to the three input fields. $\boldsymbol{R}^{(3)}(\tau_1, T, \tau_3)$ is a time-dependent quantity, and can be calculated with an explicit microscopic Hamiltonian. We will want to adopt a strategy where the vibrations are quantum mechanical degrees of freedom but the remaining coordinates are classical. Each observable in classical mechanics has a corresponding operator in quantum mechanics. Let us develop a system of compact notation and a way to calculate the time evolution of an observable and operator. An operator in quantum mechanics follows the Heisenberg equation of motion, [18]

$$\frac{dO}{dt} = i[H, O(t)], \tag{2.7}$$

O is a generic operator, H is the Hamiltonian, $[\cdots]$ is the commutator, and $\hbar \equiv 1$.

In Hamiltonian classical mechanics, an observable is a function of all the positions $\boldsymbol{r}^N$ and momenta $\boldsymbol{p}^N$ of the N particles in the system. The positions and momenta are parametric functions of time, t. The time derivative of the observable, $o(\boldsymbol{r}^N, \boldsymbol{p}^N; t)$ follows from the chain rule of partial differentiation,

$$\frac{d\, o(\boldsymbol{r}^N, \boldsymbol{p}^N; t)}{dt} = \sum_i \frac{\partial \boldsymbol{r}_i}{\partial t} \frac{\partial o(\boldsymbol{r}^N, \boldsymbol{p}^N; t)}{\partial \boldsymbol{r}_i} + \frac{\partial \boldsymbol{p}_i}{\partial t} \frac{\partial o(\boldsymbol{r}^N, \boldsymbol{p}^N; t)}{\partial \boldsymbol{p}_i}. \tag{2.8}$$

By using Hamilton's equations

$$\begin{aligned} \frac{d\, \boldsymbol{r}_i}{dt} &= \frac{\partial H}{\partial \boldsymbol{p}_i}, \\ \frac{d\, \boldsymbol{p}_i}{dt} &= -\frac{\partial H}{\partial \boldsymbol{r}_i}, \end{aligned} \tag{2.9}$$

Equation 2.8 can be written with Poisson Brackets.[1]

$$\frac{d\, o(\boldsymbol{r}^N, \boldsymbol{p}^N)}{dt} = \{H, o(\boldsymbol{r}^N, \boldsymbol{p}^N)\}. \tag{2.11}$$

With this cosmetic change, observables and operators evolve under the Liouvillian,

[1]Poisson Brackets between $A(\boldsymbol{r}^N, \boldsymbol{p}^N)$ and $B(\boldsymbol{r}^N, \boldsymbol{p}^N)$ are defined by

$$\{A(\boldsymbol{r}^N, \boldsymbol{p}^N), B(\boldsymbol{r}^N, \boldsymbol{p}^N)\} = \sum_i \frac{\partial A}{\partial \boldsymbol{p}_i} \frac{\partial B}{\partial \boldsymbol{r}_i} - \frac{\partial A}{\partial \boldsymbol{r}_i} \frac{\partial B}{\partial \boldsymbol{p}_i}. \tag{2.10}$$

$\mathcal{L}$.

$$\frac{dO}{dt} = i\mathcal{L}O, \tag{2.12}$$

$$\frac{do}{dt} = i\mathcal{L}o,$$

$$i\mathcal{L}O = i[H, O],$$

$$i\mathcal{L}o = \{H, o\}.$$

Equations 2.12 can be solved as an initial value problem

$$O(t) = e^{i\mathcal{L}t}O(0), \tag{2.13}$$

$$o(\boldsymbol{r}^N, \boldsymbol{p}^N; t) = e^{i\mathcal{L}t}o(\boldsymbol{r}^N, \boldsymbol{p}^N; 0), \tag{2.14}$$

which defines the quantity $G(t_0, t) = e^{i\mathcal{L}(t-t_0)}$ as the propagator or Green operator that propagates quantities from time t_0 to time t. When $t_0 = 0$, we use the shorthand

$$G(t_0 = 0, t) \equiv G(t). \tag{2.15}$$

The isomorphism represented by Equations 2.12 is useful to describe dynamics of quantities that are functions of both classical phase space coordinates *and* quantum mechanical coordinates.

The Hamiltonian describes the input electric fields and the radiation-matter in-

teraction. The full Hamiltonian is

$$\mathcal{H} = H_{\text{matter}} + H_{\text{field}} + \lambda H_{\text{matter-field}}(t), \tag{2.16}$$

where H_{matter} is the microscopic Hamiltonian, H_{field} is the Hamiltonian for the interacting fields alone, and $H_{\text{matter-field}}(t)$ describes the interaction of the electric fields with the matter. $H_{\text{field}}(t)$ is the bare field Hamiltonian, whose dynamics are irrelevant. We work in the limit where spontaneous emission is unimportant, and where the characteristic interaction lengths are much smaller than the wavelength of the light fields. In this limit we can treat the electric fields as classical variables, and use the dipole or *E1* approximation [18] to write

$$\lambda H_{\text{matter-field}} = -\lambda \boldsymbol{m}(\{Q_{\text{micro}}\}, t) \cdot \mathcal{E}(\boldsymbol{r}, t), \tag{2.17}$$

where $\boldsymbol{m}(\{Q_{\text{micro}}\}, t)$ is the total dipole moment operator (a macroscopic quantity), $\{Q_{\text{micro}}\}$ are the microscopic degrees of freedom, and $\boldsymbol{r}$ is the position vector of the electric field, $\mathcal{E}$ at time t. λ is an ordering parameter whose numerical value is unity, but keeps track of the order of terms in a perturbation series.

There are a few simplifications we can make to the total dipole moment operator, $\boldsymbol{m}$. First, the total dipole moment operator is the sum of all dipoles in the system,

$$\boldsymbol{m} = \sum_i \boldsymbol{m}^{(i)}, \tag{2.18}$$

because at low enough concentrations there is no interaction between the dipoles

of absorbing molecules. Secondly, we are interested in vibrational transitions so we expand the dipole moment operator into

$$\boldsymbol{m} = \boldsymbol{m}^{(0)} + \sum_i \sum_j \frac{\partial \boldsymbol{m}_j^{(i)}}{\partial Q_j} Q_j, \tag{2.19}$$

where Q_j is the coordinate for the j^{th} vibration, and $\boldsymbol{m}^{(0)}$ is the permanent dipole moment. We define $\boldsymbol{\mu}$ by

$$\boldsymbol{\mu} \equiv \sum_i \sum_j \frac{\partial \boldsymbol{m}_j^{(i)}}{\partial Q_j} Q_j \tag{2.20}$$

$\frac{\partial \boldsymbol{m}_j}{\partial Q_j}$ is called the transition dipole moment for the j^{th} vibration. The laser fields induce transitions between states so the diagonal matrix elements of $\boldsymbol{\mu}$ are irrelevant.

We will need to treat the explicit time-dependence of the Hamiltonian separately. For brevity of notation, we separate the time-independent part

$$H_0 = H_{\text{matter}}, \tag{2.21}$$

from the time-dependent matter-field interaction

$$\lambda V(t) = -\lambda \boldsymbol{\mu}(\{Q_{\text{micro}}\}, t) \cdot \boldsymbol{E}(\boldsymbol{r}, t). \tag{2.22}$$

The total Hamiltonian in Equation 2.16 becomes

$$\mathcal{H} = H_0 + \lambda V(t). \tag{2.23}$$

The time-dependent Schrödinger equation is

$$i\frac{\partial|\Psi(t)\rangle}{\partial t} = \mathcal{H}|\Psi(t)\rangle, \tag{2.24}$$

In the Schrödinger representation, the time-dependence of an observable is

$$\langle O(t)\rangle = \langle\Psi(t)|O|\Psi(t)\rangle. \tag{2.25}$$

by expanding $|\Psi(t)\rangle$ in a complete basis ($|\Psi(t)\rangle = \sum_n c_n(t)|n\rangle$), and accounting for the weight of each state in the canonical ensemble, one can rewrite 2.25 as

$$\langle O(t)\rangle = Trace(\rho(t)O), \tag{2.26}$$

where

$$\rho(t) = \frac{e^{-\beta H_0}|\Psi(t)\rangle\langle\Psi(t)|}{Trace(e^{-\beta H_0})}, (\beta = \frac{1}{k_B \mathrm{T}}). \tag{2.27}$$

defines the density matrix. The off-diagonal elements of the density matrix describe coherences between quantum states, and the diagonal matrix elements represent the populations. The density matrix, in turn, obeys the Liouville equation

$$\frac{d\,\rho(t)}{dt} = -i\mathcal{L}(t)\rho(t). \tag{2.28}$$

Because the field-matter interaction is time-dependent, the Liouvillian in Equation 2.28 is an explicit function of time. We switch from the Schrödinger picture to Dirac's

interaction picture by making the substitution,

$$\rho(t) = e^{-i\mathcal{L}_0 t}\rho_I(t) \tag{2.29}$$

where $\mathcal{L}_0$ is the Liouvillian for the time-independent part, H_0. Substituting Equation 2.29 for Equation 2.28 yields the equation of motion for the density matrix in the interaction picture [18]

$$\frac{d\,\rho_I(t)}{dt} = -i\lambda\mathcal{L}_V(t)\rho_I(t). \tag{2.30}$$

$\rho_I(t)$ evolves only under the time-dependent perturbation. $\mathcal{L}_V(t)$ is the Liouvilian of the time-dependent perturbing Hamiltonian.

One develops the perturbation (Dyson) series for $\rho(t)$ by integrating 2.30

$$\rho(t) = e^{-i\mathcal{L}_0 t}\rho(-\infty) + \lambda\int_{-\infty}^{t} dt' e^{-i\mathcal{L}_0(t-t')}(-i\mathcal{L}_V(t'))\rho(t'). \tag{2.31}$$

and iterating to the desired order in λ.

The third order polarization is $\mathcal{P}^{(3)}(\boldsymbol{r},t) = Trace(\boldsymbol{\mu}\rho^{(3)}(t))$, and

$$\rho^{(3)}(t) = (-i)^3\lambda^3\int_{-\infty}^{t} dt_3\int_{-\infty}^{t_1} dt_2\int_{-\infty}^{t_2} dt_1\,[V(t_3),[V(t_2),[V(t_1),\rho^{(0)}(-\infty)]]], \tag{2.32}$$

where $\rho^{(0)}(-\infty)$ is the unperturbed density matrix in the infinite past, the $\{t_k\}$ are dummy variables used in the integration, and $V(t) = e^{i\mathcal{L}_0 t}V(0)$. Taking the electric fields outside the nested commutators and inserting 2.32 for the polarization, and changing the limits of integration of the time vatiables (See Fig. 2-1) defines the

third order response function.

$$\boldsymbol{R}^{(3)}(t_1,t_2,t_3) = (i)^3\theta(t_1)\theta(t_2)\theta(t_3)Trace(\boldsymbol{\mu}(0)[\boldsymbol{\mu}(t_3),[\boldsymbol{\mu}(t_2),[\boldsymbol{\mu}(t_1),[\rho^{(0)}(-\infty)]]]]), \tag{2.33}$$

where the step functions $\theta(t)$ enforce causality. The polarization is

$$\mathcal{P}^{(3)}(t) = \int_0^\infty d\tau_3 \int_0^\infty d\tau_2 \int_0^\infty d\tau_1 \; \boldsymbol{R}^{(3)}(\tau_1,T,\tau_3) : \tag{2.34}$$
$$\mathcal{E}(\boldsymbol{r},t-\tau_3)\mathcal{E}(\boldsymbol{r},t-\tau_3-T)\mathcal{E}(\boldsymbol{r},t-\tau_3-T-\tau_1).$$

The : operator denotes a tensor contraction. $\boldsymbol{R}^{(3)}(\tau_1,T,\tau_3)$ contains all of the microscopic information accessible in nonlinear IR experiments. Each commutator in Equation 2.33 acts to the left and right and so generates a pair of terms. There are $2^3 = 8$ possible pairings, half of which are complex conjugates, leaving only four independent expressions. Quantum mechanical correlation functions obey detailed balance, so that in the time domain

$$\langle O(t)O(0)\rangle = \langle O(0)O(t)\rangle^*. \tag{2.35}$$

Using Equation 2.35 cancels the factor of i and turns $\boldsymbol{R}^{(3)}(\tau_1,T,\tau_3)$ into a real valued quantity.

The interaction picture has removed the interactions with the laser fields from the calculation of $\boldsymbol{R}^{(3)}(\tau_1,T,\tau_3)$, because $\boldsymbol{\mu}$ is not a function of the radiation variables.

2.3 Response functions from MD simulations

We will discuss the details of how MD simulations provide a sets of atomic configurations in Section 2.4, but this is not the difficult part of the problem. We first need to motivate the spectroscopy from a microscopic Hamiltonian so that we know how to adapt the the classical MD simulations. In this section, we take it as given that we can generate a classical set of atomic positions with a computer simulation and develop a formalism for computing vibrational frequencies from atomistic configurations of the liquid.

We use the adiabatic separation of time scales between the fast vibrations and the slower translations and rotations of the molecules. In Section 2.5 we specialize the discussion to the OH stretch of HOD in liquid D_2O, but the adiabatic strategy is generally applicable. It begins by partitioning a generic microscopic Hamiltonian for the vibrations of a molecule in a liquid host. A general form for H_{matter} is

$$H_{\text{matter}} = H_{\text{s}}(\{P\},\{Q\}) + H_{\text{sb}}(\{P\},\{Q\},\boldsymbol{r}^N,\boldsymbol{p}^N) + H_{\text{b}}(\boldsymbol{r}^N,\boldsymbol{p}^N). \tag{2.36}$$

In Equation 2.36, H_{s} is the quantal system Hamiltonian, H_{b} is the classical "bath" Hamiltonian, and H_{sb} is the coupling between system and bath. $\{P\}$ and $\{Q\}$ are the momentum and position operators of the system Hamiltonian in internal coordinates. We represent the system Hamiltonian with a complete set of eigenstates that we know,

$$H_{\text{s}}|a\rangle = E_a|a\rangle. \tag{2.37}$$

To generate more useful expressions for $\boldsymbol{R}^{(3)}(\tau_1, T, \tau_3)$, we insert a complete set of system states ($\{|a\rangle\}$) on each side of the operators in Equation 2.33. For example, the term where each of the dipole operators acts on the left of the density matrix

$$\boldsymbol{R}_I^{(3)}(\tau_1, T, \tau_3) = -iTrace(\boldsymbol{\mu}(0)\boldsymbol{\mu}(\tau_3)\boldsymbol{\mu}(T)\boldsymbol{\mu}(\tau_1)\rho(-\infty)), \tag{2.38}$$

becomes

$$\boldsymbol{R}_I^{(3)}(\tau_1, T, \tau_3) = -i \sum_{a,b,c,d} Trace(\boldsymbol{\mu}_{ab}(0)\boldsymbol{\mu}_{bc}(\tau_3)\boldsymbol{\mu}_{cd}(T)\boldsymbol{\mu}_{da}(\tau_1)\rho_{aa}^{(0)}(-\infty)). \tag{2.39}$$

In 2.39, $\boldsymbol{\mu}_{ab}(t) = \langle a|\boldsymbol{\mu}(t)|b\rangle$, and we have assumed that the unperturbed system is in pure state $|a\rangle\langle a|$ at equilibrium in the infinite past.

2.3.1 The adiabatic solution

The bath coordinates in the Hamiltonian (Equation 2.36) are classical and are much slower than the quantal coordinates and momenta. We make the adiabatic approximation to the Hamiltonian, and for each frozen or "clamped" configuration of the atomic positions in the MD simulation the adiabatic Schrödinger Equation is

$$(H_s(\{P\}, \{Q\}) + H_{sb}(\{P\}, \{Q\}, \boldsymbol{r}^N; t))|\Psi(\boldsymbol{r}^N; t)\rangle = \mathcal{E}(\boldsymbol{r}^N; t)|\Psi(\boldsymbol{r}^N; t)\rangle. \tag{2.40}$$

H_{sb} is a function of time, so we return again to the familiar interaction picture to

obtain an expression for the Green operator on $\boldsymbol{\mu}$,

$$G(t)\boldsymbol{\mu} = G_I(t)G_0(t)\boldsymbol{\mu} \tag{2.41}$$

The Liouvillian splits into

$$i\mathcal{L}_{\text{classical}} = \{H_{\text{matter}}, \cdots\} \tag{2.42}$$

$$i\mathcal{L}_{\text{quantum}} = i[H_{\text{matter}}, \cdots] \tag{2.43}$$

The dipole operator is a function of both the rotational state of the molecule, which is classical, and the vibrational state of the molecule, which is quantal.

$$\boldsymbol{\mu} = \mu(\{Q\})\boldsymbol{e}(\boldsymbol{r}^N), \tag{2.44}$$

In Equation 2.44, $\boldsymbol{e}(\boldsymbol{r}^N)$ is the unit vector of the transition dipole and is attached to the molecule. In the adiabatic scheme, there is no ro-vibrational coupling (the bath positions are clamped) so the vibrational and rotational averages are separate. The classical Liouvillian $\{H_{\text{b}}, \cdots\}$ propagates $\boldsymbol{e}$, so that $\boldsymbol{R}_I^{(3)}(\tau_1, T, \tau_3)$ becomes

$$\begin{aligned}\boldsymbol{R}_I^{(3)}(\tau_1, T, \tau_3) = -i \sum_{a,b,c,d} \langle \boldsymbol{e}(0)\boldsymbol{e}(\tau_1)\boldsymbol{e}(T)\boldsymbol{e}(\tau_3)\rangle \times \\ Trace(\mu_{ab}(0)\mu_{bc}(\tau_3)\mu_{cd}(T)\mu_{da}(\tau_1)\rho_{aa}^{(0)}(-\infty)).\end{aligned} \tag{2.45}$$

The first term in brackets is the orientational response function. It is the tensor part of the response and describes how the sample responds to the input polarization

fields. After the tensor contraction with the polarization vectors of the input fields in Equation 2.35, the orientational response function is

$$Y_{ijkl}(\tau_1, T, \tau_3) = \langle (\boldsymbol{e}(0) \cdot \boldsymbol{l})(\boldsymbol{e}(\tau_1) \cdot \boldsymbol{i})(\boldsymbol{e}(T) \cdot \boldsymbol{j})(\boldsymbol{e}(\tau_3) \cdot \boldsymbol{k}) \rangle, \tag{2.46}$$

where $\boldsymbol{i}, \boldsymbol{j}, \boldsymbol{k}$, and $\boldsymbol{l}$ are the polarization directions of the input fields in the laboratory frame interacting in chronological order.[2] The second term in brackets is the vibrational response function for $\boldsymbol{R}_I^{(3)}(\tau_1, T, \tau_3)$, which we denote simply as $R^{(3)}(\tau_1, T, \tau_3)_I$.

Inserting a complete set of system states on either side of $\mu(t)$ returns

$$\sum_{a,b} |a\rangle\langle a|\mu(t)|b\rangle\langle b| = \sum_{a,b} |a\rangle\langle a|e^{i\mathcal{L}_b t} G_I(t)(G_0(t)\mu)|b\rangle\langle b|, \tag{2.50}$$

We use the interaction picture to evaluate the quantum propagator,

$$e^{i\mathcal{L}_{\text{quantum}} t}\boldsymbol{\mu} = U_{\text{sb}}(t)^\dagger U_{\text{s}}(t)^\dagger \boldsymbol{\mu} U_{\text{s}}(t) U_{\text{sb}}(t). \tag{2.51}$$

The time-evolution operators are the results of solving the adiabatic Schrödinger

[2]Detailed analysis[8], shows that for a spherical rotor, a good series of approximations leads to the results

$$Y_{zzzz}(\tau_1, T, \tau_3) = \frac{1}{9} c_1(\tau_1) c_1(\tau_3)(1 + \frac{4}{5} c_2(T)), \tag{2.47}$$

$$Y_{yyzz}(\tau_1, T, \tau_3) = \frac{1}{9} c_1(\tau_1) c_1(\tau_3)(1 + \frac{2}{5} c_2(T)). \tag{2.48}$$

and that these are the only two independent orientational response functions for an isotropic system. The $c_n(t)$ are the time-dependent coefficients

$$c_n(t) = \langle P_n(\boldsymbol{e}(t) \cdot \boldsymbol{e}(0)) \rangle, \tag{2.49}$$

and P_n is a Legendre polynomial of degree n.

equation in the interaction picture,

$$U_{\rm s}(t) = e^{-iH_s t}, \tag{2.52}$$

$$U_{\rm sb}(t) = e^{-i\int_0^t dt' H_{\rm sb}(t')}. \tag{2.53}$$

It is difficult to work with $e^{-i\int_0^t dt' U_{\rm sb}(t')}$, because it is not necessarily diagonal in the system eigenstates. To extract the diagonal part, introduce the projection operator P

$$PH_{\rm sb} = \sum_a |a\rangle\langle a|H_{\rm sb}|a\rangle\langle a|. \tag{2.54}$$

We assume that the off-diagonal elements are small and write the matrix elements of $H_{\rm sb}$ as

$$H_{\rm sb}(\boldsymbol{r}^N;t)_{ab} = \delta_{ab}\mathcal{E}_a(\boldsymbol{r}^N;t) + \lambda(1-\delta_{ab})\ H_{\rm sb}(\mathrm{r^N;t})_{\rm ab}. \tag{2.55}$$

The interaction Green operator can be replaced to $O(\lambda)$ with its projected diagonal part.

$$e^{-i\int_0^t dt' PH_{\rm sb}(t')} + O(\lambda). \tag{2.56}$$

Replacing the interaction propagator with its projected part is sometimes called the "pure dephasing" approximation [19, 13], and gives an expression for $\mu(t)$ in the adiabatic approximation.

$$G(t)\mu = \sum_{a,b} |a\rangle e^{i\mathcal{L}_{\rm classical}t}\mu_{ab}e^{-i\int_0^t dt'(\mathcal{E}_a(\boldsymbol{r}^N;t')-\mathcal{E}_b(\boldsymbol{r}^N;t'))}\langle b|. \tag{2.57}$$

Because μ_{ab} are just matrix elements, we can associate the Green Operators with the

density matrix and transform Equation 2.39 into

$$R_I^{(3)}(\tau_1, T, \tau_3) = -i \sum_{a,b,c,d} Trace\left(\mu_{ad}\mu_{dc}\mu_{cb}\mu_{ab}G_{bc}(\tau_3)G_{cd}(T)G_{da}(\tau_1)\rho_{aa}^{(0)}(0)\right). \quad (2.58)$$

2.3.2 Pictorial perturbation theory and expressions for HOD in D_2O

It is often more intuitive to represent a perturbation theory pictorially. In a diagrammatic perturbation theory, pictures represent mathematical terms in the perturbation expansion. Equation 2.57 describes how the laser pulses in the experiment cycle the system through various coherences, and gives Equation 2.58 a nice diagrammatic representation. For example, during the first time period, τ_1, the Green Operator propagates the density matrix from the pure state $|a\rangle\langle a|$ to a coherence $|b\rangle\langle a|$.

Let us denote each of the terms in Equation 2.58 by $\sigma_{\boldsymbol{u}}$ where $\boldsymbol{u}$ is a vector that contains the system indices a,b,c and d. In this compact notion, Equation 2.58 is

$$R_I^{(3)}(\tau_1, T, \tau_3) = -i \sum_{\boldsymbol{u}} \sigma_{\boldsymbol{u}}. \quad (2.59)$$

The $\sigma_{\boldsymbol{u}}$ are all the terms in the system Hamiltonian, but only some of them will be resonant with the input fields. The $\sigma_{\boldsymbol{u}}$ that survive after making the rotating wave approximation can be calculated by drawing the double-sided Feynman diagrams [13].

As an example let us calculate one diagram for the rephasing experiment. The

Diagrammatic symbol	Mathematical term	Physical process
↗	$+\boldsymbol{k}$	Input pulse with wavevector $\boldsymbol{k}$
↗ |	$+\boldsymbol{k}$	Absorption
| ↗	$+\boldsymbol{k}$	Stimulated Emission
↖	$-\boldsymbol{k}$	Input pulse with wavevector $-\boldsymbol{k}$
| ↖	$-\boldsymbol{k}$	Absorption
↖ |	$-\boldsymbol{k}$	Stimulated Emission
$\overset{t}{t_0}\overline{\vert ab\vert}$	$\vert a\rangle\langle b\vert e^{-i\int_{t_0}^{t} dt'\omega_{ab}(t')}\mu_{ab}$	Coherence with frequency $\mathcal{E}_a - \mathcal{E}_b$.
$\underline{\vert bb\vert}$	$\vert b\rangle\langle b\vert$	Vibrational population in b

Table 2.1: Diagrammatic rules for constructing response functions from double-sided Feynman Diagrams. For every interaction on the left side of the density matrix, multiply the diagram by -1. By selecting a phase-matching condition (eg. $-\boldsymbol{k}_1+\boldsymbol{k}_2+\boldsymbol{k}_3$), one draws a diagram for every combination consistent with that phase-matching direction. Vertical bars denote the ket and bra sides of the density matrix and time progresses in the vertical direction. Figure 2-2 is an example of one diagram from the rephasing wavevector geometry.

experimental phase-matching condition is

$$\boldsymbol{k}_{\mathrm{R}} = -\boldsymbol{k}_1 + \boldsymbol{k}_2 + \boldsymbol{k}_3. \tag{2.60}$$

If one represents the density matrix by two solid vertical lines where time progresses in the vertical direction, the picture resulting from Equation 2.58 is Figure 2-2. Table 2.3.2 translates the diagramamatic pictures into mathematical terms for the response functions.

For the rephasing phase matching condition, there are two diagrams for the fundamental transitions, but only one for the overtone transition. The diagram for the overtone transition has an even number of left side interactions, but the fundamentals have an odd number. Hence the diagrams for the overtone and fundamental transitions are out of phase with one another. Summing over all the diagrams consistent

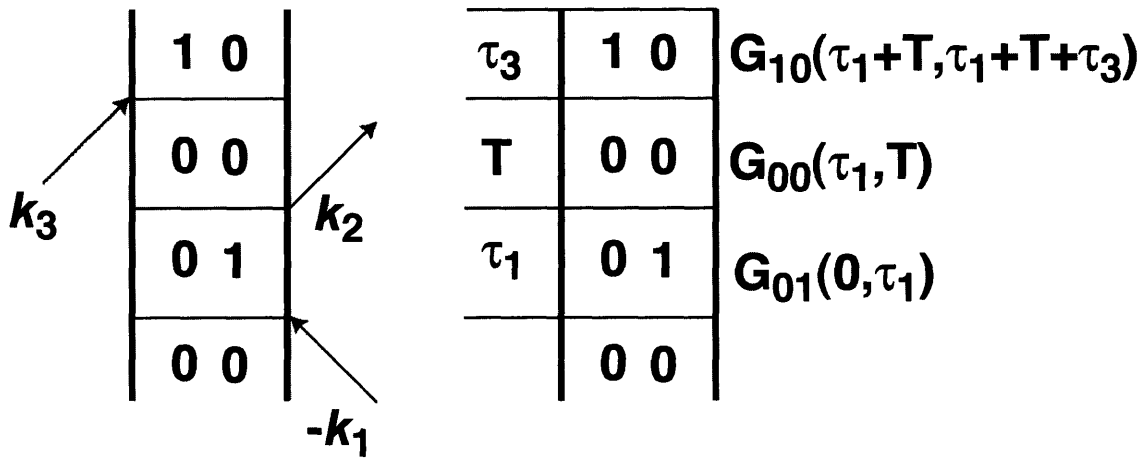

$$\sigma(\tau_1,T,\tau_3) = |\mu_{10}|^4 \langle G_{01}(0,\tau_1)\, G_{00}(\tau_1,T)\, G_{10}(\tau_1+T,\tau_3+T+\tau_3)\rangle$$

Figure 2-2: Feynman diagram for the rephasing phase-matching geometry. The left hand side of the Figure is a Feynman diagram calculated for the echo phase-matching direction, $\boldsymbol{k}_p = -\boldsymbol{k}_1 + \boldsymbol{k}_2 + \boldsymbol{k}_3$. The negative wavevectors face towards the left and the positive ones face towards the right. The numbers in the middle of the diagram label the states of the density matrix. The system begins in the ground state, $\rho^{(aa)}(-\infty) = |0\rangle\langle 0|$. Calculating Feynman diagrams starts by enumerating all the diagrams consistent with the given phase-matching direction. The right hand side is the diagram that labels the time intervals that are the arguments of the Green Operators. This particular diagram is $\sigma_{01,00,10}$.

with the rephasing phase-matching direction ($\boldsymbol{k}_{\mathrm{R}} = -\boldsymbol{k}_1 + \boldsymbol{k}_2 + \boldsymbol{k}_3$) gives

$$R_{\mathrm{R}}(\tau_1, T, \tau_3) = \tag{2.61}$$
$$2|\mu_{10}|^2|\mu_{10}|^2\langle exp\left(i\int_0^{\tau_1} dt\,\omega_{10}(t) - i\int_{\tau_1+T}^{\tau_1+T+\tau_3} dt\,\omega_{10}(t)\right)\rangle$$
$$-|\mu_{21}|^2|\mu_{10}|^2\langle exp\left(i\int_0^{\tau_1} dt\,\omega_{10}(t) - i\int_{\tau_1+T}^{\tau_1+T+\tau_3} dt\,\omega_{21}(t)\right)\rangle - c.c.$$

In Equation 2.61, the brackets are the average over the classical degrees of freedom, and $\omega_{10}(t) = \mathcal{E}_1(\boldsymbol{r}^N; t) - \mathcal{E}_0(\boldsymbol{r}^N; t)$. For the nonrephasing phase-matching direction ($\boldsymbol{k}_{\mathrm{NR}} = \boldsymbol{k}_1 - \boldsymbol{k}_2 + \boldsymbol{k}_3$)

$$R_{\mathrm{NR}}(\tau_1, T, \tau_3) = \tag{2.62}$$
$$2|\mu_{10}|^2|\mu_{10}|^2\langle exp\left(-i\int_0^{\tau_1} dt\,\omega_{10}(t) - i\int_{\tau_1+T}^{\tau_1+T+\tau_3} dt\,\omega_{10}(t)\right)\rangle$$
$$-|\mu_{21}|^2|\mu_{10}|^2\langle exp\left(-i\int_0^{\tau_1} dt\,\omega_{10}(t) - i\int_{\tau_1+T}^{\tau_1+T+\tau_3} dt\,\omega_{21}(t)\right)\rangle - c.c.$$

The sign change on the $\int_0^{\tau_1}\cdots$ term between Eqs. 2.61 and 2.62 arises from the difference in the wavevector $-\boldsymbol{k}_1 \rightarrow \boldsymbol{k}_1$ between phase-matching conditions. This flips the sign of the coherence during the first time period $\omega_{01} \rightarrow \omega_{10}$ and $\omega_{01} = -\omega_{10}$.

In the pure dephasing approximation, we have neglected the processes of vibrational relaxation and energy transfer. Unfortunately, serious fundamental inconsistencies arise when one attempts to compute energy transfer rates between classical and quantum degrees of freedom [3]. While improvised protocols exist for calculating these rates based on Landau and Teller's formula [9], a more satisfactory calculation likely requires elaborate quantum or semi-classical dynamical rules that are beyond

the scope of the current study. Recent experiments find a vibrational relaxtion and energy redistribution time of $\approx$ 700 fs [11, 5]. We expect the consequences of neglecting vibrational energy redistribution to become most severe after this time scale.

2.4 Simulation details

The adiabatic strategy allows us to compute ω_{OH} from an atomic configuration, and MD simulations provide a chronological set of positions, $\boldsymbol{r}^N$. Here are the details. In the constant energy constant volume (NVE) scheme for MD, Newton's equation propagates the positions of all the atoms forward in time. Because numerical simulations of Avagadro's number of particles are computationally infeasible, one focuses instead on a smaller number of molecules (typically between 100 and 10,000). If the system is large enough, the boundary conditions are unimportant. Conventionally, one uses periodic boundary conditions so that $\boldsymbol{r}_i^{\boldsymbol{n}} = \boldsymbol{r}_i + \boldsymbol{n}L$, where L is the box-length determined by the simulated density, $\boldsymbol{r}_i^{\boldsymbol{n}}$ is the position of atom i in the $\boldsymbol{n}^{\mathrm{th}}$ image box and $\boldsymbol{n}$ is a vector of integers. The physical motivation for this particular choice of boundary conditions is that they replicate the central box *ad infinitum*[1].

At the beginning of the simulation, one generates a molecular configuration that is reasonably close to a configurational state in the liquid. The dynamics proceed by assigning each atom a random velocity chosen from an appropriate Boltzmann distribution and then equilibrating until there is no memory of the initial configuration. I have chosen 107 D_2O molecules and one HOD molecule. To generate the initial configuration, I have put the oxygen atoms at the points of a face centered cu-

bic (FCC) lattice and given the molecules random orientations. The thermodynamic state point for D_2O at T= 298K corresponds to a density of 1.104 $\frac{g}{cm^3}$. I have used the Box-Muller algorithm to generate normal random deviates for the velocities of each molecule[15] with a standard deviation consistent with the number of degrees of freedom and the simulated temperature of 298 K.[3] After roughly 10 ps of simulation time, the system loses memory of the initial nonequilbrium configuration (FCC lattice with random orientations) and relaxes to an equilibrium configurational state of the liquid.

The key ingredient in an MD simulation is the potential energy function for all of the atoms in the system. Our mainstay potential is the extended simple point charge model (SPC/E) [2]. We use this potential almost exclusively, except in Chapter 5 when we run MD with other polarizable and fixed charge potential energy functions. In the SPC/E model of water, all of the OH bonds are fixed to 1.0 Å, and the OHO angle is 109.47°. One is always free to choose three independent units of measurement. Natural units for water are kJ/mol for energy, femtoseconds for time, and Å for length. Each atomic site has a partial charge and they interact according to Coulomb's Law,

$$U_{\text{electrostatic}} = \frac{1}{2}\sum_{i}\sum_{j,j\neq i}\frac{z_i z_j}{r_{ij}}, \tag{2.63}$$

where the sum is over all atoms in the central box and their periodic images. In the

[3]For N molecules, the number of degrees of freedom, N_f, is $6N-3$ because each molecule is free to translate and rotate in three dimensions but the total momentum of molecules in the central box is zero, placing three constraints on the degrees of freedom

units I have used,

$$z_{\mathrm{H}} = 15.796\sqrt{\mathrm{kJ/mol\ \AA}}, \tag{2.64}$$

$$m_{\mathrm{D}} = 2.02 \times 10^4 \frac{\mathrm{fs^2 kJ/mol}}{\mathrm{\AA}^2}, \tag{2.65}$$

$$m_{\mathrm{H}} = 1.01 \times 10^4 \frac{\mathrm{fs^2 kJ/mol}}{\mathrm{\AA}^2}, \tag{2.66}$$

$$m_{\mathrm{O}} = 16.00 \times 10^4 \frac{\mathrm{fs^2 kJ/mol}}{\mathrm{\AA}^2}. \tag{2.67}$$

In the above, m is the mass of either hydrogen (H), deuterium (D), or oxygen (O), z the charge, and r_{ij} is the distance between atoms i and j. The oxygen atoms also interact through a Lennard–Jones 6-12 potential,

$$\epsilon = 0.6502\,\mathrm{kJ/mol} \tag{2.68}$$

$$\sigma = 3.16555725812892\,\mathrm{\AA} \tag{2.69}$$

$$V_{\mathrm{LJ}}(r) = 4\epsilon\left(\left(\frac{\sigma}{r}\right)^{12} - \left(\frac{\sigma}{r}\right)^{6}\right), \tag{2.70}$$

$$U_{\mathrm{LJ}} = \frac{1}{2}\sum_{i}\sum_{I,J\neq I} V_{\mathrm{LJ}}(r_{IJ}). \tag{2.71}$$

I and J are the oxygen atoms of two different molecules. Because the Lennard–Jones potential is short range, I did not include molecules in the sum with $r_{ij} > \frac{L}{2}$, where L is the box length, and calculated the Lennard–Jones potential energies and the forces with the appropriate shifted force potentials [1].

Ewald sums

The electrostatic forces in Eq. 2.63 are long-range, but at large separations ($r_{ij} > L$) they are between periodically replicated images. The Ewald method makes use of the boundary conditions to provide a computationally feasible way to handle this sum [1]. In the Ewald sum, the atoms in the central box are screened with a Gaussian screening function. The potential energy for all (screened) atoms in the central box is

$$V_{\text{real}} = \frac{1}{2}\sum_{i}\sum_{j,j\neq i}\frac{erfc(\kappa r_{ij})}{rij}z_i z_j, \tag{2.72}$$

where κ is the screening parameter and $erfc(z)$ is the complementary error function, $erfc(z) = \frac{2}{\sqrt{\pi}}\int_z^\infty dte^{-t^2}$. The screening function has to be subtracted from Equation 2.72. This is done in reciprocal space. The potential energy between the periodically replicated images is

$$V_{\text{k}} = \frac{2\pi}{L^3}\sum_{\boldsymbol{k}\neq 0}\frac{e^{-\frac{k^2}{4\kappa^2}}}{k^2}|S(\boldsymbol{k})|^2, \tag{2.73}$$

where $S(\boldsymbol{k}) = \sum_i z_i e^{i\boldsymbol{k}\cdot r_i}$ is the ionic structure factor. The Fourier transform interacts atoms on the same molecule, and these terms are subtracted out in real space. The screening parameter partitions the sum of the potential energy between real space and $\boldsymbol{k}$-space. I found the screening parameter to be $\frac{5.0}{L}$, and that the sum for the potential energy as a function of the number of wavevectors converged at $\approx$ 200 wavevectors [1].

Constraint dynamics

Each atom in the simulation experiences a force, $\boldsymbol{F}_i = -\nabla_i V_{\mathrm{SPC/E}}$ where

$$V_{\mathrm{SPC/E}} = V_{\mathrm{real}} + V_{\mathrm{k}} + V_{\mathrm{LJ}} \tag{2.74}$$

is the SPC/E potential energy function. All molecules are rigid in the SPC/E potential, and there are two ways to run dynamics with this constraint [1]. One way is to compute the forces on the center of mass for each molecule and the torques in the principal axis directions, and the other way uses "constraint dynamics." We have chosen to use constraint dynamics for their computational simplicity and efficiency. The equations of constraint are holonomic, meaning that they can be written as a set of equations [7]

$$|\boldsymbol{r}_\alpha - \boldsymbol{r}_\beta|^2 - d_{\alpha\beta}^2 = 0, \tag{2.75}$$

where $d_{\alpha\beta}$ is the distance between atoms α and β on the same molecule. The Lagrangian for the system with constraints is [4]

$$L(\boldsymbol{r}^N, \boldsymbol{v}^N) = \sum_i \frac{m_i \boldsymbol{v}_i^2}{2} - \frac{1}{2}\sum_i \sum_{j,j\neq i} V_{\mathrm{SPC/E}}(\boldsymbol{r}_i, \boldsymbol{r}_j) - \sum_{\alpha,\beta} \lambda_{\alpha\beta} V_{\mathrm{constraint}}(\boldsymbol{r}_\alpha, \boldsymbol{r}_\beta). \tag{2.76}$$

In Equation 2.76, i and j are the intermolecular indices and α and β are indices for the intramolecular atoms. The constraints have been absorbed into $V_{\mathrm{constraint}}(\boldsymbol{r}_\alpha, \boldsymbol{r}_\beta) =$

[4] One can rationalize this Lagrangian from Hamilton's principle. Hamilton's principle finds equations of motion by minimizing the action along a trajectory, $\delta S = \delta \int_{t_0}^{t} L(\boldsymbol{v}^N, \boldsymbol{r}^N, t) = 0$. Without constraints, Lagrange's equation (Eq. 2.77) minimizes the action, but with holonomic constraints the minimization can be accomplished by introducing Lagrange multipliers.

$|\boldsymbol{r}_\alpha - \boldsymbol{r}_\beta|^2 - d_{\alpha\beta}^2$. Lagrange's Equation is

$$\frac{d}{dt}\left(\frac{\partial L(\boldsymbol{r}^N, \boldsymbol{v}^N)}{\partial \boldsymbol{v}_i}\right) - \frac{\partial L(\boldsymbol{r}^N, \boldsymbol{v}^N)}{\partial \boldsymbol{r}_i} = 0. \tag{2.77}$$

Substituting the Lagrangian (Equation 2.76) into 2.77 yields Newton's equation of motion for atom i

$$m_i \frac{d^2\,\boldsymbol{r}_i(t)}{dt^2} = \boldsymbol{f}_i + \delta_{\alpha,i}\boldsymbol{g}_\alpha, \tag{2.78}$$

Where $\boldsymbol{f}_i = -\nabla_i V_{\text{SPC/E}}$ is the unconstrained force and $\boldsymbol{g}_\alpha = -\sum_\beta \lambda_{\alpha\beta}\nabla_\alpha V_{\text{constraint}}(\boldsymbol{r}_\alpha, \boldsymbol{r}_\beta)$ are the forces of constraint on atom i.

It is impossible to solve the equations of motion in a molecular system with a realistic potential and more than a few degrees of freedom exactly. Instead, MD algorithms use time-domain finite difference methods to solve the equations of motion approximately. A stable integrator that stores positions, velocities, and forces at each time step is the Velocity-Verlet integrator. In the Velocity-Verlet algorithm, the unconstrained positions ($\boldsymbol{r}_u^N$) and velocities ($\boldsymbol{v}_u^N$) advance according to[1]

$$\boldsymbol{r}_i(t+\delta t)_u = \boldsymbol{r}_i(t) + \boldsymbol{v}_i(t)\delta t + \frac{1}{2}\frac{\boldsymbol{f}_i(t)}{m_i}\delta t^2 \tag{2.79}$$

$$\boldsymbol{v}_i(t+\delta t)_u = \boldsymbol{v}_i(t) + \frac{1}{2}\left(\frac{\boldsymbol{f}_i(t)}{m_i} + \frac{\boldsymbol{f}_i(t+\delta t)}{m_i}\right)\delta t. \tag{2.80}$$

The next update incorporates the forces of constraint. The constrained positions advance according to

$$\boldsymbol{r}_i(t+\delta t) = \boldsymbol{r}_i(t)_u + \frac{1}{2m_i}\boldsymbol{g}_i^{(r)}(t)\delta t^2. \tag{2.81}$$

The velocities at time $t + \delta t$ follow a similar rule

$$\boldsymbol{v}_i(t + \delta t) = \boldsymbol{v}_i(t)_u + \frac{1}{2m_i}\boldsymbol{g}_i^{(v)}(t + \delta t)\delta t. \tag{2.82}$$

The RATTLE algorithm finds the the Lagrange multipliers for the constraint forces in $\boldsymbol{g}^{(v)}$ and $\boldsymbol{g}^{(r)}$ iteratively. I have found that only 3-6 iterations per atom are necessary to achieve a tolerance of $O(10^{-5})$ Å. Because the equations of motion are solved approximately, there is a finite probability of violating energy conservation so that the total energy of the system will continuously rise over the course of the simulation. For the time step that I have chosen ($\delta t = 3$ fs), the velocities have to be re-normalized by their thermal values every 10 ps. This re-scaling interval is an order of magnitude longer than the dynamics of interest and keeps the energy fluctuations to $O(10^{-4})$ of the total energy

Some tricks in MD simulations

There are a few tricks that I have used to speed up the MD simulations. The first is in storage for the positions, velocities, and forces. It is important to ensure that the array that stores these items enters the CPU cache at the beginning of a loop and remains there until the loop is finished. In C and C++, this corresponds to writing the multidimensional array with the spatial index last (i.e. r[nmolecules][natoms][3]).

It is time-consuming to evaluate transcendental functions, such as square roots. It is particularly costly in the inner loop of a force evaluation. The real space part of the Ewald sum is a pair-wise interaction that only depends on the separation

between atomic pairs. Calculating the separation between two atoms requires taking the square root, and the evaluation of the Ewald term is expensive because it contains several transcendental functions. For the real space part of the Ewald sum, I have built a look-up table to evaluate the value of the force and potential energies as a function of the distance squared between atomic pairs.

The $\boldsymbol{k}$-space part of the Ewald sum (Eq. 2.73) is a spatial Fourier transform of a real-valued quantity. As such, the potential energy is symmetric with inversion through $\boldsymbol{k} = 0$. In other words, $V_{\mathrm{k}} = V_{\text{-k}}$. I have used this symmetry and only done the $\boldsymbol{k}$-space part of the sum for half of the wavevectors. The second half is related by inversion. When building the Fourier coefficients, I have used the recursion relationship $e^{i(n+m)} = e^{in}e^{im}$. Examples of my code can be found at http://web.mit.edu/~joel/www/Thesis/Code.

Hydrogen bonding geometries and the first solvation shell

Typically, one identifies a hydrogen bond in water with the intermolecular oxygen distance $\mathrm{R_{OO}}$ and the cosine of the "hydrogen bonding angle", $\cos(\alpha)$. Figure 2-3 illustrates these coordinates. I will call these the "geometrical criteria." A conventional approach is to define a characteristic function, h [12] that is a binary variable deciding whether or not the chosen pair is hydrogen bonded according to (Figure 2-3)

$$h = \begin{cases} 1 & \text{if } \cos(\alpha) > \cos(30°) \text{ and } \mathrm{R_{OO}} < 3.5\mathring{A}; \\ 0 & \text{otherwise.} \end{cases}$$

In Chapter 4, we will interested in the molecules in the first solvation shell of

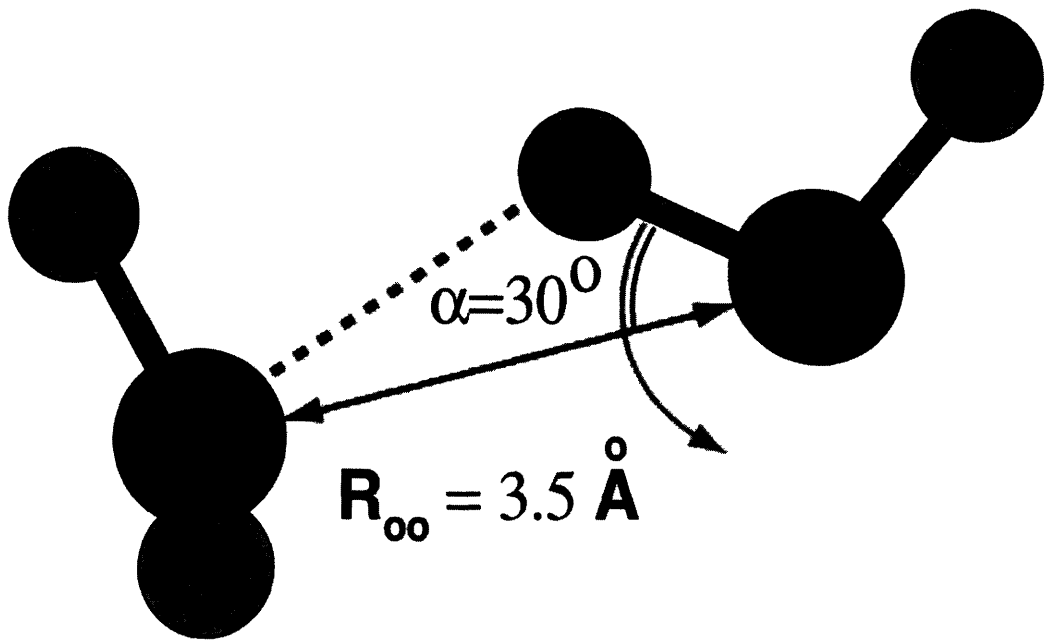

Figure 2-3: Illustration of the geometrical criteria for hydrogen bonding. The critical angle α is 30°, and the critical value of R_{OO} is 3.5 Å.

HOD in liquid D_2O. I have identified the "first solvation shell" as the four nearest neighbors surrounding the HOD molecule. Out of these, I have determined the hydrogen bonding partner by selecting the largest value of $\cos(\alpha)$ out of the four nearest neighbors. This selection strategy allows one to assign a hydrogen bonding partner even during transient fluctuations away from a hydrogen bond .

2.5 Calculating vibrational frequencies for HOD in liquid D_2O

We now specify our formalism to calculate the spectroscopy of the OH stretch of HOD in liquid D_2O. Recall the Hamiltonian (Eq. 2.36)

$$H = H_{\rm s}(\{P\},\{Q\}) + H_{\rm sb}(\boldsymbol{p}^N,\boldsymbol{r}^N,\{P\},\{Q\}) + H_{\rm b}(\boldsymbol{p}^N,\boldsymbol{r}^N). \qquad (2.83)$$

As before, {P} and {Q} are the momenta and atomic displacements of the vibrations in internal coordinates, and $\boldsymbol{p}^N$ and $\boldsymbol{r}^N$ are the classical momenta in atomic Cartesian coordinates. The "bath" Hamiltonian, $H_{\rm b}$, describes the translations and rotations of the molecules in the liquid, or the slow coordinates. The potential energy in $H_{\rm b}$ is a classical molecular dynamics potential (SPC/E). $H_{\rm s}$, the "system" Hamiltonian is the operator describing HOD's vibrational eigenstates in the gas phase. It is a function of the fast degrees of freedom, $\{P\}$ and $\{Q\}$. The system-bath Hamiltonian, $H_{\rm sb}$, couples the fast and slow coordinates. For HOD in liquid D_2O, there are two internal hydride stretch coordinates and a bend. The mechanical anharmonicity is large, but the kinetic coupling is small relative to the perturbations from the liquid environment (the experimental IR spectrum shifts ≈ 200 cm^{-1} to the red in going from the gas to the liquid), so we can neglect the kinetic coupling. Within these approximations the system Hamiltonian in Equation 3.1 is one-dimensional.

Often, the most practical and computationally efficient way to find $H_{\rm sb}$ is to expand the bath Hamiltonian as a Taylor series in the internal coordinates (and

possibly momenta) and quantize them [14] in the system basis set. $H_{\rm sb}$ is usually a slowly-varying function of the system coordinates and a low order approximation, usually first or second order, is sufficient. We truncate the expansion at second order in Q so that the system-bath Hamiltonian becomes

$$H_{\rm sb} = FQ + GQ^2. \tag{2.84}$$

To build the Q and Q^2 matrices, we used the local mode Hamiltonian of Reimers and Watts [16] and numerically integrated the eigenfunctions of the Morse oscillator from Watson, Henry, and Ross [21]. Figure 2-4 A is a diagram of the adiabatic scheme. We have chosen notation that is commensurate with Oxtoby's [14], where, F is the derivative of the potential energy at $Q = 0$, keeping the center of mass for the vibration fixed.

$$F = \frac{\partial V_{\rm SPC/E}(Q, \{\boldsymbol{r}\})}{\partial Q} = -\mu \hat{r}_{\rm OH} \cdot (\frac{\vec{F}_{\rm O}}{m_{\rm O}} - \frac{\vec{F}_{\rm H}}{m_{\rm H}}). \tag{2.85}$$

$\vec{F_{\rm O}}$ ($\vec{F_{\rm H}}$) is the force on the oxygen (hydrogen) atom and $m_{\rm O}$ ($m_{\rm H}$) is the mass of the oxygen (hydrogen) atom, $\hat{r}_{\rm OH} = \frac{\vec{r}_{\rm O} - \vec{r}_{\rm H}}{|\vec{r}_{\rm O} - \vec{r}_{\rm H}|}$ and μ is the reduced mass, $\frac{m_{\rm H} m_{\rm O}}{m_{\rm H} + m_{\rm O}}$. Analytical expressions for G appear in Appendix A. The first and second terms of F are the (mass-weighted) bath-induced forces on the oxygen and hydrogen atom, respectively, in the direction of the OH bond. In general, the magnitude of the OH component of the force for the hydrogen is comparable to that on the oxygen, but the inverse mass-weighting makes the second term larger. The forces on the hydrogen are purely

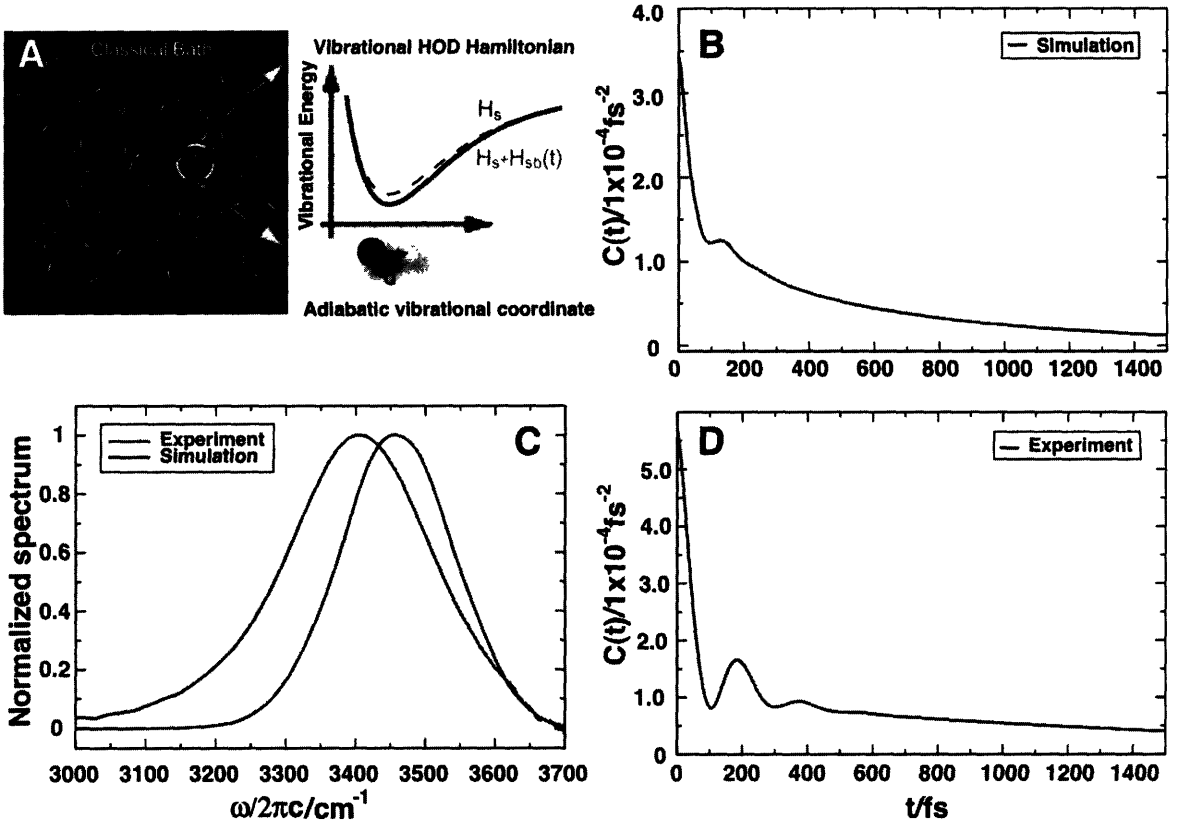

Figure 2-4: Schematic of the adiabatic separation used to compute the spectroscopy of HOD in D_2O (**A**), and a comparison to the experimental data from Fecko *et al.*[5] for both the correlation function (**B**) and (**D**) and the IR absorption lineshape (**C**). The lineshape in **B** is ≈ 200 cm^{-1} wide (FWHM) and exhibits some of the asymmetry in the experimental absorption experiment, but is nearly 70 cm^{-1} narrower and peaks roughly 30 cm^{-1} to the blue of the experimental spectrum. The correlation functions both have a sharp initial decay, a beat, and a longer time decay.

electrostatic, and so the vibrational frequency is particularly sensitive to the electric field evaluated at the proton. The dot product with $\hat{r}_{\mathrm{OH}}$ implies that electric fields in the direction of the OH bond make F the largest, and hence are most effective at inducing frequency shifts.

Once we have the system bath Hamiltonian, we solve the time independent Schrödinger equation for the vibrational eigenstates for the frozen or clamped configuration of the slow variables at time t, $\boldsymbol{r}^N(t)$.

$$(H_{\mathrm{s}}(\{P\},\{Q\}) + H_{\mathrm{sb}}(\{P\},\{Q\},\boldsymbol{r}^N;t))|\Psi(\boldsymbol{r}^N;t)\rangle = \mathcal{E}(\boldsymbol{r}^N;t)|\Psi(\boldsymbol{r}^N;t)\rangle. \qquad (2.86)$$

We assume that the couplings between the quantum mechanical oscillator and the classical degrees of freedom are weak enough that we can use the self-consistent mean field method of adiabatic quantum mechanics [20] without worrying about the forces of the OH oscillator on the atomic Cartesian coordinates. One can solve for these forces by applying the Hellman-Feynman theorem to the matrix elements of H_{sb} with the adiabatic quantum states in 2.86,

$$\boldsymbol{F}^i_{\text{Hellman-Feynman}}(t) = \langle\Psi(\boldsymbol{r}^N(t))|(-\nabla_i\ H_{\mathrm{sb}})|\Psi(\boldsymbol{r}^N(t))\rangle. \qquad (2.87)$$

Here, $\boldsymbol{F}^i_{\text{Hellman-Feynman}}(t)$ is the force from the quantum mechanical OH vibration on atom i, and ∇_i is the gradient with respect to atom i. As the appendix shows, computing derivatives of H_{sb} becomes cumbersome. Omitting the Hellman-Feynman forces means that the expectation value of the total Hamiltonian is not a constant

of the motion. The penalty for not including the Hellman-Feynman forces in the molecular dynamics is judged by the fluctuations in the total energy, given by the standard deviation of $\omega_{\rm OH}$, $\sigma_{\omega_{\rm OH}}$. $\sigma_{\omega_{\rm OH}}$ is $\approx$ 100 cm^{-1}, or about half k_BT. We address this issue by including the Hellman-Feynman forces in Chapter 3, where we show that their effects are small.

2.5.1 Comparison to experiment

We would like to compare predictions from MD simulation to experimental vibrational spectroscopic data for the OH stretch of HOD in liquid D_2O. The absorption spectrum is proportional to the Fourier transform of the dipole-dipole correlation function [23]

$$\sigma(\omega) \propto \omega \int_{-\infty}^{\infty} dt\, e^{i\omega t} \langle \boldsymbol{\mu}(t) \cdot \boldsymbol{\mu}(0) \rangle. \tag{2.88}$$

Using the Green operators in the adiabatic picture, the OH absorption lineshape is

$$\sigma(\omega) \propto \omega \int_{-\infty}^{\infty} dt\, e^{i\omega t} \langle exp(-\frac{i}{\hbar} \int_0^t dt'\, \mathcal{E}(\boldsymbol{r}(t')^N)_1 - \mathcal{E}(\boldsymbol{r}(t')^N)_0) \rangle \langle \cos(\boldsymbol{e}(t) \cdot \boldsymbol{e}(0)) \rangle e^{-\frac{t}{2T_1}}. \tag{2.89}$$

The vibrational lifetime T_1 is included as an empirical factor that represents how the flow out of the population $|1\rangle\langle 1|$ affects the coherence $|0\rangle\langle 1|$.

The lineshape computed from the simulation is roughly the same shape as the experimentally measured one, but is $\approx$ 70 cm^{-1} too narrow (FWHM). The reason for the discrepancy most likely lies in the width of the frequency distribution. This distribution is 265 cm^{-1} wide (Chapter 4), so spectral diffusion can only narrow

it. The experimental $C_{\omega\omega}(t)$ evaluated at $t = 0$ provides an estimate for the mean squared value of the distribution that is nearly 60 % larger than that computed from the simulation.

Recently, our group has measured the IR3PEPS and pump probe spectroscopy of the OH stretch in liquid D_2O [5]. From the data, Fecko *et al* extracted $C_{\omega\omega}(t)$.

$$C_{\omega\omega}(t) = \langle \delta\omega_{\mathrm{OH}}(t)\delta\omega_{\mathrm{OH}}(0)\rangle, \tag{2.90}$$

where $\delta\omega_{\mathrm{OH}}(t) = \omega_{\mathrm{OH}}(t) - \langle\omega_{\mathrm{OH}}\rangle$ [5, 4, 22].

To get $C_{\omega\omega}(t)$ from MD simulations, we can solve Equation 2.36 to any desired degree of accuracy. In this Chapter and in Chapter 4, we use second order time independent perturbation theory to approximately diagonalize H_{sb} at each time step. To second order the vibrational energies are

$$\mathcal{E}_n^{(2)} = \langle n|\ H_{\mathrm{sb}}(\boldsymbol{r}^N, Q; t)|n\rangle + \sum_{k,n\neq k} \frac{|\langle n|\ H_{\mathrm{sb}}(\boldsymbol{r}^N, Q; t)|k\rangle|^2}{\mathcal{E}_n^{(0)} - \mathcal{E}_k^{(0)}}. \tag{2.91}$$

Here $\{|n\rangle\}$ and $\mathcal{E}_n^{(0)}$ are the unperturbed states and energies, respectively. For the matrix elements of HOD, the second order term is usually smaller than the first order term so first order perturbation theory is reasonably accurate. Furthermore, differences in the diagonal matrix elements for Q^2 are smaller than those for Q for low-lying vibrational states. If we neglect the G term in Equation 2.84 and ignore

the forces on the oxygen atom, at first order the system-bath Hamiltonian is

$$E \equiv \hat{\boldsymbol{r}}_{\mathrm{OH}} \cdot \mathbf{E}, \tag{2.92}$$

$$H_{\mathrm{sb}} \approx z_{\mathrm{H}} Q E,$$

where the electric field, $\mathbf{E}$ appearing in equation 2.92 is that generated by all the molecules in the simulation and their periodic images and z_{H} is the charge of the proton. At this level of approximation, H_{sb} is isomorphic with the first order Stark shift Hamiltonian,

$$H_{\mathrm{Stark}} = -\boldsymbol{\mu} \cdot \mathbf{E}, \tag{2.93}$$

after making the substitution

$$-\boldsymbol{\mu} \cdot \mathbf{E} = z_H Q \hat{\boldsymbol{r}}_{OH} \cdot \mathbf{E}. \tag{2.94}$$

The correlation function from simulation decays initally with a fast time constant of 35 fs, has a beat that peaks near 125 fs, and has a long time decay of $\approx$ 600 fs. Figure 2-4 compares the experimental and simulated $C_{\omega\omega}(t)$. The correlation function extracted from the experiment decays with a fast time constant, exhibits a beat that peaks at 180 fs, and has a long time decay of 1.4 ps. Given the simplicity of our approximations, the agreement between experiment and simulation in Figure 2-4 for both the absorption spectrum and $C_{\omega\omega}(t)$ is notable. Because there have been several different approaches to computing the IR lineshape and $C_{\omega\omega}(t)$ with classical molecular dynamics potentials that all achieve similar results, the disagreement

between the simulation and experiment probably does not highlight a problem with the frequency calculation itself [17, 10]. There are several approximations that one has to make to extract $C_{\omega\omega}(t)$ from the experiment. Strictly speaking, the IR3PEPS experiment can only extract $C_{\omega\omega}(t)$ reliably when the pulses have infinite bandwidth, the frequency fluctuations obey Gaussian statistics, the lifetime of the excited state is very long on the time scale of frequency fluctuations, and the nonresonant background is small relative to the absorptive signal. These approximations are not quite satisfied for HOD in D_2O. Atomistic models based on simple strategies nonetheless reproduce many qualitative features in $C_{\omega\omega}(t)$ and give an explicit microscopic model that we use to analyze the vibrational spectroscopy of HOD in liquid D_2O.

Bibliography

[1] M.P Allen and D.J. Tildesley. *Computer Simulation of Liquids.* Oxford University Press, 1989.

[2] H.J.C. Berendsen, J.R. Grigera, and T.P. Straatsma. The missing term in effective pair potentials. *J. Phys. Chem.*, 91:6269–6271, 1987.

[3] S. A. Egorov, Eran Rabani, and B. J.. Berne. On the adequacy of mixed quantum-classical dynamics in condensed phase systems. *Journal of Physical Chemistry B*, 103:10978–10991, 1999.

[4] C.J. Fecko, J.D. Eaves, J.J. Loparo, A. Tokmakoff, and P.L. Geissler. Local and

collective hydrogen bond dynamics in the ultrafast vibrational spectroscopy of liquid water. *Science*, 301:1698–1702, 2003.

[5] C.J. Fecko, J.L. Loparo, S. R. Roberts, and A Tokmakoff. In press. *Journal of Chemical Physics*, 2004.

[6] Sarah M. Gallagher Faeder and David M. Jonas. Phase-resolved time-domain nonlinear optical signals. *Phys. Rev. A.*, 62:033820, 2000.

[7] Herbert Goldstein. *Classical Mechanics.* Addison-Wesley Publishing Company, 1980.

[8] O. Golonzka and A. Tokmakoff. Polarization-selective third-order spectroscopy of coupled vibronic states. *J. Chem. Phys.*, 115(1):297–309, 2001.

[9] L. Landau and E. Teller. Zur theorie der schalldispersion. *Physik. Z. Sowjetunion*, 10:34, 1936.

[10] C. P. Lawrence and J. L. Skinner. Vibrational spectroscopy of HOD in liquid D_2O. I. vibrational energy relaxation. *Journal of Chemical Physics*, 117:5827–5838, 2002.

[11] J. J. Loparo, C. J. Fecko, J. D. Eaves, S. T. Roberts, and A. Tokmakoff. Reorientational and configurational fluctuations in water observed on molecular length scales. *Physical Review B*, 2004.

[12] Alenka Luzar and David Chandler. Hydrogen-bond kinetics in liquid water. *Nature (London)*, 379:55–7, 1996.

[13] Shaul Mukamel. *Principles of Nonlinear Optical Spectroscopy.* Oxford University Press, 1998.

[14] D. W. Oxtoby. Dephasing of mol. vib. in liquids. *Adv. Chem. Phys.*, 40:1, 1979.

[15] William H. Press, Saul A. Teukolsky, William T. Vetterling, and Brian P. Flannery. *Numerical Recipes in C++, The Art of Scientific Computing.* Cambridge University Press, 2nd edition, 2002.

[16] J. R. Reimers and R.O. Watts. A local mode potential function for the water molecule. *Mol. Phys.*, 52(2):357–381, 1984.

[17] Rossend Rey, Klaus B. Moller, and James T.. Hynes. Hydrogen bond dynamics in water and ultrafast infrared spectroscopy. *Journal of Physical Chemistry A*, 106:11993–11996, 2002.

[18] Jun John Sakurai. *Modern Quantum Mechanics.* Addison-Wesley Publishing Company, 1994.

[19] Jaeyoung Sung and R. J. Silbey. Four-wave mixing spectroscopy for a multi-level system. *J. Chem. Phys.*, 115:9266–9287, 2001.

[20] John Tully. Mixed quantum-classical dynamics. *Faraday Discussions*, 110:407–419, 1998.

[21] I.A. Watson, B.R. Henry, and I.G. Ross. Local mode behavior - the morse oscillator model. *Spectrochimica Acta Part A - Molecular and Biomolecular Spectroscopy*, 37(10):857–865, 1981.

[22] Sergey Yeremenko, Maxim S. Pshenichnikov, and Douwe A. Wiersma. Hydrogen-bond dynamics in water explored by heterodyne-detected photon echo. *Chem. Phys. Lett.*, 369:107–113, 2003.

[23] Robert Zwanzig. *Nonequilibrium statistical mechanics.* Oxford University Press (New York), 2001.

Chapter 3

Adiabatic quantum mechanics and the vibrational spectroscopy of water

Onsager's regression hypothesis relates transport, kinetics, and other non-equilibrium phenomena to fluctuations at equilibrium [6, 1]. Many successful theories recast non-equilibrium dynamics in terms of a minimal set of equilibrium correlation functions [5, 6, 1, 9]. Spectroscopic experiments generally measure the response of a sample to a weak perturbing field. The fluctuation-dissipation theorem and linear response relate the rates of energy gain or loss from the field to the equilibrium fluctuations.

In the condensed phase, researchers have traditionally relied on classical MD simulations to translate experimentally measured quantities such as vibrational lifetimes and dephasing correlation functions into atomistic information about molecular liquid

motions. Theoretically, it has been a challenge to formulate a protocol that treats the quantum mechanical coordinates of the vibrations and the classical translations and rotations of molecules consistently.

Classical MD simulations are most reliable in cases where the electronic degrees of freedom are fast relative to any other motion and there is not significant electron correlation between molecules. In these situations, simple empirical and electrostatic potentials represent the average over the quantal electronic degrees of freedom. The vibrational stretch coordinates are typically constrained to be rigid because the energetic cost for deforming a molecule is high relative to thermal energy. Introducing a vibrational degree of freedom into a classical simulation presents new challenges that must be addressed. The theory must not only describe how the quantum mechanical vibrations depend on the classical degrees of freedom, but also how the classical coordinates depend on the quantum mechanical ones. This latter requirement is the most challenging.

We use an approach that treats the classical and quantum mechanical coordinates self-consistently. We solve the problem by allowing the classical coordinates to evolve according to Newtons equation. For various configurations of the liquid simulation, we solve the time independent Schrödinger equation for the vibrations and then compute the forces from these coordinates on the classical degrees of freedom with the Hellman-Feynman theorem. The expectation value of the Hamiltonian is a constant of the motion, and hence the classical dynamics are self-consistent.

3.1 Methods

Recall the system bath Hamiltonian used extensively in Chapter 2.

$$H = H_s(P,Q) + H_{sb}(Q,\boldsymbol{r}^N) + H_b(\boldsymbol{p}^N,\boldsymbol{r}^N). \tag{3.1}$$

P and Q are the momenta and positions of the vibrations in internal coordinates, and $\boldsymbol{p}^N$ and $\boldsymbol{r}^N$ are the classical momenta and coordinates. The "bath" Hamiltonian H_b describes the translations and rotations of the molecules in the liquid, or the slow coordinates. We will employ the SPC/E potential for H_{b}. H_{s}, the "system" Hamiltonian is a matrix for the vibrational eigenstates of the molecule in the gas phase. It is a function of the fast degrees of freedom, P and Q. The system-bath Hamiltonian, H_{sb}, couples the fast and slow coordinates. We have found H_{sb} by direct expansion but instead of the Hamiltonian $H_{\mathrm{sb}} = FQ + GQ^2$, we truncated the expansion at first order so that $H_{\mathrm{sb}} = FQ$. We did this because computing higher derivatives of the potential energy in the MD simulation is computationally expensive, and the first order term should be sufficient for qualitative accuracy.

As before, we solve the time-independent Schrödinger equation for the vibrational eigenstates for the frozen or clamped configuration of the slow variables,

$$H|\Psi(\boldsymbol{r}^N;t)\rangle = \mathcal{E}((\boldsymbol{r}^N;t)|\Psi(\boldsymbol{r};t)\rangle. \tag{3.2}$$

The eigenstates and energies are functions of the bath state at time t, $\boldsymbol{r}^N(t)$. After

averaging over the fast degrees of freedom, we impose total energy conservation.

$$\frac{d\langle H\rangle}{dt} = \sum_i \frac{\partial\langle H\rangle}{\partial \boldsymbol{p}_i} \cdot \dot{\boldsymbol{p}}_i + \frac{\partial\langle H\rangle}{\partial \boldsymbol{r}_i} \cdot \dot{\boldsymbol{r}}_i = 0. \tag{3.3}$$

The brackets $\langle ... \rangle$ represent the expectation value of the Hamiltonian and the dot denotes a derivative with respect to time. Equation 3.3 says that if the bath can change the vibrational frequencies over a given time interval, the vibration must do work on the bath over that same interval so that the total energy remains conserved. Evidently, Eq. 3.3 returns Hamilton's equations for $\boldsymbol{r}^N$ and $\boldsymbol{p}^N$. We use them to propagate the dynamics of the classical degrees of freedom by calculating the forces on atom i,

$$\vec{F}_i = -\sum_{j,j\neq i} \frac{\partial H_b}{\partial \boldsymbol{r}_j} + \frac{\partial\langle H_{sb}\rangle}{\partial \boldsymbol{r}_j}. \tag{3.4}$$

The first term is the conventional force from the MD potential, but the second term is the force from the quantum system on the classical variables. We can re-write it using the Hellman-Feynman theorem.

$$\frac{\partial\langle H_{sb}\rangle}{\partial \boldsymbol{r}_j} = \langle \Psi(\boldsymbol{r}^N; t) | \frac{\partial H_{sb}}{\partial \boldsymbol{r}_j} | \Psi(\boldsymbol{R}(t)) \rangle. \tag{3.5}$$

Formally, these equations are a closed self-consistent solution for both the vibrational energies and classical dynamics. However, it is difficult to exactly diagonalize the Hamiltonian for arbitrary configurations of the bath, and some approximation is necessary. Expanding the eigenstates with time-independent perturbation theory in H_{sb}, we solve for the energies in Eq. 3.2 and forces in Eq. 3.4 to arbitrary order in

perturbation theory. If H_{sb} is not perturbative, the solution is more difficult.

Although this method couples the quantal and classical coordinates in a self-consistent way, it suffers from the usual problems of a mean-field approach [7]. Specifically, we neglect coherences between the classical and quantum mechanical coordinates. As a result, TCFs calculated with this technique do not satisfy microscopic reversibility because the mean field Hamiltonian in Equation 3.3 is symmetric under time reversal.

It is most convenient to neglect the forces from the quantum mechanical coordinates on the bath. Indeed, these forces are frequently ignored. One can argue that this omission may not be important when studying equilibrium fluctuations, however, Hellman-Feynman forces appearing in Equation 3 should not be neglected if one is interested in vibrational relaxation rates. While a comprehensive atomistic model of vibrational spectroscopy must include these processes, we neglect them for the time being and focus on the equilibrium problem self-consistently. It is easy to introduce vibrational relaxation through Landau-Teller [3] theory based on Equation 3.

3.2 Linear Response Theory

Conceptually, spectroscopies designed to measure spectral diffusion are variants of hole-burning experiments. In these experiments, one saturates parts of the absorption band and monitors the time dependent spectrum as it recovers to equilibrium (Figure 3-1 A). In a transient hole burning experiment, one measures the time dependent average frequency of the hole as spectral diffusion proceeds, $\overline{\omega(t)}$. The overbar reminds

us of the non-equilibrium average.

Bakker's transient hole burning work on water infers a rather large vibrational Stokes shift for the OH stretch of HOD in D_2O [8]. If the HOD molecule appears much different in vibrationally excited states than in the ground state, the Stokes shift will be large. If the Stokes shift is very large, the excitation of the OH stretch may push the system away from equilibrium so that spectral dynamics will not reflect the more interesting equilibrium fluctuations of the system.

The total Hamiltonian in Equation 3.2 depends on the vibrational state of the molecule. We can write the average energy difference between the ground and first excited state as

$$H(t) = \langle 0(t)|H|0(t)\rangle - \theta(t)(\langle 0(t)|H|0(t)\rangle - \langle 1(t)|H|1(t)\rangle), \tag{3.6}$$

where the function $\theta(t)$ is the auxiliary field that brings the system from v =0 to v =1 (Figure 3-2 B). If a laser pulse burns a hole at t=0, $\theta(t)$ is the heavyside step function. Dynamic linear response theory based on equation 3.6 relates the hole-burning measurement to equilibrium fluctuations of the energy difference between v =0 and v =1.

$$S(t) = \frac{\overline{\omega_{\mathrm{OH}}(t)} - \overline{\omega_{\mathrm{OH}}(\infty)}}{\overline{\omega_{\mathrm{OH}}(0)} - \overline{\omega_{\mathrm{OH}}(\infty)}} \approx \frac{\langle \delta\omega_{\mathrm{OH}}(t)\delta\omega_{\mathrm{OH}}(0)\rangle}{\langle \delta\omega_{\mathrm{OH}}^2\rangle}. \tag{3.7}$$

Here, $\omega_{\mathrm{OH}}(t) = (\langle 1(t)|H|1(t)\rangle - \langle 0(t)|H|0(t)\rangle)$ and $\delta\omega_{\mathrm{OH}}(t) = \omega_{\mathrm{OH}}(t) - \langle\omega_{\mathrm{OH}}\rangle$, and the Stokes shift is $\overline{\omega_{\mathrm{OH}}(0)} - \overline{\omega_{\mathrm{OH}}(\infty)}$.

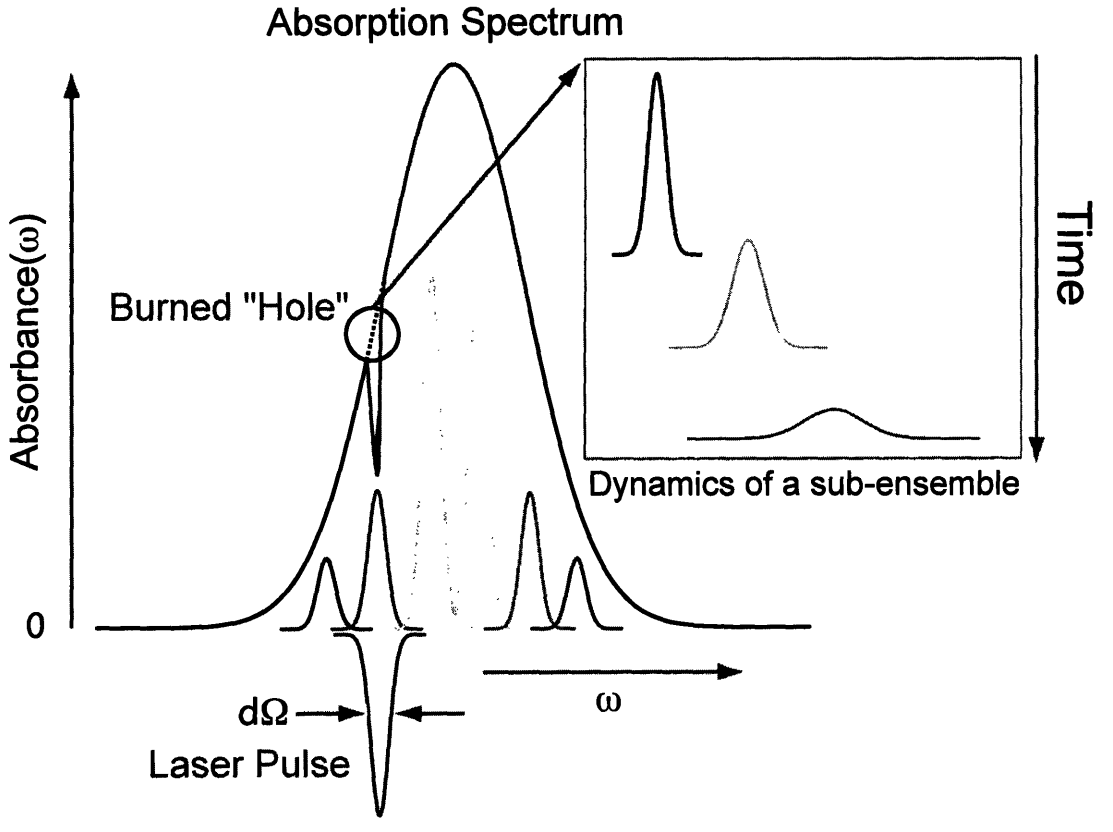

Figure 3-1: Experiments designed to measure spectral diffusion are variants of a hole burning experiment. In the hole burning experiment, a pump laser saturates a transition, and a probe beam delayed with respect to the pump records the spectrum's return to equilibrium (inset).

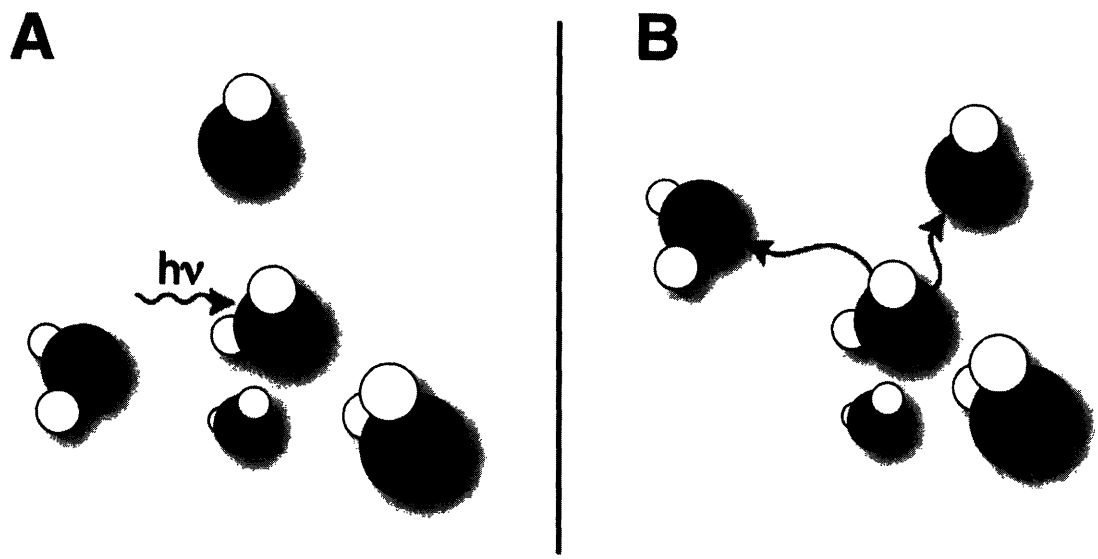

Figure 3-2: Cartoon of solvent reorganization after vibrational excitation. In a spectral diffusion experiment, a laser pulse excites a molecule at t=0 (left panel). The surrounding molecules rearrange to accommodate the molecule in the excited state (right panel). If the excitation does not drive the system too far from equilibrium, the time dependent reorganization seen in hole-burning experiments is the same as the equilibrium frequency fluctuations.

We ran MD simulations on a system of 107 D_2O molecules and one HOD molecule. The RATTLE algorithm propagated the dynamics of the classical degrees of freedom, but at each time step we added to these the Hellman-Feynman force from the OH oscillator. We equilibrated 5000 independent trajectories in v =0. After equilibration, we switched the HOD molecule in each trajectory into v =1 and calculated $S(t)$ by averaging the time-dependent transition frequency over the trajectories.

These data are preliminary. I have noticed that the total energy in the system does not remain constant, but there is a long time instability that appears after $\approx$ 1 ns of simulation time that causes the total energy to decrease by $\approx$ 40 % before it plateaus. This instability is likely a bug in the program, but has been very difficult to isolate.

Figure 3-3 shows the results of the calculation. From the calculation, the Stokes shift was 24 cm^{-1}, about a factor of three smaller than Bakker's estimate. If we expand H_{sb} to second-order in Q, but neglect the Hellman-Feynman forces, the linear response estimate of the Stokes shift is $\approx$ 50 cm^{-1} [4].

In studies of elecronic solvation dynamics, where an organic dye molecule replaces the HOD, researchers have found significant deviations between $S(t)$ and the normalized correlation function [2]. The deviations are most severe when the molecule either changes shape upon excitation, or acquires a dramatically different dipole moment in the excited state. The Stokes shift in electronic experiments is about an order of magnitude larger than we predict for HOD in D_2O. From this perspective, it is not surprising that the agreement between $S(t)$ and the normalized frequency correlation

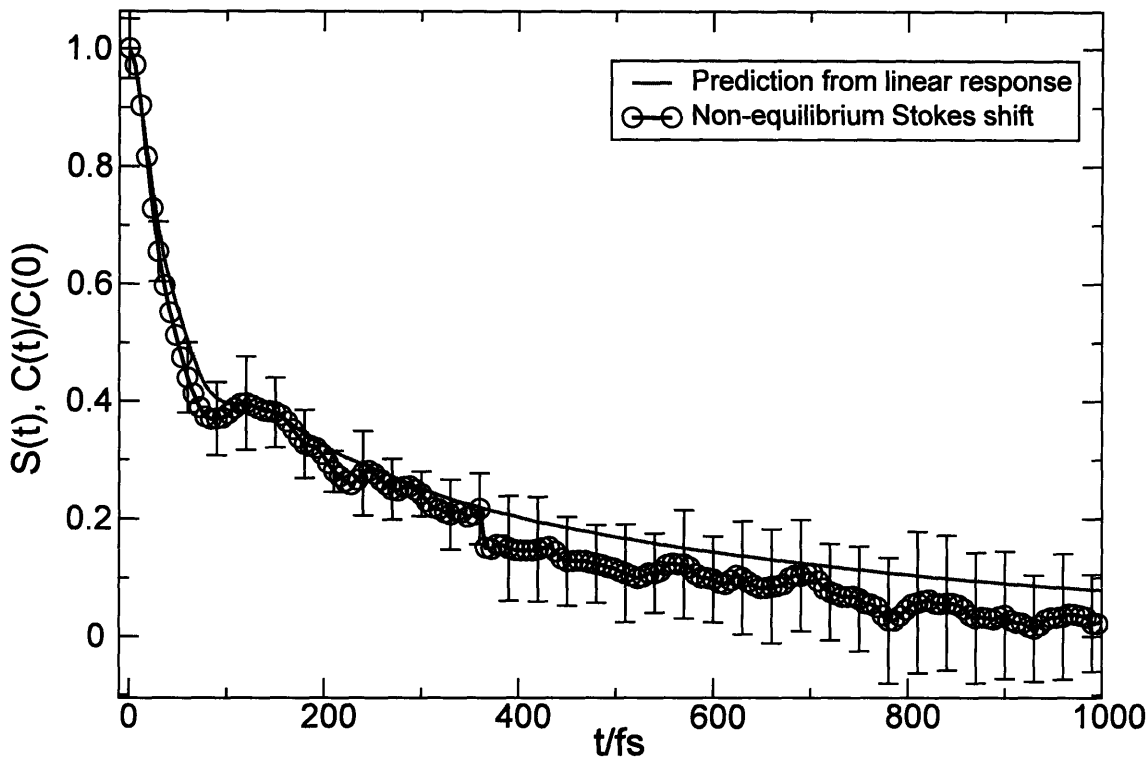

Figure 3-3: Testing linear response for the vibrational spectroscopy of the OH stretch of HOD in D_2O according to Equation 3.7 (preliminary data). The molecule enters ν =1 at t=0. The average is non-stationary because the solvent must reorganize to accommodate the excited HOD molecule. The non-equilibrium average is over 5000 trajectories where the HOD molecule enters the first vibrationally excited state at t=0. Error bars are one standard deviation. The solid line shows the normalized frequency-frequency correlation function of the molecule in ν =0, C(t)/C(0). Linear response accurately describes spectral diffusion because when HOD enters ν =1, it does not perturb the solvent much.

function is so good. It confirms our notion that spectroscopy of low energy vibrational states yields information about equilibrium fluctuations in liquid water.

In conclusion, we have presented a self-consistent method for computing vibrational frequencies that borrows many ideas from the theory of electronic structure [7]. Imposing energy conservation on the expectation value of the Hamiltonian gives the forces from the quantum mechanical coordinates on the classical degrees of freedom. We test the predictions of linear response for the vibrational spectroscopy of HOD in liquid D_2O and find that nonlinear spectroscopies designed to measure spectral diffusion do not drive the system out of the linear response regime.

Bibliography

[1] David Chandler. *Introduction to modern statistical mechanics.* Oxford University Press (New York), 1987.

[2] Phillip L. Geissler and David Chandler. Importance sampling and theory of nonequilibrium solvation dynamics in water. *Journal of Chemical Physics*, 113:9759–9765, 2000.

[3] L. Landau and E. Teller. Zur theorie der schalldispersion. *Physik. Z. Sowjetunion*, 10:34, 1936.

[4] C. P. Lawrence and J. L. Skinner. Ultrafast infrared spectroscopy probes hydrogen-bonding dynamics in liquid water. *Chemical Physics Letters*, 369:472–477, 2003.

[5] Shaul Mukamel. *Principles of Nonlinear Optical Spectroscopy.* Oxford University Press, 1998.

[6] Linda E. Reichl. *A Modern Course in Statistical Physics.* John Wiley and Sons-Interscience, 2nd edition, 1992.

[7] John Tully. Mixed quantum-classical dynamics. *Faraday Discussions*, 110:407–419, 1998.

[8] S. Woutersen and H. J. Bakker. Hydrogen bond in liquid water as a brownian oscillator. *Phys. Rev. Lett.*, 83:2077–2081, 1999.

[9] Robert Zwanzig. *Nonequilibrium statistical mechanics.* Oxford University Press (New York), 2001.

Chapter 4

Electric fields drive vibrational dephasing

Hydrogen bonds are the scaffolding of life, bridging adjacent strands of nucleic acids, stiffening proteins and functionalizing enzymes. Liquid water forms a network of hydrogen bonds that connect molecular participants together. By simulating empirical models of water, researchers have made substantial progress in identifying the molecular motions and fluctuations that generate fleeting fractures in the network and entice molecules to "change allegiances" by trading hydrogen bonding partners [36, 44, 31, 43]. Unfortunately experiments by themselves have been relatively unfruitful in revealing truly microscopic motions in water. Thermal averaging in linear spectroscopies and scattering experiments makes it impossible to detect signatures from groups of molecules in subtly different environments [46, 6, 19, 40]. However, provided there is a well-defined relationship between the vibrational transition frequency and molecular liquid structure, nonlinear IR spectroscopy overcomes this

obstacle by coherently preparing molecules in spectrally distinct environments and measuring their subsequent relaxation dynamics [14]. From this perspective, the frequency becomes a marker through which one can monitor the dynamics of the liquid as it moves through its myriad of possible configurations.

The coordinates that are often used to identify a hydrogen bond between two water molecules depend only on the relative distance and orientations of two molecules (Chapter 2). On the length scales of these connections ($\approx$ 3 Å) one imagines that the availability of nearby hydrogen bonds dictates the structure and dynamics of the liquid, but a hydrogen bonded pair also interacts with more distant partners through a network of hydrogen bonds. The fluctuations of the network can entice the hydrogen bonded pair to sever its hydrogen bond and accept new bonds from new partners. It is from this viewpoint that we describe the molecular environments in water the terms local and collective. We imagine that there is at least a conceptual separation between the HOD and its proximal hydrogen bonding partner (bonded to H) and the remainder of the liquid.

Experiments and computer simulations[11, 25, 8], have found that on molecular length scales water molecules undergo fast (tens of fs), localized intermolecular vibrations but on length scales larger than one solvation shell, descriptive variables are no longer molecular in origin. This is the regime of density and polarization fluctuations, where groups of molecules move in concert. Such long ranged fluctuations can cause instabilities in a hydrogen bond and force molecules to find new hydrogen bonding partners, thereby reorganizing the local structure.

Examples where collective motions of water molecules dominate observables that

are ostensibly molecular come from electron transfer and solvation dynamics [45]. In the Marcus scenario, long wavelength electric field fluctuations drive electron transfer and stabilize the reactants and products of a chemical reaction when the participants are adjacent to one another in the liquid [45]. The work of Balucani *et al.*[3] provides another example. By using the theory of Gaskell and Miller [17, 16], they were able to describe the center of mass velocity autocorrelation function of water in terms of collective and longitudinal currents. The competition between longitudinal and collective currents at early times produces fast fluctuations of the interatomic distance between oxygen pairs. These fluctuations support anomalously high wavevector acoustic modes and produce the "beat" seen in the velocity autocorrelation function [4, 5]. It might seen natural to assume that the beating motion is very delocalized, but the dispersion relationship shows that it only involves molecules in the first and second solvation shells [40].

The earlier work of Badger [2] and Rundle [34] identified quantitative relationships between the degree of hydrogen bonding and the OH stretch frequency (ω_{OH}), but in 1974, Novak [35] showed that for hydrogen bonding solids there is a strong correlation between the oxygen-oxygen distance, R_{OO}, (Figure 4-2) and ω_{OH}. Eager to observe hydrogen bond breaking in real time, experimentalists turned to time resolved transient hole burning (THB), a technique popularized in the studies of structural dyanmics in low temperature glasses and biological photochemistry [48, 20]. In these experiments, a narrow band pump pulse saturates a fraction of the molecules in a broad absorption band. Thermal agitation causes molecules to lose memory of their initial environments. When this happens their frequencies shift and the spectral

"hole" fills back up. If lifetime of the transition is much longer than the time scales for spectral diffusion, linear response theory relates the rate of spectral relaxation in a THB experiment to the equilibrium frequency fluctuations [14].

In 1991, Lauberau published the first IR transient hole burning experiment on the OH stretch of HOD in liquid D_2O, a model system for studying dynamics in water with IR spectroscopy. From his data, he inferred a time scale for single hydrogen bond breaking and multi-component structural rearrangement because he assigned spectral components to different types of hydrogen bonds [18]. The study reports several time scales for spectral relaxation in water, but the shortest time scale they report is close to their time resolution ($\approx$ 1 ps). Other THB experiments give a time scale of between 500 fs and $\approx$ 700 fs for the long time component of spectral diffusion [49, 15]. These experiments argued that the 700 fs – 1 ps decay corresponds to the hydrogen bond kinetic making and breaking rate between HOD and it's hydrogen bonding partner, but such an interpretation relies heavily on a strong correlation between the geometrical variables that identify a hydrogen bond and ω_{OH} that is unique and persistent on the time scale that the hydrogen bond remains intact ($\approx$ 1 ps). For Laubereau's interpretation to be accurate, there must also be a strong correlation between ω_{OH} and the degree of tetrahedrality in the first solvlation shell of HOD.

Recently, several computational studies on the nonlinear IR spectroscopy of HOD in liquid D_2O have appeared [26, 27, 29, 28, 38, 39]. These studies present a simple picture of vibrational dephasing, where the short time decay arises from fluctuations in the distance between the centers of HOD and its hydrogen bonding partner, and the

long time relaxation measures hydrogen bond breaking [28, 29]. These investigations have argued for an entirely local picture for vibrational spectroscopy in water, where the only important participants are the HOD molecule and its hydrogen bonding partner. A number of studies also have used MD simulations to examine the relationship between R_{OO} and ω_{OH} in the liquid phase. The studies have determined that the correlation between R_{OO} and ω_{OH} remains present but becomes more modest in the liquid [38, 29], but ultimately reach the same conclusion as the experimentalists about the long time decay of frequency fluctuations.

With an atomistic model of the vibrational spectroscopy of the OH stretch, we find a reasonably good correlation between the OH frequency and the geometrical hydrogen bonding variables, $\cos(\alpha)$ and R_{OO}, but these correlations are just a manifestation of the much stronger relationship between the frequency and the electric field that the molecules in the liquid impart on the proton. With the exception of the hydrogen bonding partner, molecules in the first solvation shell do not exert a large influence on the OH stretching frequency. Thus, IR experiments on the OH stretch are not sensitive to specific dynamics of hydrogen bonding partners not directly bonded to the proton. We conclude that electric field fluctuations drive the loss of vibrational coherence at all times. At short times these fluctuations reflect changes in local geometries between HOD and its hydrogen bonding partner. Of course, local geometrical reconfigurations are not independent from larger length scale polarization and density fluctuations that dominate relaxation on picosecond time scales. Electrostatics couple these two relaxation mechanisms. The vibrational dephasing of HOD in liquid D_2O closely resembles Marcus' picture of electron transfer [45]. Our

picture is highly suggestive of a reduced model for the vibrational spectroscopy of water, where the only essential molecular feature is the hydrogen bonding interaction between HOD and a single neighbor.

4.1 Results

Chapter 2 described our adiabatic model and MD methods to calculate the frequency-frequency correlation function for the OH stretch. The qualitative agreement between the simulation and the experiment is notable (Fig. 2-4). Equipped with an explicit microscopic model, we examine the relationship between frequency and molecular hydrogen bonding environments. Our analysis proceeds by defining a set of physically motivated order parameters that classify the liquid environment. We then look for statistical correlations between these order parameters and ω_{OH}. After establishing the statistical significance of our chosen order parameters, identify a set of relevant order parameters – those that are strongly correlated with ω_{OH}. We then compare the characteristic time scales of frequency fluctuations to those of the relevant order parameters.

4.1.1 The role of the hydrogen bonding partner

Our atomistic model allows us to explore the connection between ω_{OH} and hydrogen bonding structure in detail. Let us suppose that one could select a distribution of molecules by labeling them with a short pulse laser that has arbitrary time and frequency resolution. Figure 4-1 is a three dimensional probability density of the

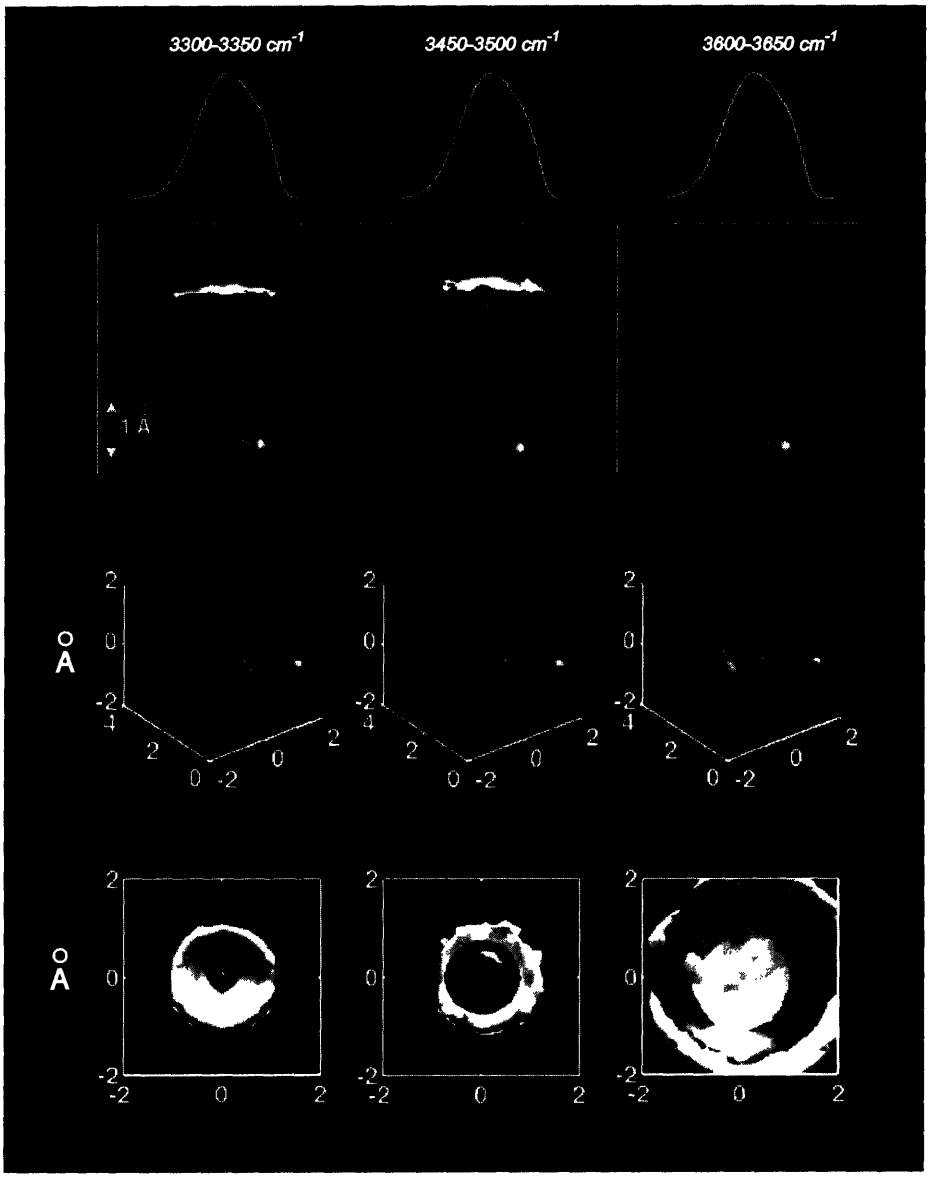

Figure 4-1: Still lifes of hydrogen bonded configurations visualized through the OH frequency. This plot shows atomic probability densities of HOD's nearest hydrogen bonding partner for various ranges of ω_{OH}. Surfaces represent the full width at half maximum of the atomic probability density for the neighbor's hydrogens (white) and oxygens (red). The first row is the distribution of $\frac{\omega_{OH}}{2\pi c}$, which peaks at 3450 cm^{-1} and is 265 cm^{-1} wide (FWHM). The arrows designate the OH frequency for each column. Numbers on the axes are distances in Å for a coordinate system centered on HOD's oxygen atom. The fourth row is the molecular configurations viewed from the perspective of the OH bond. Spectral diffusion of ω_{OH} is the time evolution over molecular geometries depicted in this figure. The blue side of the line shows cleaved or severely strained hydrogen bonds. Clearly, ω_{OH} is not a simple function of R_{OO} for all frequencies.

atomic distributions for the hydrogen bonding partner on the red, middle, and blue side of the absorption line, calculated from our simulations. Each column in Figure 4-1 is the collection of molecules in a 50 cm^{-1} wide bin about the selected frequencies (3300, 3450 and 3600 cm^{-1}). Isosurfaces represent the full width at half maximum surface for the atomic density of the hydrogen bonding parther's hydrogen (white) and oxygen (red) atoms. Progressing from the red side of the line to the blue side of the line, the oxygen density goes from being tightly localized to diffuse. All the surfaces seem to exhibit nearly azimuthal symmetry about the OH bond. The hydrogens of the nearest neighbor point away from the HOD molecule and do not significantly shift the frequency on the red or middle of the band, but become more important on the blue side of the line, filling the space that the oxygen atom does in the strongly hydrogen bonded case. We imagine that the structure that these densities depict comes from a progressive weakening in hydrogen bonds in moving from the red side to the blue side. It is obvious from these surfaces that R_{OO} is not the only coordinate that determines ω_{OH}. Moving from red to blue, the correlation with the hydrogen bonding angle, α, becomes more significant as R_{OO} becomes less significant. A successful variable that describes the relationship between ω_{OH} and local intermolecular structure must at least be a function of R_{OO} and α.

Recall that R_{OO} and α are convenient descriptors of hydrogen bonding in computer simulations. To examine the relationship between hydrogen bonding coordinates and the frequency, we computed joint probability distributions of ω_{OH} and local hydrogen bonding variables R_{OO} and $\cos(\alpha)$. Figure 4-2 shows the results. We calculated the joint probability distributions by making bivariate histograms of the

order parameters and ω_{OH}. The correlation coefficient, $\rho = \frac{\langle (x - \langle x \rangle)(\omega_{OH} - \langle \omega_{OH} \rangle) \rangle}{\sigma_x \sigma_{\omega_{OH}}}$ quantifies the staistical correlation between a chosen order parameter x and ω_{OH}. σ_x and $\sigma_{\omega_{OH}}$ are the standard deviations of x and ω_{OH}. If ω_{OH} is a linear function of x, then $\rho^2 = 1$. ρ is normalized to -1 for anti-correlated variables to +1 for perfectly correlated ones. $\rho = 0$ indicates statistical independence of x and ω_{OH}.

The statistical correlation between R_{OO} and ω_{OH} is reasonably strong ($\rho = 0.77$), but weakens at higher values of frequency and $OH \cdots O$ distance. Several researchers have examined this relationship in detail with several different models and approaches to the frequency calculation [32, 38, 29]. Their results are virtually identical to those displayed in Figure 4-2 B. Comparing Figure 4-2 with the predictions from Novak's [35] crystalline data suggests that the loss of sharp correlation between R_{OO} and ω_{OH} in the liquid comes from the higher degree of molecular disorder in the liquid. In the liquid state, molecules explore larger hydrogen bonding angles (α) than in the crystal phase. Figure 4-2 shows that as R_{OO} becomes larger, deviations in the polar angle, α are more severe, weakening the hydrogen bond.

Lawrence and Skinner [29] presented a graph similar to that displayed in 4-2, but with $P(\omega_{OH}, \alpha)$ instead of $P(\omega_{OH}, \cos(\alpha))$. $P(\omega_{OH}, \alpha)$ is zero at $\alpha = 0$. To realize a probability distribution consistent with the angular distributions of Figure 4-1, it is important to compute the joint probability density for the angular variable as a function of $\cos(\alpha)$, and not α. The reason for this lies in the Jacobian that relates the two probability densities.

$$P(\cos(\alpha), \omega_{OH}) d(\cos(\alpha)) d\omega_{OH} = P(\alpha, \omega_{OH}) |\sin(\alpha)| d\alpha d\omega_{OH}. \tag{4.1}$$

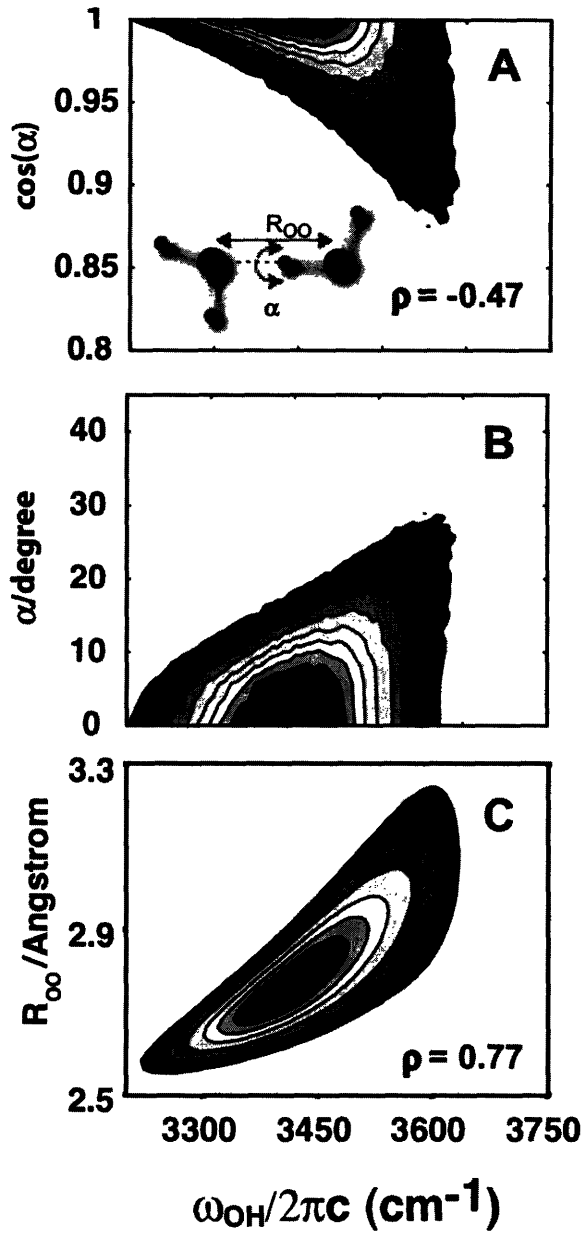

Figure 4-2: Joint probability distribution for intermolecular hydrogen bonding variables R_{OO} and $\cos(\alpha)$ with ω_{OH}. The geometrical criterion for hydrogen bonding identifies hydrogen bonded pairs based on the values of R_{OO} and $\cos(\alpha)$ **(A)** defines α and R_{OO} and displays $P(\omega_{OH}, \cos(\alpha))$. The correlation coefficient is -0.47. **(B)** Is a linear interpolation of $P(\omega_{OH}, \cos(\alpha))$ to linear spacing in α. It does not contain the Jacobian for the transformation, and hence is nonzero at $\alpha = 0$. **(C)** R_{OO} shows the stronger correlation to ω_{OH} than **(A)** with $\rho = 0.77$. At higher values of ω_{OH} the correlation between ω_{OH} and R_{OO} grows weaker while that between ω_{OH} and $\cos(\alpha)$ becomes stronger.

$P(\alpha, \omega_{\mathrm{OH}})|\sin(\alpha)|d\alpha d\omega_{\mathrm{OH}}$ is the probability of finding a configuration with a value of ω_{OH} in the interval $[\omega_{\mathrm{OH}}, \omega_{\mathrm{OH}} + d\omega_{OH})$ and a value of α in $[\alpha, \alpha + d\alpha)$. When α tends towards zero in linear strong hydrogen bonds, the probability density tends towards zero as $|\sin(\alpha)|d\alpha$. This singularity produces a beguiling distribution that suggests the most probable hydrogen bond geometry is bent instead of linear.

4.1.2 The first solvation shell and tetrahedrality

Ice is a honeycomb network of strong hydrogen bonds, where each molecule donates and accepts two bonds. In the liquid state, tetrahedral order persists [10] on the length scale of one solvation shell, but longer range crystalline order disappears. The vibrational absorption spectrum of the OH stretch is slightly different in water and ice. In hexagonal (I_h) ice, the IR spectrum is broader and shifted to the red with respect to the liquid. This fact led Laenen and Laubereau [24, 23] to hypothesize that the value of ω_{OH} describes the ordering, or degree of tetrahedrality in the first solvation shell. We examined this hypothesis by looking at the joint probability distribution of ω_{OH} with the tetrahedrality order parameter, q, defined as

$$q = 1 - \frac{3}{8}\sum_{j=1}^{3}\sum_{k=j+1}^{4}(\hat{r}_{\mathrm{OO}_j} \cdot \hat{r}_{\mathrm{OO}_k} + \frac{1}{3})^2, \tag{4.2}$$

where the unit vectors point from the oxygen of HOD to those of first solvation shell molecules j and k [10]. If the first solvation shell forms a perfect tetrahedron about HOD, $q = 1$. The average of q vanishes in the dilute gas, which prefers no local order. Typical values in the liquid range from 0.5 to 0.9 [10]. Figure 4-3 shows that there is

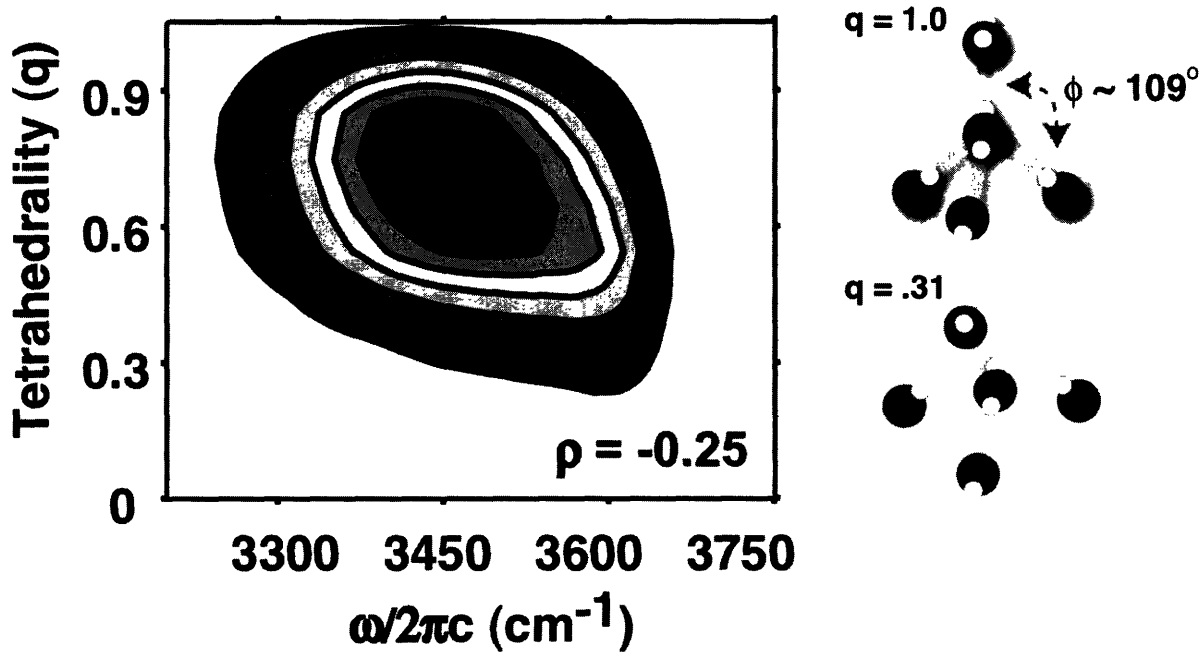

Figure 4-3: Joint probability distribution of tetrahedrality and OH frequency. The poor correlation demonstrates that the OH frequency is not a sensitive probe of local tetrahedral order in water. The illustration on the right shows the numerical value of the order parameter in a perfect tetrahedron and a disjoint, though mostly tetrahedral configuration. Typical values for q in the liquid lie between 0.5 and 0.9 [10].

negligible correlation between the OH frequency and the degree of tetrahedrality in the first solvation shell.

4.1.3 Electric field order parameters

The hydrogen bonding variables, R_{OO} and $\cos(\alpha)$ correlate reasonably well with ω_{OH}. However, as Figure 4-1 suggests, it is possible to devise a function of these variables that exhibits an even stronger correlation with ω_{OH}. To isolate the specific contribution of the hydrogen bonding partner and molecules in the first solvation shell from the rest of the liquid, we defined the electric field order parameters E_0 and E_1 to be the electric field at the proton from the hydrogen bonding partner and molecules in the first solvation shell, respectively, in the $\hat{\boldsymbol{r}}_{OH}$ direction [12]. It is also useful to define the "collective" electric field, E_c, as the field on the proton from all molecules except the hydrogen bonding partner by making the following decomposition,

$$E_c = E - E_0 \,. \tag{4.3}$$

Figure 4-4 shows the joint probability densities for the electric field order parameters. E_0 is more strongly correlated to ω_{OH} than either R_{OO} or $\cos(\alpha)$ ($\rho = 0.89$). Adding molecules in the first solvation shell shifts the position of the maximum of the join probability density, but does not improve the correlation.

Figure 4-1 shows that in the red and middle of the frequency distribution, the hydrogen atoms of the hydrogen bonding partner point away from the HOD molecule. Because the hydrogen densities for the red and middle of the frequency distribution are

so similar, we can conclude that the hydrogen atoms are not important for determining the frequency in these regions of the spectrum. In these regions, the oxygen atom dominates the electric field at the proton and it is easy to express E_0 in terms of ω_{OH} and $\cos(\alpha)$. When working in units where the OH bond has a length of unity (Å for SPC/E), we obtain

$$E_0 \propto \frac{R_{OO}\cos(\alpha) - 1}{(R_{OO}{}^2 + 1 - 2R_{OO}\cos(\alpha))^{\frac{3}{2}}} . \tag{4.4}$$

On the blue side of the line, the hydrogen atoms of the nearest neighbor begin to play a more pronounced role in perturbing ω_{OH}. For these configurations, the approximate system-bath Hamiltonian is a dipole-dipole interaction between the dipole of the hydrogen bonding partner and the Stark dipole (Equation 2.93) of HOD. This interaction introduces extra intermolecular variables, and there is no simple relationship between E_0, R_{OO} and $\cos(\alpha)$. These diverse configurations seen in figure 4-1 distort the probability distributions in Figure 4-4 A and 4-4 B on the blue side.

Another simple electrostatic argument explains the weak dependence of ω_{OH} on tetrahedrality (q). The OH bond is one leg of the hydrogen bonded tetrahedron in the first solvation shell. The remaining three legs of the tetrahedron are nearly orthogonal to the OH bond, with an angle of $\approx 109°$. The dot product in equation 2.92 significantly diminishes their contribution to the frequency shift relative to that from the nearly collinear hydrogen bonding partner. The OH frequency is so sensitive to the hydrogen bonding partner that it is an insensitive probe of the remainder of the molecular structure in the first solvation shell.

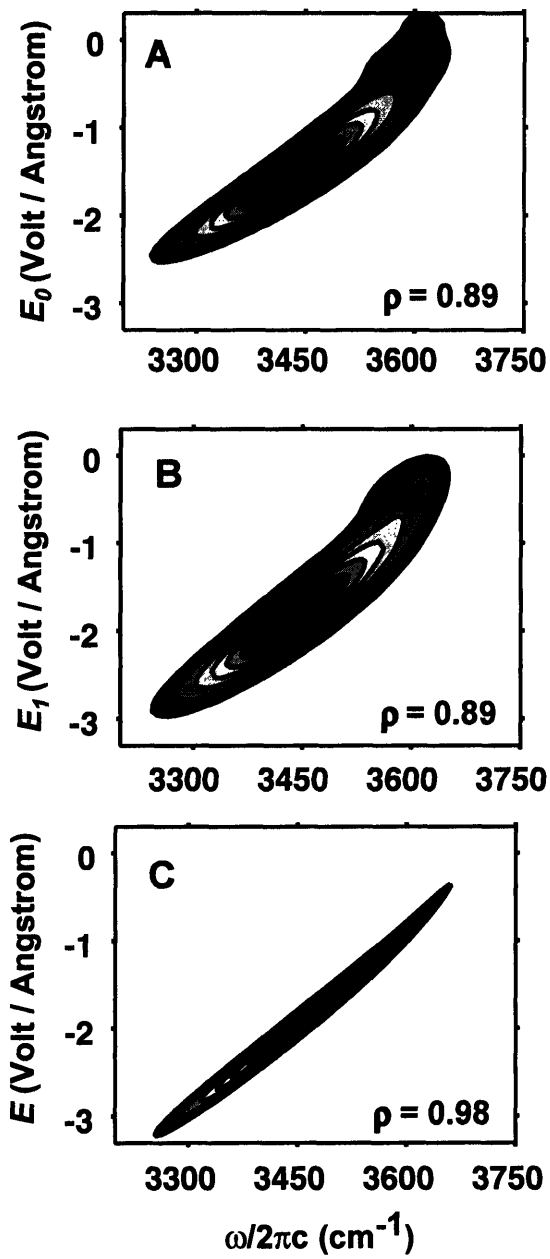

Figure 4-4: Joint probability densities of electric field variables and ω_{OH}. **(A)** The electric field from the nearest neighbor (E_0) is a function of the intermolecular geometries investigated in figure 4-2 but improves the correlation between ω_{OH} and either R_{OO} and $\cos(\alpha)$ alone. **(B)** Including the electric field from all the molecules in the first solvation shell shifts the position of the maximum of the probability density, but it does not improve the correlation. **(C)** By including the electric field from all molecules in the simulation and their periodic images, the correlation coefficient nears unity.

4.2 Dynamics

IR spectroscopy measures response functions, that in perturbative limits can be expressed in terms of equilibrium time correlation functions, such as $C_{\omega\omega}(t)$ [33]. These equilibrium TCFs are the connection between simulation and experiment, and describe the time scales of natural fluctuations at equilibrium. Because intermolecular motions in water are fast ($\approx$ 100 fs), building intuition about vibrational spectroscopy based on joint probability densities alone can be misleading. Figures like 4-1 are instructive to motivate a set of meaningful order parameters, but cannot not be relied on to provide a comprehensive picture of vibrational spectroscopy because they ignore the dynamics of molecular environments.

Understanding the spectroscopy in terms of molecular motions lies in quantifying the relationship between the *dynamics* of the relevant order parameters and the frequency. Joint probability distributions and statistical correlations of the statics identified a set of relevant order parameters, E_0, E_c, E, and $\mathrm{R_{OO}}$.Figure 4-5 is a plot of the normalized TCFs for $\mathrm{R_{OO}}$ and q for times less than 500 fs. As q correlates poorly with frequency, the dynamics of q do not follow the dynamics of ω_{OH}. The correlation function in $\mathrm{R_{OO}}$, the interatomic oxygen distance, displays a more pronounced beat than in $C_{\omega\omega}(t)$.

E correlates strongly with ω_{OH}, and its TCF bears remarkable resemblence to $C_{\omega\omega}(t)$. Figure 4-6 highlights the short time part of the normalized correlation functions for the electric field order parameters. The local field correlations, $\langle \delta E_0(t) \delta E_0(0) \rangle$ display the same beat at $\approx$ 125 fs seen in $C_{\omega\omega}(t)$. The reason is that the local field

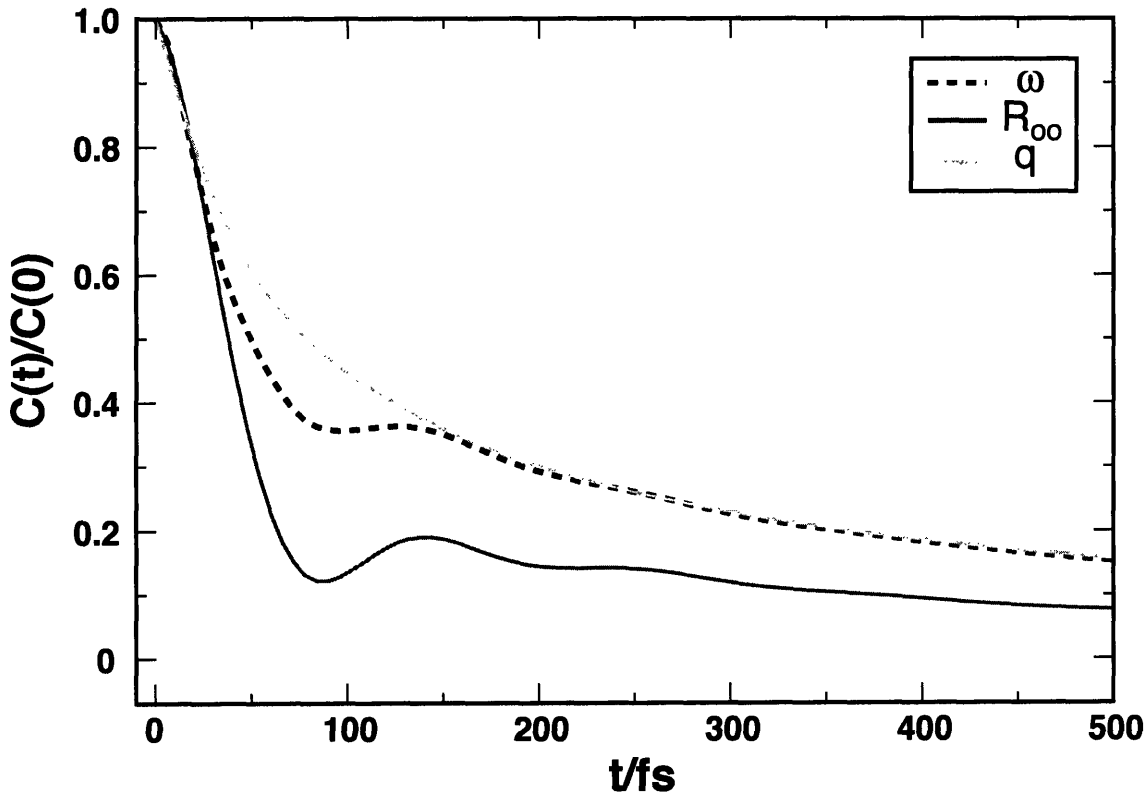

Figure 4-5: Dynamics of molecular order parameters. As one would anticipate from the weak correlation between q and ω_{OH}, the dynamics of q do not follow the dynamics of ω_{OH} at short times. The beat in $C_{\omega\omega}(t)$ is most pronounced in $\mathrm{R_{OO}}$.

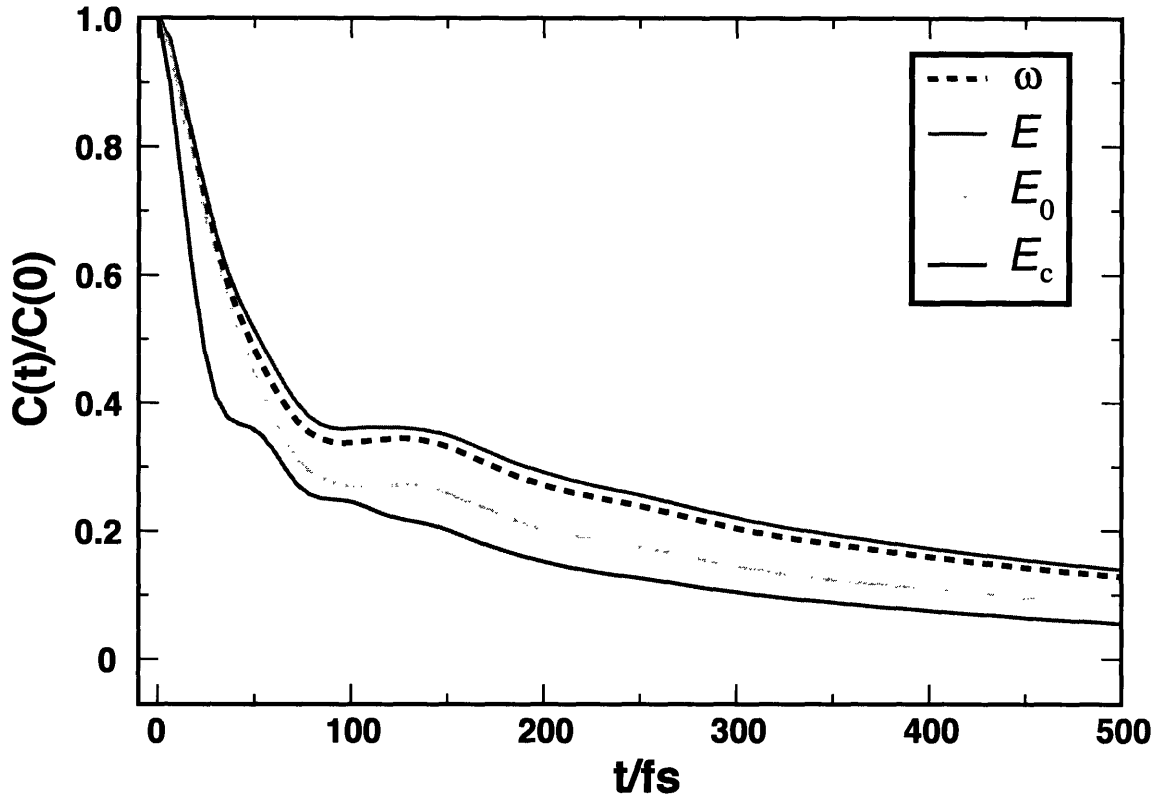

Figure 4-6: Dynamics of order parameters based on the electric field at the proton. Fluctuations along the hydrogen bond control the relaxation before $\approx$ 200 fs. The fluctuations of the local field follow $C_{\omega\omega}(t)$. The collective electric field fluctuations resemble the dielectric response of water. A shoulder appears near $\approx$ 60 fs from molecular librations outside the first solvation shell.

component in the direction of the OH bond is nearly parallel to the displacement of R_{OO}. The local electric field fluctuations between HOD and its hydrogen bonding partner produce the beat in $C_{\omega\omega}(t)$, but their molecular origin is the hydrogen bond vibration between oxygen atoms.

The beat in $C_{\omega\omega}(t)$, $\langle \delta E_0(t) \delta E_0(0) \rangle$ and R_{OO} is also present in the velocity-velocity autocorrelation function of water. Analysis of the velocity-velocity autocorrelation function has revealed that the beat corresponds to density fluctuations in the liquid that behave more like those of a disordered solid than a liquid. The speed of sound at the beat frequency is $\approx$ 3.2 km/s, about twice as fast as the speed of sound of water in the hydrodynamic regime. The fast speed of sound in water corresponds to fluctuation wavelengths of $\approx$ 3-8 Å [36, 4, 5, 47, 40]. This peculiar behavior can be explained by hydrogen bonding [4, 5]. Hydrogen bonds are energetically favorable between the hydrogen and oxygen atoms of the bonding pair, but it is energetically unfavorable between the oxygen atoms. This repulsion of the oxygen atoms gives rise to an underdamped oscillation in the density fluctuations [47, 40, 4, 5].

The collective electric field fluctuations $\langle \delta E_c(t) \delta E_c(0) \rangle$ exhibit a shoulder at $\approx$ 60 fs from librational motions. The shape of this function is remarkably similar to what Lang *et al.*[25, 42] have measured for the solvation correlation function of an electronic chromophore in water. Additionally, Song and Chandler [42] have shown that for simple solute geometries, the solvation polarizability resembles the collective electric field fluctuations displayed in Figure 4-6. This observation further supports the notion that for vibrational spectroscopy of HOD in liquid D_2O, the prominent molecular feature is the hydrogen bonding partner. The remaining electric field fluctuations

follow the dielectric relaxation of a (modified) dielectric.

Figure 4-7 focuses on the the long time decay of the normalized TCFs for ω_{OH} and each of the order parameters. The long time (> 200 fs) exponential decay time is nearly the same ($\approx$ 600 fs) for all of these functions, yet many of the order parameters are qualitatively different. For example, the tetrahedrality, which shows poor statistical correlation with the frequency and exhibits different short time dynamics than frequency fluctuations, decays with the same long time constant as $C_{\omega\omega}(t)$. The similarity in the decay times after $\approx$ 200 fs for such different measures of the molecular environment suggests that this is the regime where collective fluctuations dominate. After $\approx$ 200 fs, cooperative intermolecular arrangements, density and polarization fluctuations destroy correlations for the order parameters after $\approx$ 200 fs.

Analyzing the interplay between local and collective electric fields sheds light on the types of molecular and cooperative motions that dephase the OH vibration. Specifically, Figure 4-8 compares the Fourier transform of the correlation function $\widetilde{C}(\omega) = \int_{-\infty}^{\infty} dt\ C(t)exp(i\omega t)$, or spectral density, for $\langle \delta E_0(t)\delta E_0(0)\rangle$, to that of the cross correlation function between the local and collective electric fields, $C_{\mathrm{cross}}(t) = \langle \delta E_c(t)\delta E_0(0)\rangle$. The integral over spectral density of the cross correlation function is negative.

$$\int_0^{\infty} d\omega\ \widetilde{C}_{\mathrm{cross}}(\omega) = \pi\, C_{\mathrm{cross}}(t=0), \tag{4.5}$$

$$\rho_{E_cE_0} = \frac{C_{\mathrm{cross}}(t=0)}{\sigma_{E_c}\sigma_{E_0}}. \tag{4.6}$$

$\rho_{E_cE_0}$ is the correlation coefficient between the local and collective electric fields.

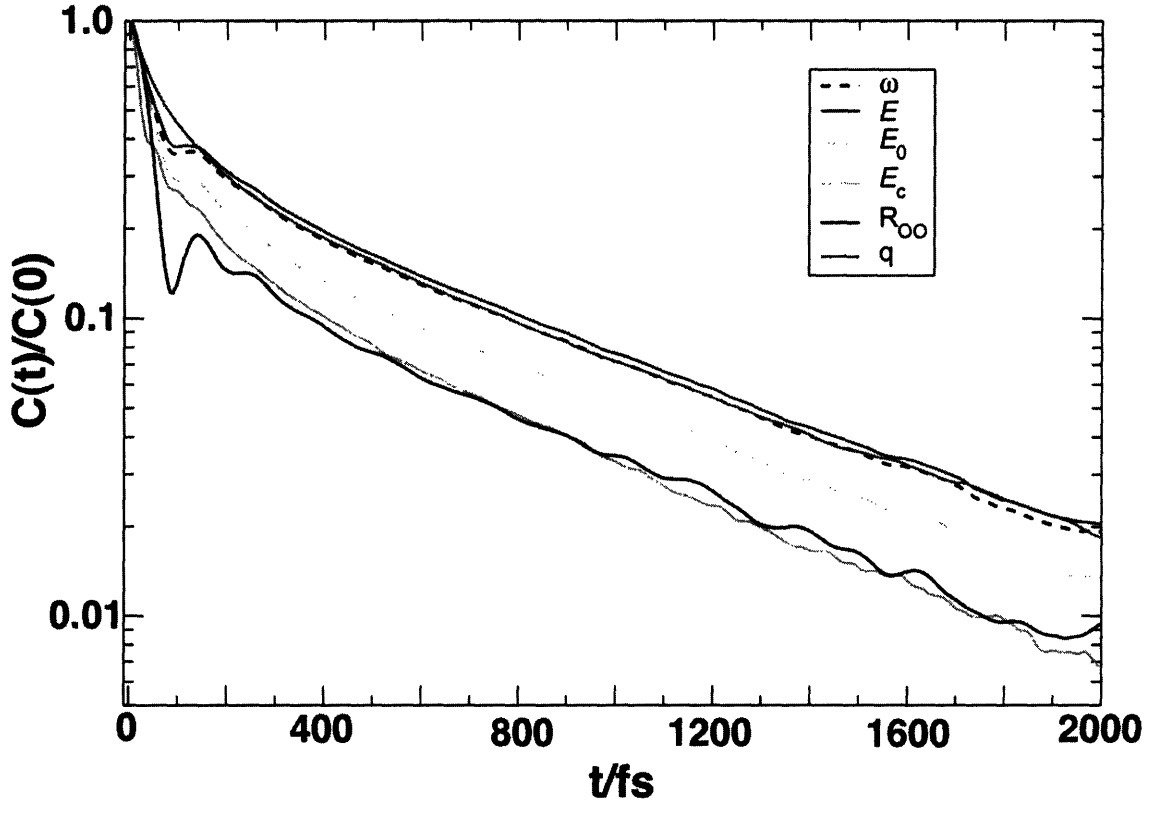

Figure 4-7: Semilog plot of the normalized time correlation functions for the order parameters studied in the text. The time constant of the exponential decay after $\approx$ 200 fs for qualitatively different order parameters is $\approx$ 600 fs. The long time decay of $C_{\omega\omega}(t)$ characterizes electric field fluctuations on longer length scales than the distance between molecules in the first solvation shell.

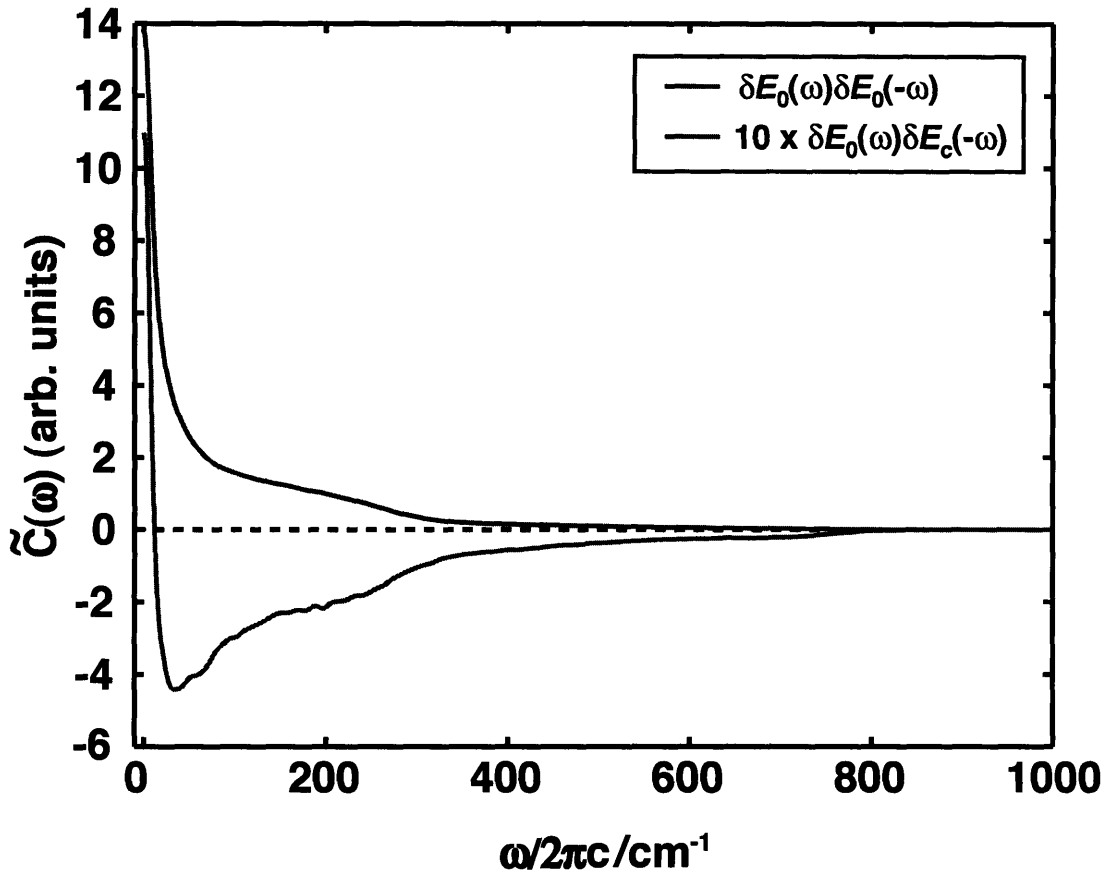

Figure 4-8: The Fourier transform of the cross correlation function (red line) between the local and collective electric field fluctuations reveals the phase relationship between these variables as a function of frequency. When HOD and its proximal hydrogen bonding partner approach each other and the local field strength increases, the medium polarizes in the opposite direction to minimize the electrostatic energy. The low frequency peak, however, is in phase with the local electric field fluctuations. Because this part of the spectral density corresponds to the exponential decay of the electric field fluctuations, the change in sign from negative to positive indicates that the long time exponential decay of correlations in Figure 4-7 is cooperative. The dotted black line is the baseline, included for contrast.

The integral in Equation 4.5 is an example that illustrates how averaging over a dynamical quantity ($\widetilde{C}_{\text{cross}}(\omega)$) returns a static one ($\rho_{E_c E_0}$). Because $\rho_{E_c E_0}$ is negative, the local and collective electric fields are anti-correlated, but Figure 4-8 shows that only part of the spectral density is negative. The frequency dependence in Figure 4-8 reveals that the collective field opposes changes that increase the field strength between HOD and its hydrogen bonding partner when the frequency is larger than a few wavenumbers. The high frequency molecular motions, librations and hydrogen bond vibrations, polarize against high frequency changes in the local electric field. Alternatively, the local electric field is shielded from the more cooperative polarization fluctuations on short time scales. The zero frequency peak in $\widetilde{C}_{\text{cross}}(\omega)$ is positive. It corresponds to the long time exponential decay of $C_{\text{cross}}(t)$, indicating that the motions that decorrelate E_c and E_0 at long times are in phase with each other. After $\approx$ 200 fs, the TCFs $\langle \delta E_0(t) \delta E_0(0) \rangle$ and $\langle \delta E_c(t) \delta E_c(0) \rangle$ decay exponentially and the local and collective fields fluctuate in concert with one another. These data appear to support a dispersion relationship, where shielding between the local and collective fields is important for frequencies greater than $\approx (200 \text{ fs})^{-1}$, while lower frequencies correspond to collective polarization fluctuations with wavelengths longer than the intermolecular spacing of the first solvation shell ($\approx$ 3 Å). The longer wavelength fluctuations drive vibrational dephasing in the long time regime ($t >$ 200 fs) and participate in de-correlating the order parameters on the time scale of $\approx$ 600 fs.

4.3 Discussion and conclusions

We employed a simple adiabatic strategy combined with time independent perturbation theory to compute vibrational frequencies of HOD in liquid D_2O with atomistic MD simulations. The strategy is accurate, computationally efficient and lends itself to a straightforward physical interpretation. The predictions of our model compare well with recent experimental data [13]. Joint probability distributions reveal statistical relationships between a set of physically motivated order parameters that classify the liquid environment and ω_{OH}. The correlation between ω_{OH} and the variables that describe local molecular geometries in the vicinity of the HOD molecule (q,$\cos(\alpha)$, R_{OO}) are manifestations of the stronger underlying correlation between ω_{OH} and the electric field at the proton. The strong correlation between ω_{OH} and the electric field explains the weak connection between frequency and the tetrahedrality of the first solvation shell, as well as the nearly azimuthal symmetry that Figure 4-1 displays about the OH axis on the red side of the line. As Fig. 4-6 shows, adding the electric field contributions from molecules in the first solvation shell does little to improve upon the correlation between ω_{OH} and E_0 alone. These observations argue for a separation of length scales between between the proximal hydrogen bonding partner and the rest of the molecules in the liquid.

Classical electrostatic forces dominate (over, for example, dispersion forces) in determining the optical spectroscopy of polar liquids. Solvation dynamics experiments, for example, view the collective response of solvent in response to rapid changes in the charge distribution of a chromophore. Treating the solute's environment as a linearly

responding polarizable medium often yields accurate predictions for the dynamics of solvation energy measured in experiments or computed in simulations [42, 41].

There is mounting evidence that vibrational dynamics in polar solvents are similarly governed by electrostatics. Rey and Hynes [37] found that the electrostatic forces dominated non-Coloumbic forces in their study of vibrational dynamics of the CN^- anion in water. Kwac and Cho [22] have computed vibrational frequencies for small peptides by solving the Schrödinger equation for the vibrational coordinate under the influence of the electrostatic potential from the peptide and solvent molecules. The physical picture we proposed in Ref. [12] and have described in detail in this paper is much simpler still: to a very good approximation instantaneous vibrational frequency shifts are directly proportional to the liquid's electric field at a single point in space ($\boldsymbol{r}_{\mathrm{H}}$) projected onto a single direction ($\boldsymbol{r}_{\mathrm{OH}}$). This connection is a powerful concept for interpreting and calculating spectral diffusion. Corcelli and Skinner[9], for example, have recently exploited the strong correlation between vibrational frequency and electric field at the proton to devise a hybrid QM/MM method for computing vibrational frequencies.

Previous experimental [21, 49, 7, 24] and simulation [28, 38, 32] work has been driven by the empirical relationships built by Novak [35], Badger[2], and Rundle[34] but the spectroscopy of the OH stretch of HOD in liquid D_2O is much richer than previously imagined. IR spectroscopy measures transient electric field fluctuations. At times prior to $\approx$ 200 fs, these dynamics characterize fluctuations on short length scales, where the density fluctuations are short ranged. Any information obtained from IR spectroscopies about local hydrogen bond interactions between HOD and its

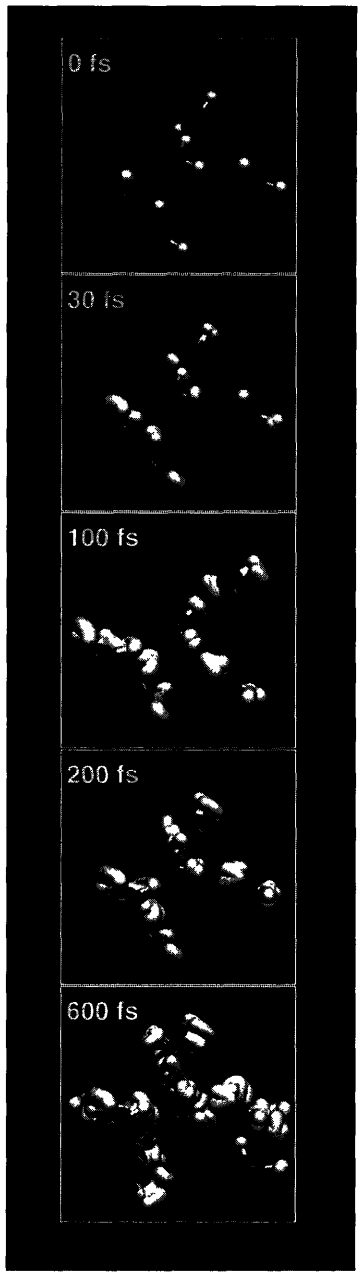

Figure 4-9: Evolution of time and length scales in water. Initially, the HOD molecule (center molecule) is hydrogen bonded to three partners. Between 30 and 100 fs, the molecular motions are small, localized fluctuations in the hydrogen bond network. After 200fs, corresponding roughly to the correlation time of $C_{\omega\omega}(t)$, collective fluctuations destroy the structure of the first solvation shell. After 600 fs have passed, the molecules in the first solvation shell have little memory of their original positions, and new molecular partners attempt entrance to the first solvation shell.

hydrogen bonding partner is unreliable after 200 fs because after this time the relaxation becomes collective. Figure 4-9 is a chronological "time-elapsed photograph" of how time and length scales evolve in water over several hundreds of femtoseconds, and illustrates the drastic changes in the liquid environment between 0 and 600 fs.

At longer times ($>$ 200 fs), there is a cross over to exponential relaxation that includes both molecular participants and collective density and polarization fluctuations. As Figure 4-8 shows, collective polarization fluctuations shield fast ($\approx$ 200 fs) distortions of the local electric field. The characteristic shielding motions are the libration and hydrogen bond stretch of the D_2O molecules and are out of phase with the local electric field fluctuations. The long time decay, seen as a zero frequency resonance in the cross correlation spectrum, is in phase with the local electric field fluctuations. At long times the relaxation originates from large scale cooperative reorganization, not specific molecular motions such as hydrogen bond making and breaking as some have suggested [28, 49, 7, 50]. Previous pump-probe experiments have operated with time resolution that is longer than the characteristic time of 200 fs [21, 49, 7, 24], and hence probe the time scale of collective polarization fluctuations. Only recently have experimentalists performed measurements with sufficiently short time resolution to observe dynamics that occur on molecular length scales [50, 1, 30, 12, 13].

Our picture of vibrational dephasing in water resonates with Marcus' theory of solvation dynamics, where by analogy the hydrogen bonding partner is an "inner shell" participant whose dynamics are buffeted by a polarizing solvent [45]. Our observations suggest that one may be able to understand the physical origin and

qualitative features in vibrational dephasing experiments on hydrogen bonded systems with a highly simplified model. For HOD in liquid D_2O, the model would consist of only the hydrogen bonding partner as an essential molecular feature and represent all other molecules as an appropriate polarizable dielectric. This picture may prove useful when one is interested in the spectroscopy of complex systems where a mechanistic description of vibrational dynamics is important and enigmatic, but fully atomistic simulations are computationally costly. Such systems include large proteins that contain side chains and backbone atoms hydrogen bonded to the aqueous solution, as well as vibrational dynamics in mesoscopic but confined environments.

Bibliography

[1] John B. Asbury, Tobias Steinel, C. Stromberg, S. A. Corcelli, C. P. Lawrence, J. L. Skinner, and M. D. Fayer. Water dynamics: Vibrational echo correlation spectroscopy and comparison to molecular dynamics simulations. *Journal of Physical Chemistry A*, 108:1107–1119, 2004.

[2] Richard M. Badger. The relation between the energy of a hydrogen bond and the frequencies of the $O-H$ bands. *Journal of Chemical Physics*, 8:288–9, 1940.

[3] U. Balucani, J.P. Brodholt, and R. Vallauri. Analysis of the velocity autocorrelation function of water. *J. Phys. : Condens. Matter*, 8:6139–6144, 1996.

[4] U. Balucani, Ruocco G., A. Torcini, and R. Vallauri. Fast sound in liquid water. *Physical Review E*, 47(3):1677–1684, 1993.

[5] U. Balucani, G. Ruocco, M. Sampoli, A. Torcini, and R. Vallauri. Evolution from ordinary to fast sound in water at room temperature. *Chemical Physics Letters*, 209(4):408–416, 1993.

[6] P. Bosi, F. Dupre, F. Menzinger, F. Sacchetti, and M. C. Spinelli. Neutron scattering of water. *Nuovo Cimento Lett.*, 21:436, 1978.

[7] S. Bratos, G. M. Gale, G. Gallot, F. Hache, N. Lascoux, and J. Cl. Leicknam. Motion of hydrogen bonds in diluted HDO/D_2O solutions: Direct probing with 150 fs resolution. *Phys. Rev. E*, 61(5):5211–5217, 2000.

[8] M. Cho, G. R. Fleming, S. Saito, I. Ohmine, and R. M. Stratt. Instantaneous normal mode analysis of liquid water. *J. Chem. Phys.*, 100:6672–6683, 1994.

[9] S. A. Corcelli, C. P. Lawrence, and J. L. Skinner. Combined electronic structure/molecular dynamics approach for ultrafast infrared spectroscopy of dilute HOD in liquid H_2O and D_2O. *Journal of Chemical Physics*, 120:8107–8117, 2004.

[10] Jeffrey R. Errington and Pablo G. Debenedetti. Relationship between structural order and the anomalies of liquid water. *Nature*, 409:318–321, 2001.

[11] C. J. Fecko, J. D. Eaves, and A. Tokmakoff. Isotropic and anisotropic raman scattering from molecular liquids measured by spatially masked optical kerr effect spectroscopy. *J. Chem. Phys.*, 117(3):1139–1154, 2002.

[12] C.J. Fecko, J.D. Eaves, J.J. Loparo, A. Tokmakoff, and P.L. Geissler. Local and collective hydrogen bond dynamics in the ultrafast vibrational spectroscopy of liquid water. *Science*, 301:1698–1702, 2003.

[13] C.J. Fecko, J.L. Loparo, S. R. Roberts, and A Tokmakoff. In press. *Journal of Chemical Physics*, 2004.

[14] G.R. Fleming and M. Cho. Chromophore-solvent dynamics. *Annu. Rev. Phys. Chem.*, 47:109–34, 1996.

[15] G. M. Gale, G. Gallot, F. Hache, N. Lascoux, S. Bratos, and J-Cl. Leicknam. Femtosecond dynamics of hydrogen bonds in liquid water: A real time study. *Phys. Rev. Lett.*, page 1068, 1999.

[16] T. Gaskell and S. Miller. Longitudinal modes, transverse modes, and velocity correlations in liquids I. *Journal of Physics C - Solid State Physics*, 11(18):3749–3761, 1978.

[17] T. Gaskell and S. Miller. Longitudinal modes, transverse modes, and velocity correlations in liquids II. *Journal of Physics C - Solid State Physics*, 11(24):4839–4848, 1978.

[18] H. Graener, G. Seifert, and A. Laubereau. New spectroscopy of water using tunable picosecond pulses in the infrared. *Phys. Rev. Lett.*, 66:2092–2095, 1991.

[19] J.B. Hasted, S.K. Husain, F. A. M. Frescura, and J. R. Birch. IR water. *Chem. Phys. Lett.*, 118:622, 1985.

[20] R. Jankowiak, J.M. Hayes, and G.J. Small. Spectral hole-burning spectroscopy in amorphous molecular solids and proteins. *Chemical Reviews*, 93(4):1471–1502, 1993.

[21] Michel F. Kropman, Han-KWang Nienhuys, Sander Woutersen, and Huib J. Bakker. Vibrational relaxation and hydrogen-bond dynamics of HDO:H_2O. *J. Phys. Chem. A*, 105:4622–4626, 2001.

[22] K. Kwac and M. Cho. Molecular dynamics simulation study of n-methylacetamide in water I: Amide I mode frequency fluctuation. *J. Chem. Phys.*, 119(4):2247–2255, 2003.

[23] R. Laenen, C. Rauscher, and A. Laubereau. Dynamics of local substructures in water observed by ultrafast IR holeburning. *Phys. Rev. Lett.*, 80:2622–2625, 1998.

[24] R. Laenen, C. Rauscher, and A. Laubereau. Local substructures of water studied by transient hole-burning spectroscopy in the infrared: Dynamics and temperature dependence. *J. Phys. Chem. B*, 102:9304–9311, 1998.

[25] M. J. Lang, X. J. Jordanides, X. Song, and G. R. Fleming. Aqueous solvation studied by photon echo spectroscopy. *J. Chem. Phys.*, 110:5884–5892, 1999.

[26] C. P. Lawrence and J. L. Skinner. Vibrational spectroscopy of HOD in liquid D_2O. I. vibrational energy relaxation. *Journal of Chemical Physics*, 117:5827–5838, 2002.

[27] C. P. Lawrence and J. L. Skinner. Vibrational spectroscopy of HOD in liquid D_2O. II. infrared line shapes and vibrational stokes shift. *Journal of Chemical Physics*, 117:8847–8854, 2002.

[28] C. P. Lawrence and J. L. Skinner. Ultrafast infrared spectroscopy probes hydrogen-bonding dynamics in liquid water. *Chemical Physics Letters*, 369:472–477, 2003.

[29] C. P. Lawrence and J. L. Skinner. Vibrational spectroscopy of HOD in liquid D_2O III: Spectral diffusion, and hydrogen-bonding and rotational dynamics. *Journal of Chemical Physics*, 118:264–272, 2003.

[30] J. J. Loparo, C. J. Fecko, J. D. Eaves, S. T. Roberts, and A. Tokmakoff. Reorientational and configurational fluctuations in water observed on molecular length scales. *Physical Review B*, 2004.

[31] Alenka Luzar and David Chandler. Hydrogen-bond kinetics in liquid water. *Nature (London)*, 379:55–7, 1996.

[32] Klaus B. Moller, Rossend Rey, and James T. Hynes. Hydrogen bond dynamics in water and ultrafast infrared spectroscopy: A theoretical study. *Journal of Physical Chemistry A*, 108:1275–1289, 2004.

[33] Shaul Mukamel. *Principles of Nonlinear Optical Spectroscopy.* Oxford University Press, 1998.

[34] Kazuo Nakamoto, Marvin Margoshes, and R.E. Rundle. Stretching frequencies as a function of distances in hydrogen bonds. *Journal of the Americal Chemical Society*, 77:4670–4677, 1955.

[35] A. Novak. Hydrogen bonding in solids. correlation of spectroscopic and crystallographic data. In J. D Dunitz, P. Hemmerich, R. H. Holm, J. A. Ibers, C. K.

Jorgenson, J. B. Neilands, D. Reinen, and R. J. P. Williams, editors, *Structure and Bonding*, volume 18, pages 177–216. Springer-Verlag, New York, 1974.

[36] A. Rahman and F. H. Stillinger. Hydrogen-bond patterns in liquid water. *Journal of the American Chemical Society*, 95:7943–8, 1973.

[37] R. Rey and J. T. Hynes. Vibrational phase and energy relaxation of cn- in water. *J. Chem. Phys.*, 108:142, 1998.

[38] Rossend Rey, Klaus B. Moller, and James T.. Hynes. Hydrogen bond dynamics in water and ultrafast infrared spectroscopy. *Journal of Physical Chemistry A*, 106:11993–11996, 2002.

[39] Rossend Rey, Klaus B. Moller, and James T.. Hynes. Ultrafast vibrational population dynamics of water and related systems: A theoretical perspective. *Chemical Reviews (Washington, DC, United States)*, 104:1915–1928, 2004.

[40] F. Sette, G. Ruocco, M. Krisch, U. Bergmann, C. Masciovecchio, V. Mazzacurati, G. Signorelli, and R. Verbeni. Collective dynamics in water by high-energy resolution inelastic x-ray scattering. *Physical Review Letters*, 75(5):850–853, 1995.

[41] X. Song, D. Chandler, and R.A. Marcus. Gaussian field model of dielectric solvation dynamics. *J. Phys. Chem.*, 100:11954–11959, 1996.

[42] Xueyu Song and David. Chandler. Dielectric solvation dynamics of molecules of arbitrary shape and charge distribution. *Journal of Chemical Physics*, 108:2594–2600, 1998.

[43] F.H. Stillinger. Theory and molecular models for water. *Adv. Chem. Phys.*, 31:1–101, 1975.

[44] Frank H. Stillinger. Water revisited. *Science*, 209(4455):451–457, 1980.

[45] H. Sumi and R.A. Marcus. e- trans; theory. *J. Chem. Phys*, 84(9):4894, 1986.

[46] J. Teixeira, M.-C. Bellissent-Funel, and S. H. Chen. water neutron scattering. *J. Phys. Condens. Mateer*, 2:105, 1990.

[47] J. Teixeira, M.-C. Bellissent-Funel, S. H. Chen, and B. Dorner. Observation of new short-wavelength collective excitations in heavy water by coherent inelastic neutron scattering. *Phys. Rev. Lett.*, 54(25):2681–2683, 1985.

[48] S. Volker. Hole-burning spectroscopy. *Annual Review of Physical Chemistry*, 40:499–530, 1989.

[49] S. Woutersen and H. J. Bakker. Hydrogen bond in liquid water as a brownian oscillator. *Phys. Rev. Lett.*, 83:2077–2081, 1999.

[50] Sergey Yeremenko, Maxim S. Pshenichnikov, and Douwe A. Wiersma. Hydrogen-bond dynamics in water explored by heterodyne-detected photon echo. *Chem. Phys. Lett.*, 369:107–113, 2003.

Chapter 5

Polarizable water models in the vibrational spectroscopy of water

Molecular dynamics simulations of empirical models have guided our understanding of how water molecules play their essential roles in chemistry, biology and physics. Using classical molecular dynamics (MD) simulations, Rahman and Stillinger [15, 14] made remarkably accurate predictions of bulk thermodynamic, atomic pair correlation functions, and transport properties. Stillinger [24] described the peculiar chemical and physical properties of water in terms of the microscopic dynamics of the hydrogen bond network and provided a consistent molecular level description of hydrogen bonding in water. Indeed, it is unlikely that researchers today would have such robust and refined methods without the notable early successes of MD simulations in water.

The potential energy models inspired by these early studies contain few characteristically molecular features. Most empirical water potentials replace electron densities with point charges situated either at atomic or "virtual" sites near the molecule,

rigid intramolecular bonds take the place of intramolecular vibrations, and a simple Lennard–Jones potential represents the excluded molecular volume [1]. Most experimental data that validate such water potentials are either thermodynamic (surface tension, specific heats), transport (diffusion and dielectric constants), or structural quantitites (radial distribution functions). Such quantities are spatial and time averages over a large number of molecules and are not clean measures of the microscopic details of a water potential.

Computer simulations use atomistic models to examine molecular chemistry in detail, and are often a surrogate when experiments are unavailable. Molecular dynamics (MD) studies are seldom concerned with macroscopic behaviors, but instead focus on microscopic motions that facilitate electron and proton transfer, fold proteins, or participate in biological catalysis between an enzyme and its substrate. The potentials employed are typically parameterized so that they reproduce macroscopic bulk thermodynamic quantities and transport coefficients. For such macroscopic quantities, molecular polarizability appears to play a marginal role, but on molecular length scales (Å), the microscopic details of a molecular potential should be important.

Electrons in real molecular systems are not stationary. Molecular electric field strengths are high ($\approx 1\frac{\mathrm{V}}{\mathrm{A}}$), so even a modest degree of polarizability in the molecule will generate charge displacements. The simplest measure of the susceptibility for the electronic coordinates in water comes from the variation of the molecular dipole moment. *Ab-initio* MD simulations of liquid water predict that the molecular dipole moment varies considerably in the liquid [20], which raises questions about the accu-

[1]Examples of such potentials are SPC, SPC/E, ST2, TIP3P and TIP4P

racy of fixed charge models on molecular length scales.

The characteristic time scales of intermolecular dynamics in water are faster than those of almost any other liquid. The fastest motion, the librations or hindered rotations, have a periodicity of $\approx$ 60 femtoseconds (fs) [23]. Femtosecond Raman [6] and electronic solvation dynamics experiments [9] that do have sufficient bandwidth to observe these fast motions in water usually probe collective motions of the liquid or view molecular dynamics through a non-native probe molecule. Inelastic neutron and x-ray scattering trade high spatial resolution for poor temporal resolution.

The hydride stretch frequency is sensitive to the local hydrogen bonding environment [13, 7] and to polarization fluctuations. By isotopically labeling a small number of water molecules, femtosecond IR spectroscopy on the OH stretch of HOD in liquid D_2O views water's structural evolution on fast time scales with an ostensibly native and vibrationally distinct probe. MD studies on the vibrational spectroscopy of water have identified computationally efficient, robust and accurate methods for computing the frequency of the OH stretch of HOD in D_2O based on an adiabatic separation between the fast vibrational motion and the translations and rotations of the D_2O molecules [5, 7, 10, 17, 12]. Our simulations have revealed that the frequency of the OH stretch measures the electric field strength at the proton, in the direction of the OH bond [7, 5]. On short time scales ($<$ 200 fs), spectroscopy of the OH stretch measures distance fluctuations between the HOD molecule and its hydrogen bonding partner (bonded to the H). On time scales longer than 200 fs, the OH stretch probes the polarization fluctuations on length scales larger than a molecular diameter. Two dynamical equilibrium time correlation functions (TCFs) provide the connection be-

tween experiments and computer simulation. The equilibrium frequency-frequency correlation function, $C_{\omega\omega}(t)$ characterizes the equilibrium fluctuations of the vibrational energy [9]

$$C_{\omega\omega}(t) = \langle \delta\omega_{\mathrm{OH}}(t)\delta\omega_{\mathrm{OH}}(0)\rangle. \tag{5.1}$$

Here, $\langle ... \rangle$ is an equilibrium ensemble average, $2\pi\omega_{\mathrm{OH}}$ is the transition frequency for the $|1\rangle \leftarrow |0\rangle$ transition of the OH stretch, and $\delta\omega_{\mathrm{OH}} = \omega_{\mathrm{OH}}(t) - \langle\omega_{\mathrm{OH}}\rangle$. Within several reasonable approximations, one can retrieve this correlation function from a three pulse photon echo peak shift (3PEPS) measurement [9] . The second TCF is the second Legendre polynomial of the projection of the transition dipole moment,

$$C_{\mathrm{or}}(t) = \langle P_2(\boldsymbol{e}(t)\cdot\boldsymbol{e}(0))\rangle, \tag{5.2}$$

where $\boldsymbol{e}(t)$ is unit vector of the transition dipole moment at time t. One obtains $C_{\mathrm{or}}(t)$ by measuring the anisotropy in polarization-selective femtosecond pump-probe spectroscopy [11]. Although simple point charge type models show qualitatively similar features in $C_{\omega\omega}(t)$ and $C_{\mathrm{or}}(t)$ the experiments measure, the results from simulation are not quantitatively accurate. For example, SPC/E [4] underestimates the variance of the frequency distribution and time constant for the long time decay in C(t).

Pair distribution functions, thermodynamic and transport quantities in polarizable and nonpolarizable models are similar. Such quantities are measures of how large ensembles of molecules behave, and are not particularly sensitive to microscopic dynamics. Vibrational spectroscopy on the other hand, measures response

functions. In perturbative limits, response functions can be expressed in terms of TCFs. Fecko *et al.*[7] have recently performed nonlinear vibrational spectroscopies with sufficiently fast time resolution to measure water's fastest intermolecular motions. Because ω_{OH} is sensitive to the electric field strengths, these measurements provide a rigorous point of comparison for predictions from polarizable models on microscopic length scales where the effects of molecular polarizability should be most pronounced. For example, Xu and co-workers [25] showed that the largest discrepencies between polarizable and fixed charge models appear in time correlation functions. Xu *et al.*[25] showed that including molecular polarizability in empirical models of water introduces a slight prejudice on the local environment when hydrogen bonds change partners and also strengthens hydrogen bonds between molecules, lengthening the time pairs of molecules spend hydrogen bonded to one another. The picture of hydrogen bonding becomes qualitatively different when one allows the molecules to polarize.

We examined the role of molecular polarizability in vibrational spectroscopy with computer simulations of fluctuating charge (fq) models for water. In Section 5.1, we describe the protocol developed to compute vibrational spectrosopies in the fq and fixed charge models. In Section 5.2, we compare recent experimental results for $C_{\omega\omega}(t)$, $C_{\mathrm{or}}(t)$, and IR absorption spectrum to simulations two qualitatively different fixed charge and fq water models.

5.1 Methods

In classical molecular dynamics, one imagines that the motions of the electrons are fast relative to the nuclear degrees of freedom and that the density of molecules is sufficiently low that neighboring molecules do not begin to share electron densities. The electronic and vibrational energies are high with respect to k_BT, so one can "average" them out, replacing high energy vibrations with stiff bonds and fast electron densities with appropriate point charges or dipoles. In these limits, classical mechanics provides a reasonable description for the translations and rotations of molecules, offering a computationally feasible method for studying the dynamics of complex systems in the condensed phase.

In real molecular systems, particularly those with large or polarizable atoms, the electronic degrees of freedom are not stationary on atomic sites. In fact, the molecular dipole moment of water varies considerably in the liquid [20], with a full width at half maximum (FWHM) of $\approx$ 1 Debye. Fixed charge models average these fluctuations away and replace them with an appropriate "mean field" value, evidently unable to model energetic or dynamic effects of distorted or fluctuating electron densities. To address this issue, Rick *et al.*[18] have developed fq models and methods for molecular dynamics. This approach allows the electronic degrees of freedom to deform during the course of the simulation but introduces only a modest additional computational burden in most cases [18], providing an attractive alternative to *ab-initio* molecular dynamics when molecular polarizability is important.

In the fq models, one specifies the molecular parameter set by defining the linear

response matrix, $\boldsymbol{J}$ that describes how the charges and dipoles on the molecule, $\boldsymbol{q}$, respond to an external field, $\boldsymbol{v}$ [21].

$$\boldsymbol{q} = -\boldsymbol{J}^{-1}\boldsymbol{v}. \tag{5.3}$$

In principle, one can solve the linear Equation 5.3 at each step in the simulation. In practice, it is more efficient to employ the extended Lagrangian method to solve for the electronic degrees of freedom [21].

Simulation Details

We have performed MD simulations of the SPC/E [4], SPCfq [18], TIP5P [19], and TIP5Pfq [22] models for liquid water. The simple point charge model of water (SPC/E) is an empirical potential energy where each atom has a fixed point charge. The OH bonds are 1 Åin length and the angle between the OH bonds is 109.47 °. The SPCfq model uses the same molecular geometry as SPC/E but allows the charges at the atomic sites to vary in response to the fluctuations in the electric field surrounding the molecule. The TIP5P model is a five-site potential for liquid water. The geometry of the molecule is set to the experimentally determined geometry, where the OH bond lengths are 0.9572 Åand angle between OH bonds is 104.52°. Each hydrogen atom carries a positive charge but the compensating negative charges are not on the oxygen atom but rather at positions to mimic the lone pairs of oxygen. The original TIP5P model was designed for simulations that do not include long range electrostatics (i.e. Ewald sums). We have simulated the Rick's [19] re-parameterized version

of TIP5P that has been designed for Ewald sums. The polarizable counterpart to TIP5P, TIP5Pfq has been parameterized from *ab-initio* calculations and comes in two flavors, POL5-TZ and POL5-QZ [22]. We have simulated the POL5-TZ model, or POL5 model for short. In the POL5 model there is an additional polarizable dipole on the oxygen atom that points out of the plane of the molecule.

The thermodynamic state point of liquid D_2O at ambient conditions corresponds to a density of 1.104 $\frac{g}{cm^3}$. We ran 17 independent realizations of one HOD molecule dissolved 107 D_2O molecule for a duration of 500 ps. During the initial equilibration period (10 ps), Nose-Hoover chain thermostats [1] kept each realization of the simulation at constant temperature (298.15 K). After equilibration, we rescalled the velocities at 10 ps intervals to ensure that the rescaling interval was an order of magnitude longer than the dynamics of interest. The fluctuations in the total energy were $O(10^{-4})$ of the total energy.

In the fq models, the electrostatic potential energy is a function of the values of $\boldsymbol{q}$. For the fq potentials, we solved Equation 5.3 at the beginning of the simulation and used the extended Lagrangian method [18] to ensure that the electronic coordinates remained on the minimum of the electrostatic potential throughout the duration of the simulation. We assigned the electronic degrees of freedom fictitious masses, and treated them as dynamical variables that propagate with the imposed constraint of electroneutrality. The electronic mass was sufficiently small to decouple the intramolecular electronic and nuclear degrees of freedom, but large enough to average over transient fluctuations of the electronic coordinates that have negligible effect on the nuclear dynamics [21]. To compute the long-ranged electrostatics, we

used the particle-particle particle-mesh approximation to the Ewald sum, P3PME, to include dipolar terms [26].

5.1.1 Calculating vibrational frequencies

In Chapter 2, we have described a computationally efficient strategy for calculating the vibrational frequency of an HOD molecule in liquid D_2O [7, 5]. We follow a similar approach in this Chapter, but we need to adapt the adiabatic strategy because the electronic degrees of freedom are faster than the vibration. As before, we partition the total Hamiltonian, H as the sum of the system (HOD oscillator) bath (translations and rotations of all molecules), and system-bath coupling.

$$H = H_{\rm s}(P,Q) + H_{\rm sb}(Q,\boldsymbol{q},\boldsymbol{r}^N) + H_{\rm b}(\boldsymbol{p}^N,\boldsymbol{r}^N,\boldsymbol{q}). \tag{5.4}$$

$H_{\rm s}$ (P,Q) is the Hamiltonian of the OH stretch for HOD in the gas phase, which we take from a spectroscopic gas phase Hamiltonian [16]; P and Q are the momentum and position operators of the OH oscillator; $H_{\rm b}(\boldsymbol{p}^N,\boldsymbol{r}^N)$ is the bath Hamiltonian, that describes all of the translations and rotations of the molecules, and $\boldsymbol{r}$ are the atomic cartesian coordinates and $\boldsymbol{p}$ their momenta; $H_{\rm sb}(Q,\boldsymbol{r}^N)$ is the system-bath Hamiltonian that couples the OH oscillator with the classical degrees of freedom. The potential energy V in $H_{\rm b}$ is an empirical water potential, TIP5P, POL5, SPC/E, or SPCfq. The vibrational eigenstates and energies are solutions to the adiabatic

Schrödinger Equation,

$$(H_s(P,Q) + H_{sb}(Q, \boldsymbol{q}; \{\boldsymbol{r}\}))|\Psi(\boldsymbol{r}(t))\rangle = \mathcal{E}(\boldsymbol{r}(t))|\Psi(\boldsymbol{r}(t))\rangle \tag{5.5}$$

The energies in Equation 5.5 are parametric functions of the bath coordinates, $\boldsymbol{r}$ at time t.

One must be careful in performing the adiabatic separation for the fq models because the electronic coordinates, $\boldsymbol{q}$ are fast relative to the vibrational motion of Q. It would be incorrect to follow the previous method to find H_{sb} by expanding in a Taylor series about $Q = 0$, [5] without displacing the charges. Instead, we find H_{sb} for both the fixed charge and fq models by holding all atomic positions fixed, translating the H and O atoms that define Q in 0.1 Å intervals while leaving the center of mass for the vibration fixed. $Q_i = Q_0 + i\Delta Q$. With all $\boldsymbol{r}$ fixed the total potential energy is a function of Q, $V(Q)$. However, changing the position of Q alters the values of $\boldsymbol{q}$ in the electrostatic potential so at each displacement of Q, we must find the new values of $\boldsymbol{q}$ with the extended Lagrangian method. This ensures that the electronic degrees of freedom remain on the minimum of the electrostatic potential at each step in Q. By repeating this process for several values of the displacement, we find H_{sb} at each Q_i,

$$H_{sb}(Q, \boldsymbol{q}(Q); \{\boldsymbol{r}\})_i = V(Q_i) - V(Q = 0), \tag{5.6}$$

where $V(Q = 0)$ is the potential energy at the position of Q prescribed by the

intermolecular potential. Finally, we fit a third order polynomial to the discretely sampled H_{sb} to obtain a perturbative expression for H_{sb},

$$H_{sb} = FQ + GQ^2 + HQ^3, \tag{5.7}$$

and solve Equation 5.7 to second order in time-independent perturbation theory to obtain the vibrational frequencies for the $|1\rangle \leftarrow |0\rangle$ transition at 12 fs intervals in the simulation. While acquiring H_{sb}, we simultaneously obtain the transition dipole moment, $\boldsymbol{u} = \frac{\partial \boldsymbol{\mu}}{\partial Q}|_{Q=0}$, where $\boldsymbol{\mu}$ is the dipole moment of HOD. The experimental data used for comparison have been described in detail elsewhere [7, 8, 11].

5.2 Results and discussion

When comparing to experiment, the most straightforward quantity to examine is the IR absorption lineshape. Figure 5-1 shows the predictions from the fq and fixed charge models in comparison to experiment. The SPC/E potential is a "reference" water potential. We have shown in Chapter 2 that this potential produces IR lineshapes and TCFs that compare qualitatively well with experiment. The polarizable counterpart, to SPC/E on the other hand, SPCfq predicts a lineshape that is in stark constrast to the experimentally measured one. The origin of this disagreement is in the distribution of frequencies for this model (Table 5.2). The standard deviation is $\approx$ 3 times larger than that estimated from experiment. Clearly, for the IR absorption line shape predicted with this model is an outlier.

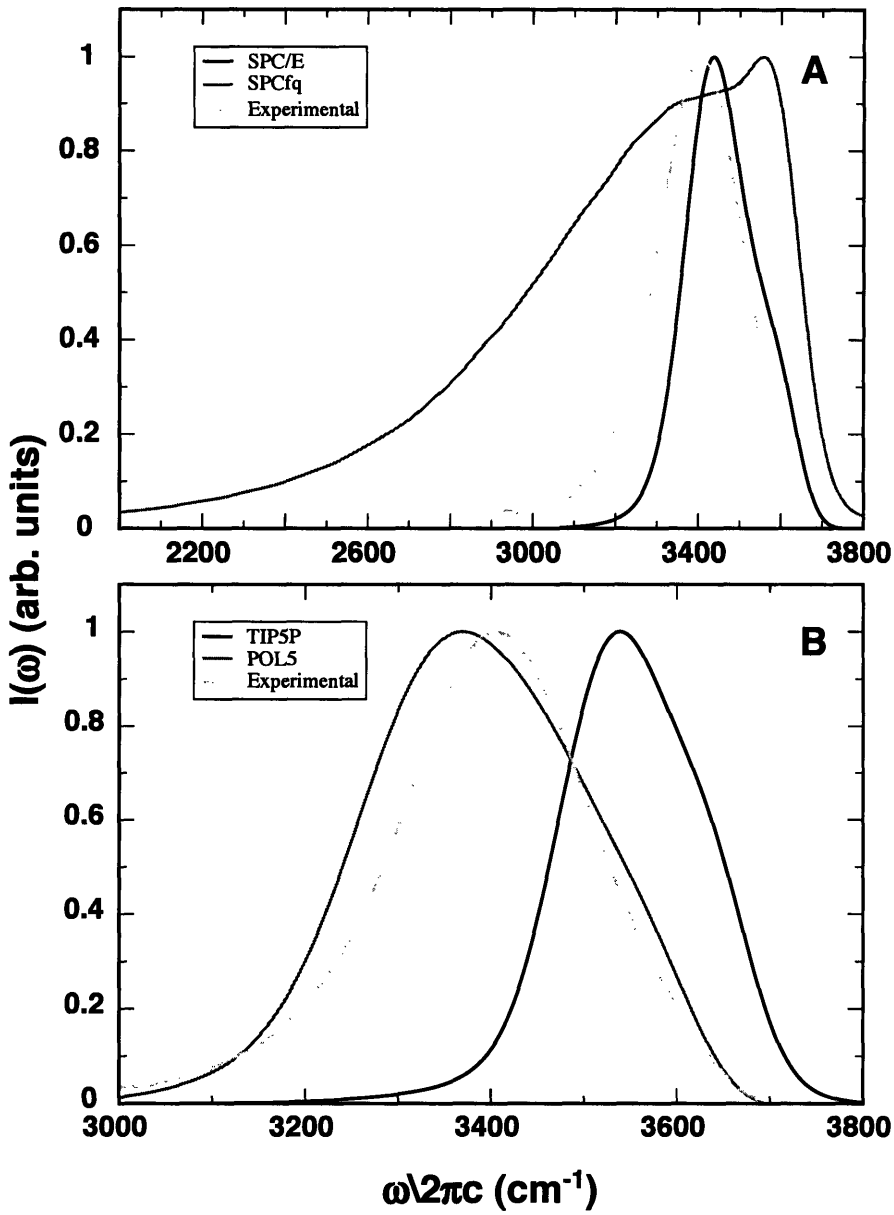

Figure 5-1: Absorption spectra of HOD in D_2O and comparison to experiment for polarizable and fixed charge models. The absorption spectrum is slightly asymmetric with a steeper tail on the blue side than on the red. The width (FWHM) of the experimental spectrum is 245 cm^{-1}. **(A)** Computed absorption spectra of SPCE and SPCfq models of water. The SPCfq model predicts a spectral width in stark contrast with experiment (FWHM of $\approx$ 670 cm^{-1}). The SPC/E model has a FWHM of $\approx$ 200 cm^{-1}. **(B)** The spectrum of the TIP5P model slightly underestimates the width ($\approx$ 190 cm^{-1} FWHM), but the POL5 model overestimates it by about the same amount ($\approx$ 300 cm^{-1} FWHM). Molecular polarizability increases the width of the absorption line shapes dramatically, but the notable disagreement of SPCfq with experiment implies that it is a poor model of molecular polarizability.

The TIP5P potential gives an IR absorption lineshape that is narrower than the experimental spectrum by ≈ 50 cm^{-1} (FWHM) and shifted ≈ 140 cm^{-1} to the blue. Its polarizable counterpart, POL5, is ≈ 60 cm^{-1} wider than the experimental spectrum but peaks at nearly the same position. Including molecular polarizability improves modestly upon the predictions from the TIP5P model for the IR absorption line shape.

The IR experiments are sensitive to the dynamics of molecular environments. At early times, these dynamics should be sensitive to the microscopic details of the potential energy, including the effects of polarizability. To make a quantitative comparison between the TCFs from simulation and those extracted from the experiment, we fit both TCFs with a bi-exponential function that models the decay of the fast and slow parts.

$$C_{\omega\omega}(t) = Ae^{-t/\tau_{\text{fast}}} + Be^{-t/\tau_{\text{slow}}}, \tag{5.8}$$

$$C_{\text{or}}(t) = Ae^{-t/\tau_{\text{l}}} + Be^{-t/\tau_{\text{or}}}. \tag{5.9}$$

Table 5.2 summarizes the results of the comparison between predictions from the water models and the experiments.

Figure 5-2 displays the normalized $C_{\omega\omega}(t)$ for the comparable fq and polarizable models. These data exhibit some general trends. Including polarizability increases the long time decay of $C_{\omega\omega}(t)$. Our results for the long time decay of $C_{\omega\omega}(t)$ are consistent with the findings of Xu *et al.*, who examined the decay of the hydrogen bonding characteristic function in water for polarizable and fixed charge models.

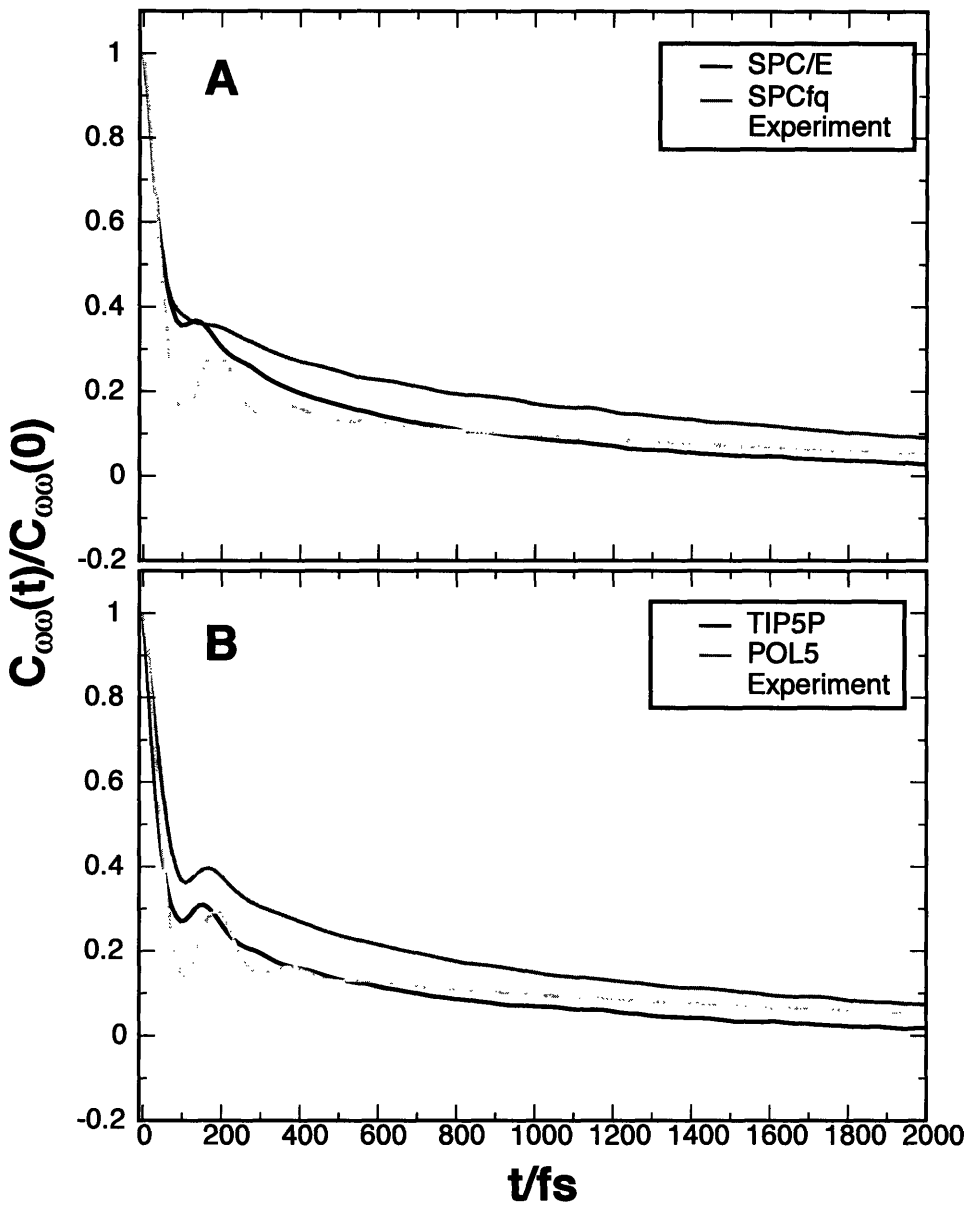

Figure 5-2: Frequency-Frequency correlation functions for the OH stretch of HOD in liquid D_2O for various polarizable and fixed charge models **(A)** Normalized $C_{\omega\omega}(t)$ for SPC/E (black) and SPCfq (red). SPCfq does not predict a beat. **(B)** Normalized $C_{\omega\omega}(t)$ for TIP5P (black) and POL5 (red) models. The beat frequency in these models is slightly closer to that measured from the IR3PEPS experiment. The long time decay for both polarizable models is similar, with a time constant of $\approx$ 1 ps, and for both fixed charge models is $\approx$ 600 fs. The short time exponential decay time for all models is $\approx$ 30 fs.

Model Name	τ_{fast}/fs	τ_{slow}/fs	τ_{or}/ps	FWHM/ cm^{-1}	$\frac{\sigma_{\omega_{\text{OH}}}}{2\pi}$/ cm^{-1}
Experiment	35	1450	3.0	245	126
SPC/E	40	700	2.4	204	103
SPCfq	37	1360	3.2	670	411
TIP5P	30	650	2.0	190	190
POL5	43	1130	3.7	305	140

Table 5.1: Summary of the results for fq and fixed charge models for TCFs and comparison to the experiment. To maintain consistency, the experimental values come from the bi-exponential fit of Equation 5.8, so that the values for the fast and slow time scales are different than those reported in Chapter 4 and Ref. [8] because the functional form is different. The standard deviation ($\frac{\sigma_{\omega_{\text{OH}}}}{2\pi} = \sqrt{C_{\omega\omega}(t=0)}$) appears in the last column.

They found that the decay time of the long time component increased in the polarizable water models. While we disagree about the meaning of the decay of the characteristic function, these results are consistent with the interpretation that the long time decay of $C_{\omega\omega}(t)$ corresponds to a cooperative process, where the microscopic details of the potential energy are unimportant. These results suggest that on long length scales, molecular polarizability makes fluctuations more sluggish but the specific details about the potential are not important on this time scale.

We have also calculated $C_{\text{or}}(t)$ for the various water models. For the fixed charge models, $C_{\text{or}}(t)$ is the second Legendre polynomial reorientational correlation function for the the OH bond, but for the fq models we computed the transition dipole moment directly from the derivative of the molecular dipole moment with respect to the OH stretch. Figure 5-3 shows the results. In general, the shapes of these functions look the same. The underdamped oscillations at early times are from the librational motions of water molecules. Interestingly, in SPCfq these motions are damped away, leaving only a weak shoulder. TIP5P and POL5 show the opposite trend; the beats appear

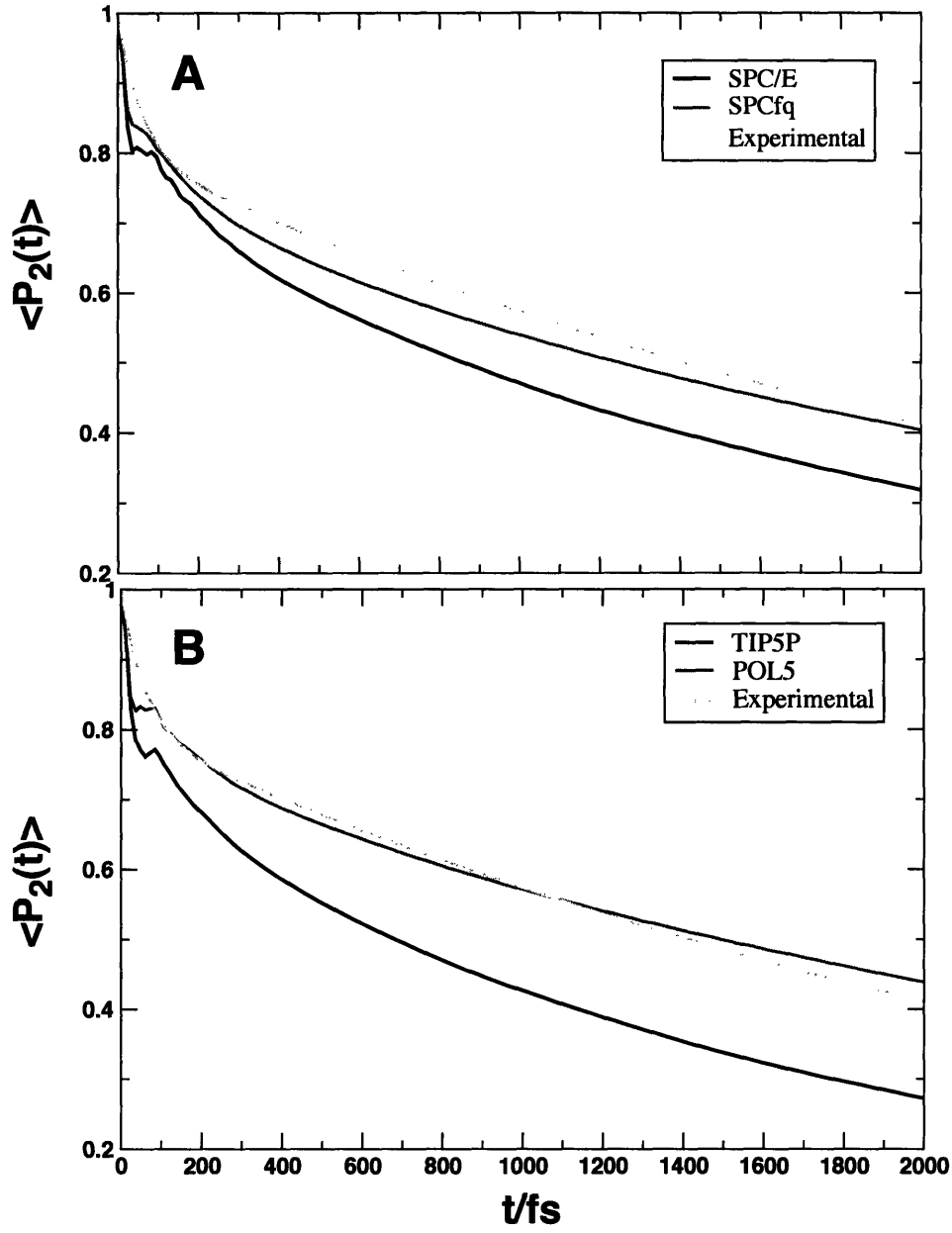

Figure 5-3: Reorientational motion in fixed charge and fq models. **(A)** SPC/E (black) and SPCfq (red) models of water. The SPC/E model shows underdamped beats from the librations of individual molecules while the SPCfq model does not. **(B)** TIP5P (black) and POL5 (red) show the opposite trend; the beats appear in the fq model but not in the fixed charge one. The long time decays are all similar, but are longer in the fq models than in the fixed charge models.

in the fq model but not in the fixed charge one. Including molecular polarizability makes the long time decay longer in all of these models, but all of the models predict a decay time within ≈ 30 % of the experimental value.

Unlike comparable fixed charge models (SPC,SPC/E,TIP4P), the TIP5P model of water accurately predicts the anomalous density maximum above the freezing point at $\approx 4°$ C [19]. It also gives reasonable results for the vibrational spectroscopy of water. The predictions from the POL5 model are an obvious improvement over those from TIP5P. Including molecular polarizability shifts the mean frequency down to a more reasonable value. Because the mean frequency is the average electric field at the proton, including molecular polarizability in the water model yields a more accurate representation of the molecular electric field strengths. Likewise, the standard deviation $\sigma_{\omega_{OH}}$ has improved by adding molecular polarizability. Taken as a whole, however, POL5 only marginally gives better estimates for the experimental data than SPC/E. Unfortunately, the computational cost of POL5 is much higher than in any of the other models studied. There are situations where one could imagine it would be profitable to use the POL5 model (for example in the cold liquid near the freezing point), but one should employ the POL5 model only when quantitative detail is of the essence, and molecular polarizability is known or anticipated to be an important factor.

Remarkably, the long time decays for $C_{\omega\omega}(t)$ in all of the polarizable models are similar, ≈ 1 ps, even though the short time dynamics for $C_{\omega\omega}(t)$ in these models can be very different. In the SPCfq model, for example, the beat in $C_{\omega\omega}(t)$ is absent. The work of Balucani [2, 3] explains that the physical origin of the beat is the

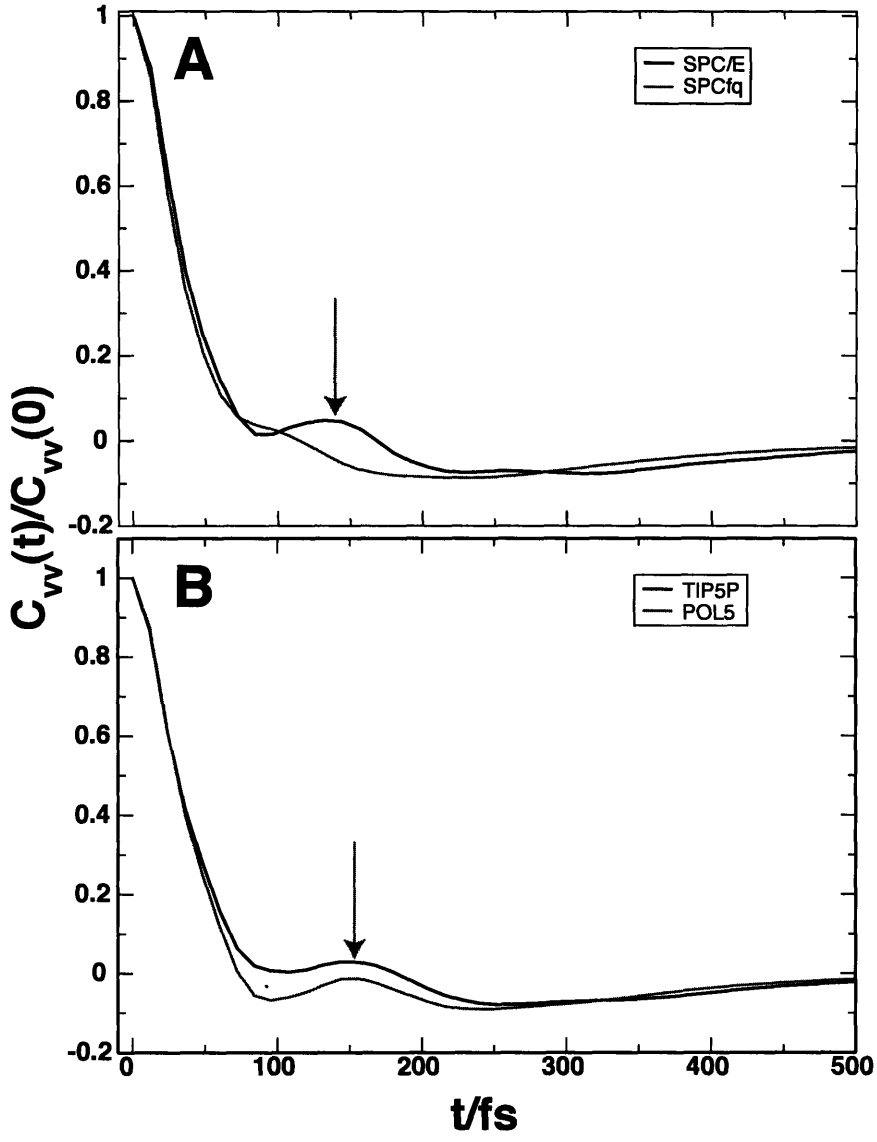

Figure 5-4: Center of mass velocity autocorrelation function for fixed charge and fq models examined in the text. **(A)** SPC/E (black) and SPCfq (red) models of water. The oscillations of R_{OO} appear at the beat frequency in $C_{\omega\omega}(t)$ for these models also appear in $C_{vv}(t)$. The blue arrow illustrates that the beat absent in $C_{\omega\omega}(t)$ from SPCfq is also absent in $C_{vv}(t)$. **(B)** $C_{vv}(t)$ for TIP5P (black) and POL5 (red). In both of these models, the beat frequency is slightly higher than in SPC/E, mirroring the same behavior for the beat in $C_{\omega\omega}(t)$.

competition between the attractive electrostatic forces of hydrogen bonding and the repulsive forces of neighboring oxygen atoms participating in a hydrogen bond. When two molecules approach each other, the dipole between them increases in the SPCfq model leading to an increased attraction, but the repulsion force is imbalanced. The difference in the depth of the Lennard–Jones potential for SPCfq is nearly twice the size as that in comparable fixed charge models [18].

We have examined the correlation function of R_{OO} independently to confirm that SPCfq does not properly capture this molecular motion. In SPCfq, both the beat in R_{OO} and the librational beats in $C_{or}(t)$ are overdamped. The shortcomings of the SPCfq model are evident in both the line shape and early time behavior of $C_{\omega\omega}(t)$. The source of the problem most likely lies in the current parameter set for SPCfq. The polarizability tensor element in the plane of the molecule but orthogonal to the C_2 axis of H_2O is larger than the gas phase by almost a factor of two ($2.26/\text{Å}^3$ in for SPCfq versus the gas phase value of $1.44/\text{Å}^3$). We have examined the velocity-velocity TCFs for all of the fixed charge and polarizable models as well (Figure 5-4). As one would expect from the results for $C_{\omega\omega}(t)$, the dynamics of SPCfq at early times are divergent from the predictions of the other models. This model shows no improvement over predictions from SPC/E. On the contrary, the effects of molecular polarizability in this model are highly exaggerated and lead to larger discrepencies between the experimental data. The parameterization for SPCfq should be re-examined to better balance the induced attractions from the polarizable interactions and the empirical repulsions.

5.3 Acknowledgements

I would like to thank Edward Harder and Bruce Berne for running the MD simulations of the fq and fixed charge water models.

Bibliography

[1] M.P Allen and D.J. Tildesley. *Computer Simulation of Liquids.* Oxford University Press, 1989.

[2] U. Balucani, J.P. Brodholt, and R. Vallauri. Analysis of the velocity autocorrelation function of water. *J. Phys. : Condens. Matter*, 8:6139–6144, 1996.

[3] U. Balucani, G. Ruocco, M. Sampoli, A. Torcini, and R. Vallauri. Evolution from ordinary to fast sound in water at room temperature. *Chemical Physics Letters*, 209(4):408–416, 1993.

[4] H.J.C. Berendsen, J.R. Grigera, and T.P. Straatsma. The missing term in effective pair potentials. *J. Phys. Chem.*, 91:6269–6271, 1987.

[5] J. D. Eaves, A. Tokmakoff, and P. Geissler. Electric field fluctuations drive vibrational dephasing in water. *In preparation*, 2004.

[6] C. J. Fecko, J. D. Eaves, and A. Tokmakoff. Isotropic and anisotropic raman scattering from molecular liquids measured by spatially masked optical kerr effect spectroscopy. *J. Chem. Phys.*, 117(3):1139–1154, 2002.

[7] C.J. Fecko, J.D. Eaves, J.J. Loparo, A. Tokmakoff, and P.L. Geissler. Local and collective hydrogen bond dynamics in the ultrafast vibrational spectroscopy of liquid water. *Science*, 301:1698–1702, 2003.

[8] C.J. Fecko, J.L. Loparo, S. R. Roberts, and A Tokmakoff. Submitted. *Journal of Chemical Physics*, 2004.

[9] G.R. Fleming and M. Cho. Chromophore-solvent dynamics. *Annu. Rev. Phys. Chem.*, 47:109–34, 1996.

[10] C. P. Lawrence and J. L.. Skinner. Vibrational spectroscopy of hod in liquid d2o. i. vibrational energy relaxation. *Journal of Chemical Physics*, 117:5827–5838, 2002.

[11] J. J. Loparo, C. J. Fecko, J. D. Eaves, S. T. Roberts, and A. Tokmakoff. Reorientational and configurational fluctuations in water observed on molecular length scales. *Physical Review B*, 2004.

[12] K. B. Moller, R. Rey, and J. T. Hynes. Hydrogen bond dynamics in water and ultrafast infrared spectroscopy: A theoretical study. *J. Phys. Chem. A*, 108:1275–1289, 2004.

[13] A. Novak. Hydrogen bonding in solids. correlation of spectroscopic and crystallographic data. In J. D Dunitz, P. Hemmerich, R. H. Holm, J. A. Ibers, C. K. Jorgenson, J. B. Neilands, D. Reinen, and R. J. P. Williams, editors, *Structure and Bonding*, volume 18, pages 177–216. Springer-Verlag, New York, 1974.

[14] Aneesur Rahman and Frank H. Stillinger. Molecular dynamics study of liquid water. *J. Chem. Phys.*, 55:3336–3359, 1971.

[15] Aneesur Rahman and Frank H.. Stillinger. Propagation of sound in water. molecular-dynamics study. *Physical Review A: Atomic, Molecular, and Optical Physics*, 10:368–78, 1974.

[16] J. R. Reimers and R.O. Watts. A local mode potential function for the water molecule. *Mol. Phys.*, 52(2):357–381, 1984.

[17] Rossend Rey, Klaus B. Moller, and James T.. Hynes. Hydrogen bond dynamics in water and ultrafast infrared spectroscopy. *Journal of Physical Chemistry A*, 106:11993–11996, 2002.

[18] Steven W. Rick, Steven J. Stuart, and B.J. Berne. Dynamical fluctuating charge force fields: Application to liquid water. *J. Chem. Phys.*, 101:6141–6156, 1994.

[19] S.W. Rick. A reoptimization of the five-site water potential (tip5p) for use with ewald sums. *Journal of Chemical Physics*, 2004.

[20] Pier Luigi Silvestrelli and Michele Parrinello. Structural, electronic, and bonding properties of liquid water from first principles. *J. Chem. Phys.*, 111(8):3572–3580, 1999.

[21] Harry A. Stern, George A. Kaminski, Jay L. Banks, Ruhong Zhou, B. J. Berne, and Richard A. Friesner. Fluctuating charge, polarizable dipole, and combined models: Parameterization from ab initio quantum chemistry. *Journal of Physical Chemistry B*, 103:4730–4737, 1999.

[22] Harry A. Stern, F. Rittner, B. J. Berne, and Richard A. Friesner. Combined fluctuating charge and polarizable dipole models: Application to a five-site water potential function. *Journal of Chemical Physics*, 115:2237–2251, 2001.

[23] F.H. Stillinger. Theory and molecular models for water. *Adv. Chem. Phys.*, 31:1–101, 1975.

[24] Frank H. Stillinger. Water revisited. *Science*, 209(4455):451–457, 1980.

[25] Huafeng Xu, Harry A. Stern, and B.J. Berne. Can water polarizability be ignored in hydrogen bond kinetics? *J. Phys. Chem. B*, 106:2054–2060, 2002.

[26] R.H. Zhou, E. Harder, H.F. Xu, and B.J. Berne. Efficient multiple time step method for use with ewald and particle mexh ewald for large biomolecular systems. *Journal of Chemical Physics*, 2001.

Chapter 6

Hydrogen bond dynamics in water

There is extensive evidence that liquid water maintains the tetrahedral geometry of ice on molecular length scales, but lacks about 10 % of the hydrogen bonds formed in a perfect crystal. These broken hydrogen bonds could exist either as a species in stable equilibrium with intact hydrogen bonds, or as frequent fluctuations that encourage hydrogen bonds to change partners. A water molecule at ambient conditions spends about half its time engaged in only three out of four possible hydrogen bonds. Support for this estimate comes broadly, from latent heats of melting and vaporization, from x-ray and neutron scattering [26], and in very detailed form from MD simulations [29]. It is thus possible to conceive of a "broken hydrogen bond" as a distinct molecular state, interconverting with the hydrogen bonded state (HB) at a rate determined by the transition state separating them. In this scenario, hydrogen bonds change partners in a stepwise mechanism. Alternatively, non-hydrogen bonded species (NHB) could be an intrinsically unstable and transient state that appears during natural fluctuations about a hydrogen bond or when molecules trade hydrogen

bonding partners. This mechanism is concerted, where molecules trade hydrogen bonding partners only when a new bonding partner becomes available. Indeed, these possibilities, illustrated in Figure 6-1, immediately suggest a role for water in mediating the dynamics of biological, chemical, and physical change in solution. Such questions remain unresolved because of the experimental challenges of isolating signatures of NHB from HB on the time scale of intermolecular motions in water ($\approx$ 100 fs).

Ultrafast infrared (IR) spectroscopy of the OH stretching vibration has opened a promising new route for characterizing broken hydrogen bonds [15, 12, 33, 28, 35, 9, 27]. Chapter 4 showed that in a dilute solution of HOD in D_2O, the proton is sensitive to hydrogen bonding and dielectric fluctuations [17, 22, 9]. As a result, the average OH frequency is several hundred wavenumbers lower than in the gas phase, and the line shape is broad (245 cm^{-1}). The red-shift from the gas phase is roughly proportional to the hydrogen bonding distance between donor and acceptor (Chapter 4). Thus, the high-frequency (blue) side of the IR spectrum reflects molecules that interact less strongly with their neighbors, including NHBs [17, 16]. Femtosecond spectroscopies that probe the time evolution of the OH stretch frequency, $\omega_{OH}(t)$, for selected groups of molecules might provide a glimpse of hydrogen bonds breaking and forming.

In Chapter 4, we compared $C_{\omega\omega}(t)$ from simulation to that extracted from a IR3PEPS experiment. Microscopic information about hydrogen bonding is most apparent at short times ($<$ 200 fs) in $C_{\omega\omega}(t)$, but on time scales longer than this, spectral relaxation of ω_{OH} was insensitive to specific hydrogen bonding dynamics. As a result,

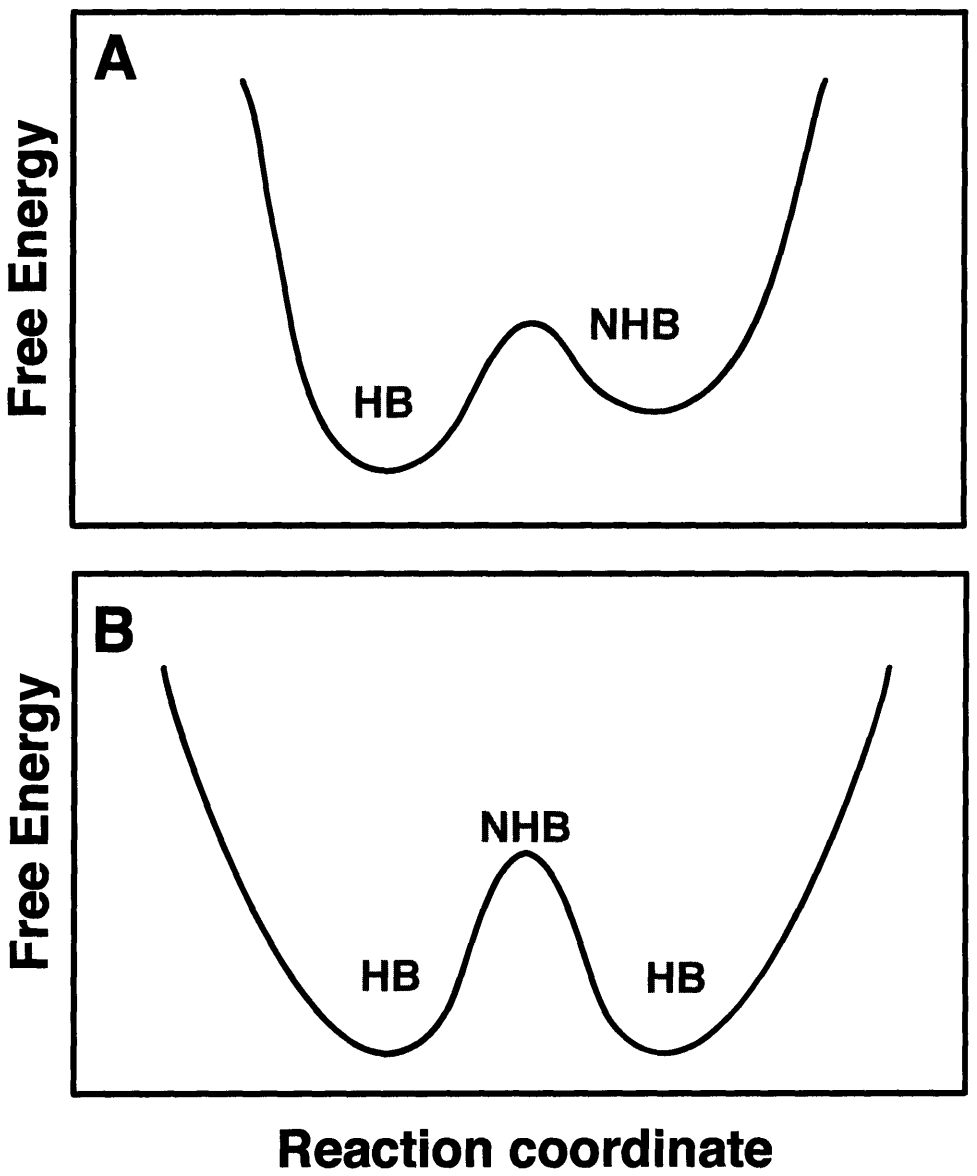

Figure 6-1: Two different pathways for hydrogen bond rearrangement in water. **(A)** depicts the stepwise mechanism where NHBs are in stable chemical equilibrium with HBs. Hydrogen bonds rearrange by first entering into the NHB state and then by re-crosssing the barrier to form HBs with new partners. **(B)** shows the concerted mechanism, where NHBs are an intrinsically unstable chemical species. They appear as distortions in the hydrogen bond network that are natural fluctuations at equilibrium or configurations that molecules visit when changing hydrogen bond partners.

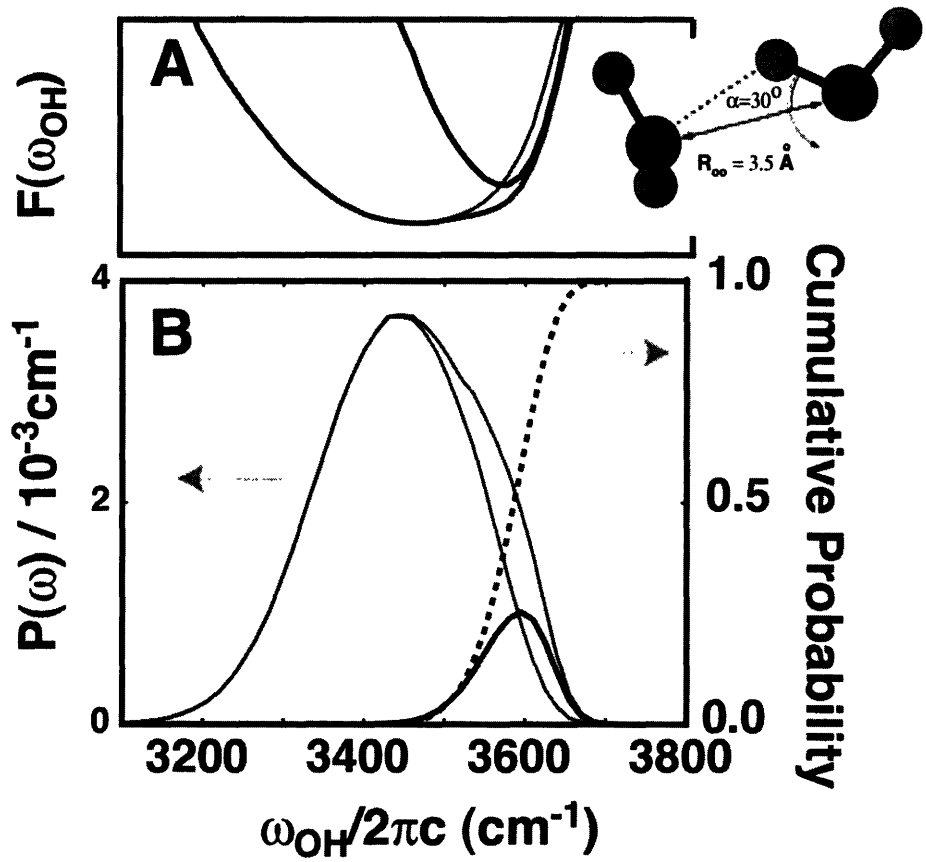

Figure 6-2: Hydrogen bonding relationships of HOD In D_2O from MD simulations. **(A)** The free energy as a function of ω_{OH}, defined by $\beta F(\omega_{OH}) = -ln(P(\omega_{OH}))$, separated into hydrogen bonded (HB) and non hydrogen bonded (NHB) contributions. We used standard geometrical criteria (see text) to discriminate HB from NHB. **(B)** The frequency distribution, $P(\omega_{OH})$ is a time-average from several ergodic trajectories of ω_{OH}. The dashed line is the cumulative probability of selecting an NHB molecule as a function of ω_{OH}. The probability of selecting NHB reaches 66 % at $\omega_{OH} \approx 3600$ cm^{-1}. The inset is a diagram of the geometrical criterion used to separate HBs from NHBs.

$C_{\omega\omega}(t)$ could not provide a detailed picture of how hydrogen bonds rearrange in water. For this task, we turn to 2D IR experiments. Conceptually, the 2D IR experiment spectrally labels molecules in different hydrogen bonding environments and observes their evolution during the waiting time, T. It is a more informative technique that IR 3PEPS because the spectroscopic measure is not a two-point correlation function, but rather a detailed map of how ω_{OH} evolves as a function of T. To translate dynamics of ω_{OH} into motions of the hydrogen bond, we marry the concepts and methods of nonlinear spectroscopy with those of reaction dynamics.

In Section 6.1 I develop the language of reaction dynamics in complex systems and apply it to describe hydrogen bond dynamics in water. In Section 6.2 I show how notions from reaction dynamics can be applied directly to spectroscopic observables. Section 6.3 is a discussion of linear response relationships for frequency fluctuations and shows that for a reactive system, including HOD in liquid D_2O, coupling of the frequency to a reactive chemical coordinate generates nonlinear frequency dynamics. The simulation guides our intuition for analyzing the 2D IR experiment, which I do in 6.6 where I compute 2D IR spectra, compare them to experiment, and interpret the results.

6.1 The language of reaction dynamics

Reaction dynamics is the art of identifying the few physically relevant microscopic variables that participate in a complex many-bodied chemical reaction. This enormous reduction in complexity returns a highly simplified description of the chemical

reaction and provides a physical picture for how the reaction occurs. Hydrogen bonding in water is a chemical reaction, akin to isomerization. Because I will draw on many concepts from reaction dynamics, it is useful to discuss the general unimolecular chemical reaction in detail before confining attention to hydrogen bonding in water. Section 6.1.1 describes the phenomenology of reaction kinetics for reactions in liquids. Section 6.1.2 shows how an comparable phenomenology based on linear response theory for perturbations in the concentration of a species can be used to analyze two-state reactive systems with MD simulations. For concreteness, I analyze the hydrogen bond making and breaking reaction for HOD in liquid D_2O using this methodology [20, 19, 34]. By default, such analysis postulates a stepwise mechanism. Section 6.1.3 introduces the important concepts of order parameters and reaction coordiantes. For the vibrational spectroscopy of HOD in liquid D_2O, ω_{OH} is an order parameter that aims to distinguish HBs from NHBs (Figure 6-2). In Section 6.1.5 I review a technique that uses projection operators [36] to generate a Langevin Equation for the reaction coordinate in a reactive chemical system. Section 6.1.4 describes how notions of stability in nonlinear dynamical systems typically used to locate the transition state [7, 3] can also identify ambiguous chemical species (NHBs).

6.1.1 The anatomy of a chemical reaction

In a kinetics experiment in the laboratory, one measures the concentrations of reactants and products as a function of time during the progress of a chemical reaction. The chemical equation for the unimolecular (two-state) reaction is $A \rightleftharpoons B$, where A

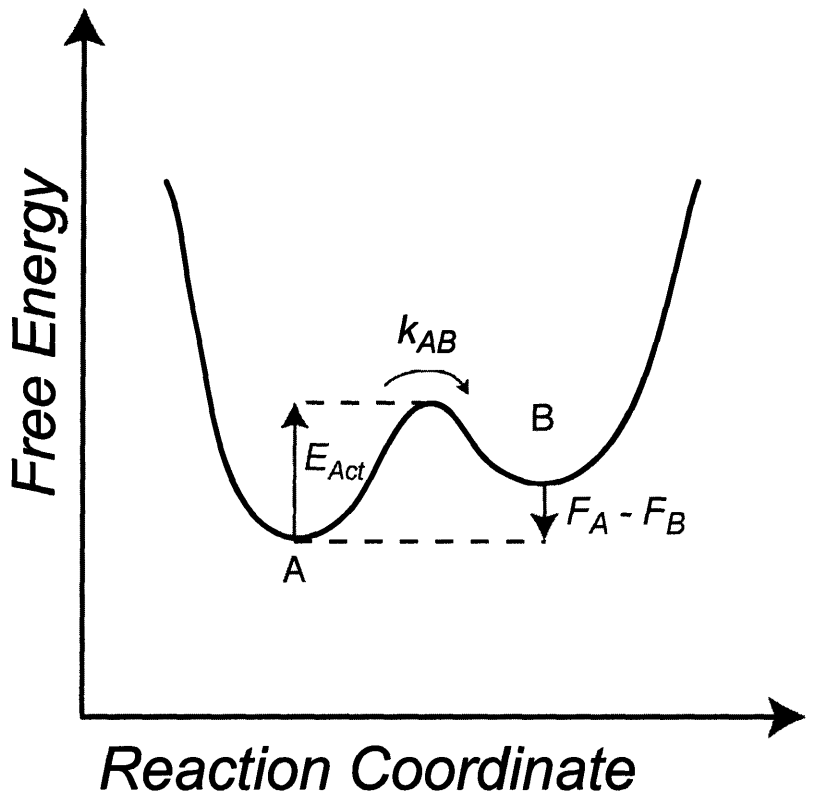

Figure 6-3: Free energies and phenemenology for a two-state chemical reaction. The reaction coordinate is a progress variable for the reaction. The chemical states A (reactants) and B (products) are minima of of the free energy along the reaction coordinate. The blue line shows the free energy difference between reactant and product states (Equation 6.2). The maximum of the free energy along the reaction coordinate is the transition state. E_{Act} is the Arrhenius activation energy. k_{AB} is the rate for the forward reaction.

represents the reactants and B the products. The concentrations of A and B (C_{A} and C_{B}) follow the familiar first order rate equations,

$$\begin{aligned} \frac{dC_{\mathrm{A}}(t)}{dt} &= -k_{\mathrm{AB}}C_{\mathrm{A}}(t) + k_{\mathrm{BA}}C_{\mathrm{B}}(t), \\ \frac{dC_{\mathrm{B}}(t)}{dt} &= k_{\mathrm{BA}}C_{\mathrm{A}}(t) - k_{\mathrm{BA}}C_{\mathrm{B}}(t), \end{aligned} \tag{6.1}$$

where k_{AB} is the reaction rate for going from A to B and k_{BA} is the reaction rate for the reverse reaction. The reversible work needed to convert A to B is the free energy difference between reactant and product states. In terms of the ratio of populations between A and B at thermodynamic equilibrium,

$$e^{-\beta(F_{\mathrm{A}}-F_{\mathrm{B}})} = \frac{C_{\mathrm{A}}}{C_{\mathrm{B}}} = \frac{1}{k_{\mathrm{eq}}}, \tag{6.2}$$

where k_{eq} is the equilibrium constant for the forward reaction. The steady state condition from Equation 6.1 can also be used to express the ratio of concentrations.

$$\frac{C_{\mathrm{A}}}{C_{\mathrm{B}}} = \frac{k_{\mathrm{BA}}}{k_{\mathrm{AB}}}. \tag{6.3}$$

Arrhenius noted that the log of the reaction rate vs. inverse temperature was a straight line. His equation for the rate constant is another phenomenological expression that describes the temperature dependence of the reaction rate

$$ln(k_{\mathrm{AB}}(\mathrm{T})) = ln(\mathcal{A}) - \frac{E_{\mathrm{Act}}}{R\mathrm{T}}, \tag{6.4}$$

where R is the ideal gas constant, $\mathcal{A}$ is the Arrhenius prefactor, T the temperature, and E_{Act} is the "activation energy." E_{Act} is the slope in the plot of $ln(k_{\mathrm{AB}}(\mathrm{T}))$ vs. $-\frac{1}{RT}$.

From kinetics experiments, one constructs a diagram that details the anatomy of the chemical reaction. Figure 6-3 is the phenomenological picture of a unimolecular chemical reaction. It has three key features; the reaction coordinate, which describes the progress of the reaction; the reactant and product states, which are the free energy minima; and a transition state at the free energy maximum between reactants and products. The free energy difference between the transition state and the reactant state is the Arrhenius activation energy, E_{Act}. The phenomenological rates and free energies are useful for describing the rate of conversion between reactants and products, but they do not explain *how* reactants transform into products.

6.1.2 Two-state kinetics and linear response theory

In this section we will show how a comparable phenomenology to that developed in the previous section can be applied to MD simulations. Two putative species, A and B are constructed and appropriate analysis of time correlation functions gives the rates of going between A and B. This type of calculation is called a reactive flux calculation. In water, the reactants (A) are HB and the products (B) are NHB defined by the conventional geometric criteria, and the rates are the making and breaking rates. The inferred rates are only sensible if both HB and NHB are stable chemical species. In other words, the reactive flux calculation assumes a two-state chemical

model.

The reactive flux calculation relates the changes in concentration to fluctuations of concentrations at equilibrium. Conversely, if one believes the geometric criteria distinguish between HB and NHB, one can locate the transition state and discern how molecules make and break hydrogen bonds in the stepwise mechanism [5]. Here I outline the framework of the reactive flux calculation and show that rates obtained from it imply a stepwise mechanism for hydrogen bond dynamics in water.

If we focus on the hydrogen bonding state of the HOD molecule and ignore the mutual diffusion of HOD and the hydrogen bonding partner, we can consider the HOD molecule and its hydrogen bonding partner to be members of a closed system. Over the distances between molecules in the first solvation shell, the sum of the concentration of NHB and HB is constant. If NHB are a stable chemical species, one can expect the concentrations of HB and NHB to satisfy the first order kinetic equations,

$$\begin{aligned} \frac{d\,C_{\mathrm{HB}}}{dt} &= -k_{\mathrm{break}} C_{HB}(t) + k_{\mathrm{form}} C_{\mathrm{NHB}}(t), \\ \frac{d\,C_{\mathrm{NHB}}}{dt} &= k_{\mathrm{break}} C_{HB}(t) - k_{\mathrm{form}} C_{\mathrm{NHB}}(t). \end{aligned} \tag{6.5}$$

The hydrogen bond breaking (making) rate, k_{break} is the probability per unit time of breaking (forming) an intact hydrogen bond, and C_{HB} is the number of hydrogen bonded molecules per unit volume. Now imagine introducing a perturbation that changes the concentration of NHB (i.e. $C_{\mathrm{HB}}(t) \rightarrow C_{\mathrm{HB}}(t) + \delta C_{HB}(t)$). Because

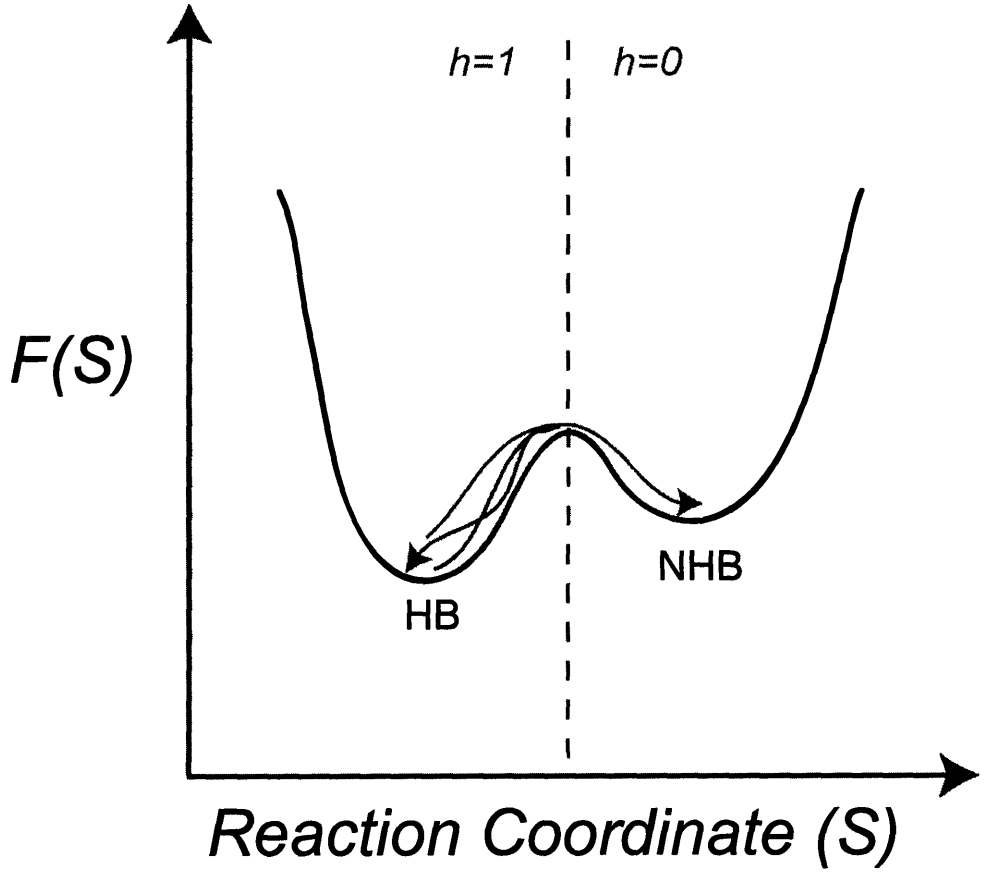

Figure 6-4: Schematic of two-state kinetics for hydrogen bond dynamics in water. This model is implicit in most studies of hydrogen bond dynamics. The purple trajectory re-crosses the barrier after approaching the transition state on the time scale τ_{mol}. The red trajectory passes through the transition state and commits to NHB on a longer time scale. The characteristic function $h(t) = 1$ when the molecule is engaged in a hydrogen bond and zero otherwise.

$\frac{d(C_{\mathrm{HB}}+C_{\mathrm{NHB}})}{dt} \approx 0$, the perturbation also obeys first order kinetics

$$\frac{d\,\delta C_{\mathrm{HB}}}{dt} = (-k_{\mathrm{break}} - k_{\mathrm{form}})\delta C_{\mathrm{HB}}(t). \tag{6.6}$$

The solution to 6.6 is

$$\delta C_{\mathrm{HB}}(t) = \delta C_{\mathrm{HB}}(0)e^{-\tau_{rxn}t}, \tag{6.7}$$

$$\tau_{\mathrm{rxn}} = \frac{1}{k_{\mathrm{break}} + k_{\mathrm{form}}}, \tag{6.8}$$

$$\kappa_{\mathrm{equil}} = \frac{\langle C_{\mathrm{HB}}\rangle}{\langle C_{\mathrm{NHB}}\rangle} = \frac{k_{\mathrm{form}}}{k_{\mathrm{break}}}, \tag{6.9}$$

where κ_{equil} is the equilibrium constant, and τ_{rxn} is the inverse of the reaction time. Based on this phenomenology, a comparable picture to Figure 6-3 can be drawn for the hydrogen bonding reaction in water (Figure 6-4).

To make a connection to Equation 6.6, imagine introducing a biasing force to the Hamiltonian that changes the concentration of HB. The Hamiltonian describing the perturbed distribution is

$$\mathcal{H} = \mathcal{H}_0 - \epsilon g(t). \tag{6.10}$$

$\mathcal{H}_0$ is is the Hamiltonian of the unperturbed system, the characteristic function g is 1 in NHB and 0 in HB, ϵ is the auxiliary field that perturbs the concentration. Classical linear response theory [36] relates the correlation function of g to the concentration of HB.

$$\delta C_{\mathrm{HB}}(t) = \delta C_{\mathrm{HB}}(0)\frac{\langle \delta g(t)\delta g(0)\rangle}{\langle C_{\mathrm{HB}}\rangle\langle C_{\mathrm{NHB}}\rangle}. \tag{6.11}$$

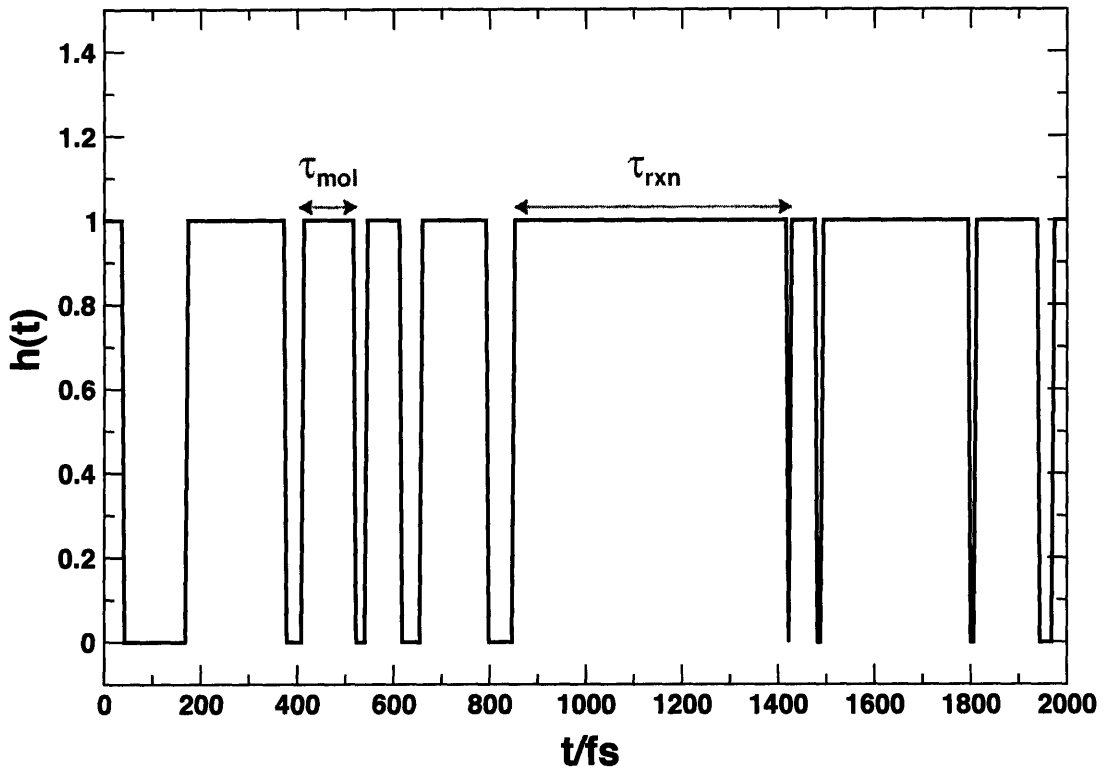

Figure 6-5: Trajectory of the hydrogen bonding characteristic function from MD simulation. In the two-state model, frequent fluctuations of $h(t)$ occur on $\tau_{\text{mol}} \approx 100$ fs, while the reaction time, τ_{rxn} indicative of barrier crossing is much longer (≈ 650 fs).

Comparing this to Equation 6.7, we see that τ_{rxn} is the exponential decay time of the correlation function for $\langle \delta g(t) \delta g(0) \rangle$. This function will not decay exponentially until after microscopic molecular motions have relaxed on a time, τ_{mol}. Loss of correlation prior to τ_{mol} is the result of fast re-crossings over the transition state.

Detailed balance allows one to obtain either the making or breaking rate from the ratio of populations of NHB or HB and the computed τ_{rxn}. Conventional studies of hydrogen bond kinetics in water define the related characteristic function, $h(t) =$

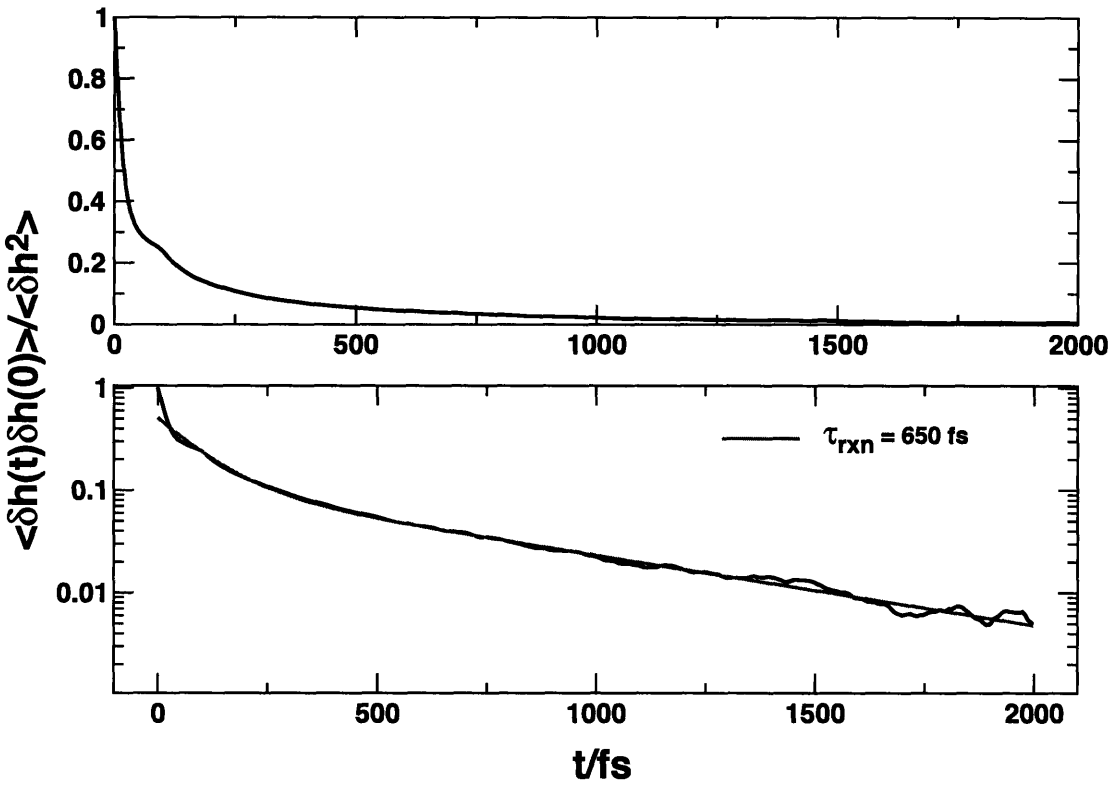

Figure 6-6: Reactive flux calculation for hydrogen bond breaking in the two-state model. The top panel is the normalized TCF for the characteristic function $h(t)$. The bottom panel is the same plot on a log scale. The red line is a bi-exponential fit that extracts τ_{rxn} for the two-state model.

$1 - g(t)$. Recall that by the "geometrical criteria," [20] the characteristic function, h is

$$h(t) = \begin{cases} 1 & \text{if } \cos(\alpha(t)) > \cos(30°) \text{ and } R_{OO} < 3.5\mathring{A}; \\ 0 & \text{otherwise.} \end{cases}$$

Evidently, the exponential decay times for the TCFs of g and h are the same. Figure 6-5 is a diagram of the fluctuations in a trajectory of $h(t)$, and Figure 6-6 is the TCF $\frac{\langle \delta h(t) \delta h(0) \rangle}{\langle \delta h^2 \rangle}$ along with the bi-exponential fit to extract τ_{rxn}. The similarity of the decay times for $C_{\omega\omega}(t)$ and $\frac{\langle \delta h(t) \delta h(0) \rangle}{\langle \delta h^2 \rangle}$ is notable. In contrast with the conclusions in Chapter 4, Lawrence and Skinner [16] have concluded that this similarity along with the relationship in Figure 6-2 implies that $C_{\omega\omega}(t)$ measures hydrogen bond kinetics at long times. Correlations of $\langle \delta h(t) \delta h(0) \rangle$ decay exponentially after τ_{mol}, but this does not validate the stepwise mechanism for hydrogen bond rearrangements in water. Rather, the reactive flux calculation *assumes* a stepwise mechanism, and computes a rate for the reaction within this framework. If NHBs are not a stable species, $\langle h(t) h(0) \rangle$ does not describe barrier crossing but instead characterizes the size of large fluctuations of HBs.

Notice that $\langle h(t) h(0) \rangle$ has the behavior one would anticipate for a barrier-crossing reaction: there is a fast relaxation on the time scale of $\approx$ 100 fs followed by an exponential decay. At this stage it is tempting to conclude that hydrogen bonding in water follows the stepwise mechanism, but recall that the reactive flux framework assumes this mechanism at the beginning of the calculation. With only the data from the reactive flux calculation, it is impossible to verify if the reaction is indeed a stepwise process or if relaxation in the TCF of the population operator is only a

characteristic of a complicated combination of R_{OO} and $\cos(\alpha)$.

6.1.3 Reaction coordinates and order parameters

The gross features of Figure 6-3 do not translate directly into a microscopic interpretation. The statistical mechanics of configurations provides some insight into the connection between the phenomenology developed in the laboratory and the role of atoms and molecules in the reaction. The statistical interpretation of the entropy for example, enumerates the configurations at the transition state. The number of atomistic configurations at the transition state is $N^{\ddagger} = e^{\frac{S^{\ddagger}}{k_B}}$, where $S^{\ddagger}$ is the entropy at the transition state. In "energetically dominated dynamics", the entropy of the transition state is negligible, and there are only a small number of configurations at the transition state. In this case, the potential energy guides the dynamics of the reaction and the transition state occurs at a saddle point in the potential energy landscape that separates reactants and products. In a process like nucleation or protein folding there are several statistical degrees of freedom that participate in the chemical reaction, so there can be many configurations a system can assume when transforming between reactants and products. Like the transition state, the number of molecular configurations in the reactant and product states scales exponentially with the entropy of the reactant and product states. The number of saddle points minima of the energy landscape scale exponentially with the number of degrees of freedom. Many of these are unimportant for the dynamics at room temperature. A language based on the statistics of configurations quickly lends itself to confusion. To

avoid such confusion, we will adopt the terminology used to describe the statistical mechanics of trajectories in reactive rare events [3, 7].

The order parameter is a variable that distinguishes between reactant and product states. In the simplest case, the order parameter and the reaction are the same variable. More generally, the order parameter is only related to the reaction coordinate. For example, the interatomic distance of a dissociating diatomic molecule in the gas phase distinguishes the stable covalently bonded dimer (reactant) from the stable atomic constituents (products). It is also the reaction coordinate. Most reactions in liquids are not so simple. The dissociation of table salt in liquid water provides an example where the reaction coordinate and order parameter are different. Geissler *et al.*[13] have found that the interionic separation serves as an order parameter to distinguish reactant and product states, but it is not the reaction coordinate. The dissociation mechanism requires a fluctuation in the local water density around the NaCl pair that allows a water molecule to separate them. Dissociation into Na^+ and Cl^- ions proceeds after six water molecules coordinate around the sodium atom. Clearly, this solvation coordinate is nearly independent of the interionic distance order parameter.

Experiments in the condensed phase seldomly measure the reaction coordinate directly, but rather observe an order parameter characterizing reactant and product states. As an example, consider an experiment that monitors the fluorescence intensity of a reactant and product as a function of time in a fast mixing experiment. If the reactant and product fluoresce at different wavelengths, the fluorescence intensity is proportional to the concentration of the chemical species monitors the course of

the reaction. For HOD in D_2O the order parameter is ω_{OH}. Figure 6-2 shows that ω_{OH} can, at least marginally, discriminate between HB and HNB molecules.

6.1.4 Reactive trajectories, attractors, and dynamical bottlenecks

The free energy as a function of reaction coordinate, S, depends on the choice of reaction coordinate.

$$exp(-\beta F(s)) = \frac{\int d\mathbf{\Gamma} e^{-\beta \mathcal{H}(\mathbf{\Gamma})} \delta(S(\mathbf{\Gamma}) - s)}{Z}, \tag{6.12}$$

In Equation 6.12, the chosen reaction coordiante S has a functional dependence on the phase space coordinates $\mathbf{\Gamma}$, and the Dirac δ function constrains the integral to values where $s = S(\mathbf{\Gamma})$. Z is the partition function, and the free energy $F(s)$ should be understood as the reversible work required to constrain the equilibrium system to a particular value of $S = s$. An unfortunate choice of S will lead to unrealistic barrier heights (compared to the empirically determined E_{Act}) for the transition state in the postulated reaction coordinate.

Typically, E_{Act} is sufficiently high relative to k_BT that there is a separation of time scales between the dynamics of barrier crossing and the duration of time spent in either the reactant or product regions. Physically, this corresponds to a rate-determining step, or dynamical bottleneck that trajectories navigate when moving between reactant and product basins. Figure 6-7 illustrates the problem encountered when the free energy maximum in a presumed reaction coordinate does not corre-

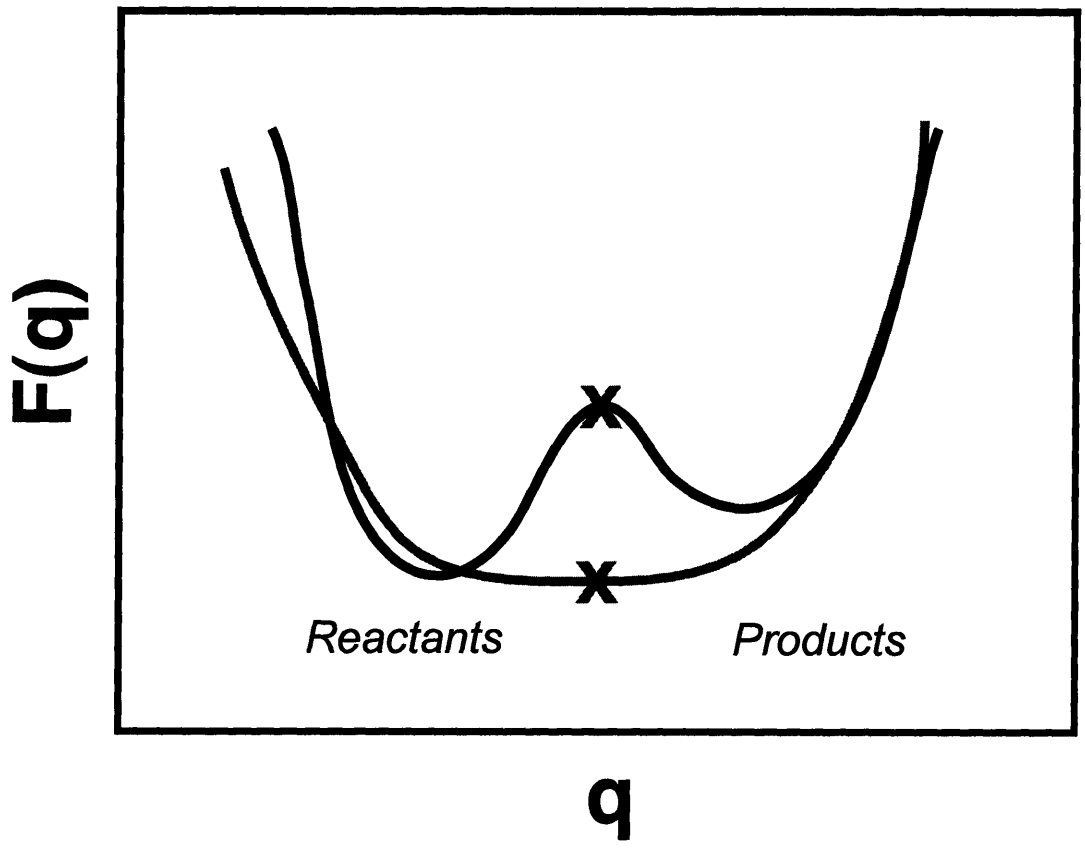

Figure 6-7: Order parameters and reaction coordinates in a unimolecular chemical reaction. q is an order parameter that distinguishes reactants from products. In the example used in the text, it could be the distance between anion and cation in the dissociation of table salt. The red "X" denotes the position on this coordinate where trajectories go through the rate-determining step. If q is a good reaction coordinate (black), the rate-determining step occurs at the free energy maximum. The purple curve illustrates the case where q is a poorly chosen reaction coordinate. In this case, the transition state separating reactants and products is in another coodinate.

spond to the bottleneck. Because it is often impossible to guess what the reaction coordinate is in a complex many-bodied system, it is more profitable in computer simulations to focus on the dynamical bottleneck, that separates products and reactants. Transition path sampling, for example, takes this approach [7, 3]. Either by performing a long enough simulation or by importance sampling [7, 3], one identifies a set of reactive trajectories from the simulation. Each trajectory passes through the dynamical bottleneck. Once these paths are harvested, the reaction coordinate can be inferred from them.

There are many atomistic degrees of freedom in a liquid and the intermolecular potential couples many, if not all of these coordinates. As a result, the equations of motion are nonlinear and trajectories in the system are chaotic. Trajectories with infintesimally close initial conditions diverge exponentially in phase space. On the computer, floating point round-off errors of $\approx O(10^{-15})$ cause trajectories to diverge in phase space so that they are statistically distinct after $\approx$ 10 ps [7].

Physically, we expect that the reactant and product must remain stable to thermal perturbations. For example, if we perturb the trajectory by instantaneously displacing the momenta of all particles in the system by a small amount, short trajectories (on the time scale of τ_{mol}) should remain in either the reactant or product state. Figure 6-8 is a diagram of both the stable chemical species and the dynamical bottleneck in a chemical reaction. The top panel of Figure 6-8 displays the requirement for stability. For the purposes of illustration, the ordinate and abscissa are configurational variables that classify the trajectory, and the black arrows are short trajectories initiated in the region of reactants or products. The region in trajectory space where

trajectories of duration τ_{mol} relax back to the reactants or products is called the basin of attraction for either reactants or products. The second panel illustrates the dynamical bottleneck. It repels trajectories from the origin in all directions except X so that only a small fraction of the trajectories successfully pass through the dynamical bottleneck. The ensemble of configurations at the dynamical bottleneck, called the transition state ensemble [7, 3], constitute the transition state for the reaction. Likewise, the ensemble of configurations in the basins of attraction comprise the reactants and products [7, 3]. These identifications of both the transition state and the reactants and products in the chemical reaction are based on notions of stability, and are free from preconceived bias one might have about the reaction coordinate.

Because we assume the system is ergodic, the connection to theromodynamic free energies and the features labled in Figure 6-3 comes from averaging over trajectories. In the basins of attraction, for example, the density of trajectories is high, but in the region of the dynamical bottleneck the density of trajectories is low. A "good" reaction coordinate, to be defined in detail in Section 6.1.5, has a distribution of commitors that is sharply peaked at the transition state [7, 3]. Figure 6-9 is a is a cartoon of trajectories and free energies in a complex system.

6.1.5 Reduced equations of motion

Our discussion of reaction coordinates so far has been physically motivated. We want to describe the motion of the complex reactive system with as few physically relevant degrees of freedom as possible, and come up with a good approximation for how all the

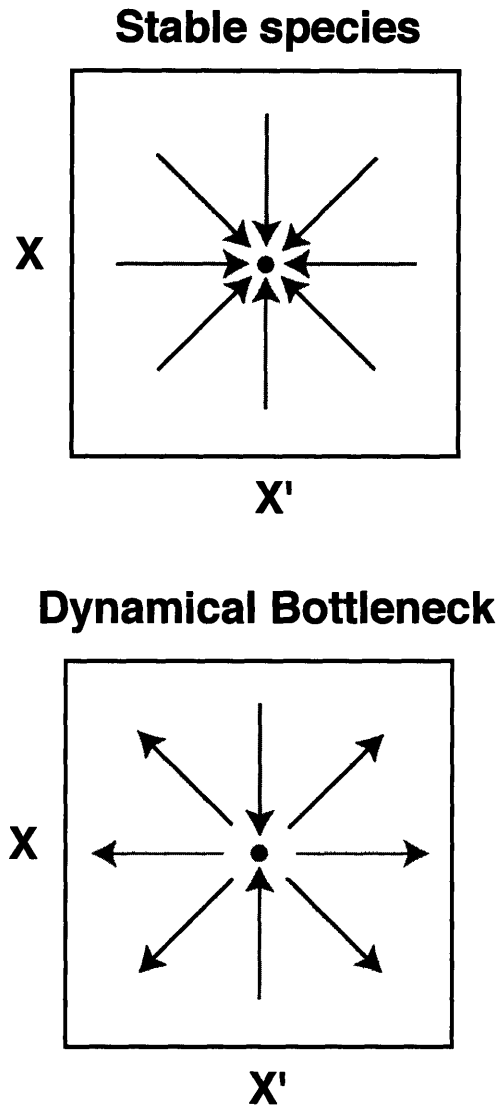

Figure 6-8: Trajectory maps and stability. X and X' are configurational coordinates that for purposes of illustration classify trajectories. The top panel shows a stable chemical species. The black arrows are short trajectories (on the time scale of τ_{rxn}) that define the basin of attraction. Trajectories that initiate in the basin of attraction for reactant or product do not pass through the dynamical bottleneck, but relax back to reactants or products (red dot) with high probability. The bottom panel is a cartoon of the dynamical bottleneck (blue dot). The outward arrows show trajectories relaxing to reactant and product basins, located in the directions specified by the red arrows. Short trajectories initiated at the dynamical bottleneck with random momenta commit to reactant or product basins with equal probability. The ensemble of configurations at the dynamical bottleneck comprise the transition state.

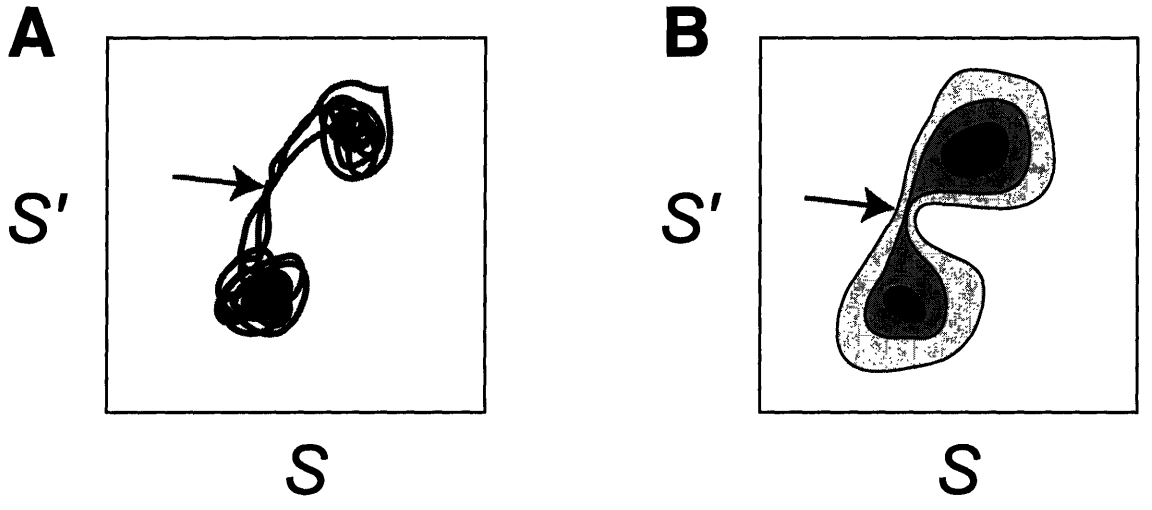

Figure 6-9: Basins of attraction and dynamical bottlenecks. **(A)** is a cartoon that illustrates a several reactive trajectories as a function of the S and S' reaction coordinates. The arrow shows the dynamical bottleneck trajectories pass in going between reactants and products. The trajectory density is high in the regions of the basins of attraction, but low in the region of the dynamical bottleneck, leading to the free energy landscape $F(S, S')$ diagramed in **(B)**. **(B)** The transition state is the point at the dynamical bottleneck. In energetically dominated dynamics there are only a few atomistic degrees of freedom that define the reaction coordinate: the basins of attraction correspond to collections of minima on the energy landscape and the transition state occurs at a saddle point.

other coordinates behave in the reduced space. The projection operator formalism of Mori and Zwanzig [36] provides a way to "project" out the irrelevant dynamics from the motion along the reaction coordinate in a reactive chemical system. The resulting equation is the generalized Langevin equation (GLE) where the extraneous degrees of freedom appear as random noise. For concreteness, let us describe reactive trajectories by their motions on the reaction coordinate, S. The total Hamiltonian for the reactive system is

$$\mathcal{H} = \mathcal{H}_r(P,S) + \mathcal{H}_b(\boldsymbol{r}^N, \boldsymbol{p}^N) + \mathcal{H}_{sb}(\boldsymbol{r}^N, S). \tag{6.13}$$

$\mathcal{H}_r(P,S)$ is the Hamiltonian of the pure reactive system, S is the reaction coordinate and P its conjugate momentum; $\mathcal{H}_b$ the Hamiltonian for the "bath", which in this case is the liquid in the absence of the reacting system; $\mathcal{H}_{sb}$ the coupling between the reactive system and the liquid.

Recall that dynamical variables obey the Liouville equation, and for the reaction coordinate

$$\boldsymbol{A} = \begin{pmatrix} P \\ \\ S \end{pmatrix}, \tag{6.14}$$

$$\frac{d\,\boldsymbol{A}(t)}{dt} = i\mathcal{L}\boldsymbol{A}(t). \tag{6.15}$$

The formal solution to 6.15 is $\boldsymbol{A}(t) = e^{i\mathcal{L}t}\boldsymbol{A}(0)$. While this solution is exact, it is useless without further manipulation. Because Equation 6.15 is a linear differential

equation, $\mathcal{L}$ is a Strum-Liouville operator whose vector space consists of all dynamical variables. The Mori-Zwanzig approach [36] uses projection operators in the space of the dynamic variables to eliminate the explicit functional dependence of the bath coordinates. Following standard procedures, [21, 25] we integrate out the bath variables by defining the projection operator $\mathcal{P}$, such that

$$g(\mathbf{\Gamma}) = \frac{e^{-\beta \mathcal{H}_b}}{Z_b}, \tag{6.16}$$

$$\mathcal{P}B = \int d\mathbf{\Gamma} e^{-\beta(\mathcal{H}_{sb} - w(R))} g(\mathbf{\Gamma}) B \tag{6.17}$$

where $d\mathbf{\Gamma}$ is shorthand for $d\boldsymbol{r}^N d\boldsymbol{p}^N$, Z_b is the partition function for the bath, and $w(R)$ is the potential of mean force, $e^{-\beta w(R)} = \int d\mathbf{\Gamma} g(\mathbf{\Gamma}) e^{-\beta \mathcal{H}_{sb}}$. Using the operator identity

$$e^{i\mathcal{L}(1-\mathcal{P})t} = e^{i\mathcal{L}t} + \int_0^t d\tau \, e^{i\mathcal{L}\tau} i\mathcal{P}\mathcal{L} e^{i(1-\mathcal{P})\mathcal{L}(t-\tau)} \tag{6.18}$$

yields the equations of motion

$$\frac{dS(t)}{dt} = \frac{P(t)}{M}, \tag{6.19}$$

$$\frac{dP(t)}{dt} = e^{i\mathcal{L}t} F - \int_0^t d\tau \, \xi(t-\tau) P(\tau) + \mathcal{F}(t), \tag{6.20}$$

here, $\mathcal{F}(t)$ is the "random force" $e^{(1-\mathcal{P})i\mathcal{L}t} F$, F is the deterministic force, $F = -\frac{d(w(S) - H_s(P,S))}{dS}$, and M is the mass. Because Equation 6.20 is a re-writing of the Liouville equation, it is still exact. The memory kernel satisfies the fluctuation dissipation theorem, $\xi(t) = \frac{\beta}{M} \langle \mathcal{F}(t) \mathcal{F}(0) \rangle$. The random force is orthogonal to $\boldsymbol{A}$ at all times, and represents the motion of dynamical variables orthogonal to $\boldsymbol{A}$.

When the reaction coordinate is an obvious choice, Equation 6.20 can be solved analytically by using a good approximation to the statistics of $\mathcal{F}(t)$, or equivalently, modeling the memory function. Kramer's theory solves for mean first passage times in 6.20 in the overdamped limit [36] and uses a Markovian model for the friction ($\xi(t) \propto \delta(t)$). Gröte-Hynes theory is a more detailed treatment that uses a harmonic approximation for F and solves self-consitently for the friction at the transition state in the high friction limit. Recently, Shental *et al.*[25] have developed an even more detailed treatment that uses a mixed kinetic and mode-coupling theory to model the memory kernel. Their results agree remarkably well with computer simulations of a model system at early and late times.

Equation 6.20 does not tell us what the reaction coordinate is, but only how how trajectories behave on it once it is chosen. If the reaction coordinate is "good", then trajectories on it yield the same statistics as those in a fully atomistic computer simulation. In the following section we generalize Eq. 6.20 to find a reduced description for the dynamics of ω_{OH}, the order parameter in the vibrational spectroscopy of water.

6.2 Reaction dynamics perspective of vibrational spectroscopy

We need to generalize equation 6.20 so that it is suitable for vibrational spectroscopy. Because the reduced equations of motion are in terms of S and P, we need to develop an analogous Hamiltonian to 6.13 where ω_{OH} plays the role of the coordinate, S.

ω_{OH} is an order parameter, and to make an analogy with Equation 6.20, we define an order parameter, x, with the dimensions of length by

$$x = x(\omega_{OH}), \tag{6.21}$$

$$x(\omega_{OH}) = m\,\omega_{OH} + b. \tag{6.22}$$

x is a linear function of ω_{OH}, specified by the slope (m) and intercept (b). Because x has units of length, we expect an accompanying conjugate momentum, p to x so that Hamilton's Equations are satisfied.

$$\frac{dx(t)}{dt} = \frac{p}{M}, \tag{6.23}$$

where M is the mass of the coordinate. We assume that the primary action of the other degrees of freedom is to keep the HOD molecule in thermal equilibrium. These "bath" modes interact with x and p. An simple model Hamiltonian for the system and the bath is

$$\mathcal{H} = \frac{p^2}{2M} + V(x) + \sum_i \left(\frac{1}{2}{p_i}^2 + \frac{1}{2}\omega_i^2 \left(q_i + \frac{\gamma_i}{\omega_i^2} x \right)^2 \right). \tag{6.24}$$

the indexed q_i and p_i are the mass weighted coordinates and momenta of the thermal bath and γ_i measures the strength of the coupling of the frequency to bath mode i. $V(x)$ is an empirical potential energy. The system remains in thermal equilibrium with the heat bath. By using Phillip Geissler's "favorite result of Gaussian statistics,"

[1]

$$\frac{1}{\sqrt{(2\pi)^N det(\boldsymbol{K}^{-1})}} \int d\boldsymbol{x}\, e^{\boldsymbol{a}^T \cdot \boldsymbol{x}} e^{-\frac{1}{2}\boldsymbol{x}^T \cdot \boldsymbol{K} \cdot \boldsymbol{x}} = e^{\frac{1}{2}\boldsymbol{a}^T \cdot \boldsymbol{K}^{-1} \cdot \boldsymbol{a}}, \tag{6.25}$$

the Canonical distribution function of x becomes

$$P(x) = \frac{e^{-\beta U(x)}}{Z}, \tag{6.26}$$

where Z is the partition function, and $U(x)$ is the potential of mean force, $U(x) = V(x)$. Indeed, Equation 6.26 immediately suggests a method to compute $U(x)$ from MD simulation. Solving Hamilton's equations with the Hamiltonian in Equation 6.24 yields the GLE for x and p, analogous to Equation 6.20

$$\frac{dx(t)}{dt} = \frac{p(t)}{M}, \tag{6.27}$$

$$\frac{dp(t)}{dt} = -\frac{dU(x)}{dx} - \int_0^t ds\, \xi(t-s)\frac{p(s)}{M} + \mathcal{F}(t), \tag{6.28}$$

where the memory kernel and random force have specific definitions in terms of the bath variables.

$$\xi(t) = \sum_j \left(\frac{\gamma_j}{\omega_j}\right)^2 \cos(\omega_j t). \tag{6.29}$$

A popular form of Equation 6.29 uses the "density of states," $g(\omega) = \sum_j \delta(\omega - \omega_j)$ to express 6.29 as a one sided cosine transform,

$$\xi(t) = \int_0^\infty d\omega\, g(\omega)\frac{\gamma(\omega)^2}{\omega^2}\cos(\omega t). \tag{6.30}$$

[1] Phillip Geissler, private communication

The interpretation of the memory kernel in Equation 6.29 is unchanged. It represents the motion of all degrees of freedom orthogonal to x. Analogous to the Markovian approximation used in Kramer's theory (Section 6.1.5), if we assume that all bath modes are spectators and do not influence the dynamics of ω_{OH}, the friction is Markovian.

$$\xi(t)_{\mathrm{Markovian}} = \Gamma\delta(t). \tag{6.31}$$

In Equation 6.31, Γ is the friction coefficient.

Simple and complex relaxation dynamics of $C_{\omega\omega}(t)$

If the correlation function $C_{\omega\omega}(t)$ is a single decaying exponential it is a signature of simple dynamics. One can easily show that the correlation function for $\langle x(t)x(0)\rangle$ from Equations 6.27 and 6.28 in the limit of a harmonic $U(x)$ and Markovian friction is a single exponential decay. When Γ is much larger than the frequency of the harmonic well the decay will be underdamped, but $\langle x(t)x(0)\rangle$ still decays exponentially. In the overdamped limit, $\langle x(t)x(0)\rangle \propto e^{-\frac{\Gamma}{M}t}$.

There are two sources that can give rise to a more complex $C_{\omega\omega}(t)$; an anharmonic potential of mean force, $U(x)$ and a non-Markovian friction kernel. A non-Markovian friction indicates that the bath modes are not merely spectators of the dynamics in x. Though analogous approximations to the memory kernel can be developed for Equation 6.29 that were discussed in Section 6.1.5, the physical interpretation is fuzzy. Though difficult to justify, we hope that the only other significant coordinate that interacts with ω_{OH} is the reaction coordinate, S. If this is the case, by observing

the dynamics of ω_{OH}, we can observe the important features of the potential of mean force $U(S, \omega_{OH})$ and distinguish between the stepwise and concerted mechanisms.

6.3 Reactive dynamics from spectral fluctuations of HOD in liquid D_2O

Analogies to transient hole burning experiments provide a route to relate spectral dynamics measured in an ultrafast experiment to changes in concentrations of HBs and NHBs. In transient hole burning experiments, One drives the system away from equilibrium and measures the change in the spectrum as the system returns back to equilibrium. For a linearly responding system, such a measurement can be related to the equilibrium frequency fluctuations, $C_{\omega\omega}(t)$. This relationship provides a convenient measure of dynamical nonlinearities in ω_{OH}. Section 6.3.1 describes how the time-dependent Stoke's shift introduced in this section can be used to interpret deviations from dynamic linearity and motivates the development of a model linear system, called the harmonic reference system. Section 6.3.2 describes spectral fluctuations in the idealized linear reference system in detail.

Dynamic linear systems in statistical mechanics obey the statistics of Gaussian fluctuations, while a nonlinear dynamical system does not. Section 6.3.3 uses the Central Limit Theorem to ellucidate why frequency fluctuations are not Gaussian for HOD in liquid D_2O. I show that if a spectroscopic measurement is designed to measure chemical reaction dynamics through frequency fluctuations, these fluctua-

tions should not be Gaussian. In Section 6.4.1 I perform numerical simulations the Generalized Langevin Equation developed for ω_{OH} to show that nonlinear ω_{OH} dynamics are not simply the product of an anharmonic potential of mean force. Indeed, these dynamics are more involved because they are coupled to the hydrogen bonding reaction coordinate in a complex way.

6.3.1 Transient hole-burning analogies

We need to formulate a way to analyze the statistics of vibrational frequencies and connect them to chemical dynamics on the reaction coordinate. A convenient measure of spectral dynamics is the time-dependent Stoke's shift, $S(T)$. In a hole burning experiment, the observer saturates part of the absorption spectrum with a pulse narrower than the absorption line and then measures the first moment of the hole as a function of the waiting time, T, as the spectrum returns to equilblirium. At $T = 0$, the laser burns a hole in the spectrum and there is a sudden perturbation to the Hamiltonian. Let $H_g = \langle g(\{\boldsymbol{r}\})|\mathcal{H}|g(\{\boldsymbol{r}\})\rangle$ be the expectation value of the vibrational Hamiltonian taken with respect to the adiabatic vibrational ground state and H_e the same quantity but for the first excited state ($\nu = 1$) (Chapter 2). The Hamiltonian as a function of time is,

$$H(t) = H_g + \epsilon\theta(t)(H_e - H_g), \tag{6.32}$$

where $\theta(t)$ is the heavy-side step function and ϵ measures the size of the perturbation. The transition frequency is $\omega_{\mathrm{OH}} = \frac{H_e - H_g}{\hbar}$. The hole burning experiment constructs

the time dependent Stokes shift, $S(T)$, defined by

$$S(T) = \frac{\overline{\omega_{\mathrm{OH}}(T)} - \overline{\omega_{\mathrm{OH}}(\infty)}}{\overline{\omega_{\mathrm{OH}}(0)} - \overline{\omega_{\mathrm{OH}}(\infty)}} \tag{6.33}$$

The quantal degrees of freedom have been averaged out, so classical linear response relates the time-dependent first moment of the hole, $\overline{\omega_{\mathrm{OH}}(t)}$ to the natural fluctuations of ω_{OH} at equilibrium [11].

$$\overline{\omega_{\mathrm{OH}}(T)} = \langle \omega_{\mathrm{OH}} \rangle + \epsilon \int_0^T dt' R(t') \theta(T - t') + O(\epsilon^2). \tag{6.34}$$

In Equation 6.34, the response function $R(t)$ is

$$R(t) = -\beta \theta(t) \frac{d\, C_{\omega\omega}(t)}{dt} \tag{6.35}$$

Equation 6.35 is called the second fluctuation dissipation theorem in statistical mechanics. The first appeared in Section 6.1.5. Using Equations 6.34 and 6.35, the time-dependent Stoke's shift is

$$S(T) = \frac{\langle \delta\, \omega_{\mathrm{OH}}(T) \delta\, \omega_{\mathrm{OH}}(0) \rangle}{\langle (\delta\, \omega_{\mathrm{OH}})^2 \rangle} + O(\epsilon^2), \tag{6.36}$$

6.3.2 The Harmonic reference system and hole-burning

Sometimes it is instructive to solve a problem in an exact model, where everything is analytically tractable. The "Harmonic reference system" is such a model. It is

obtained by replacing $U(x)$ with a Harmonic approximation. The Hamiltonian from 6.24 becomes

$$H_{ref} = \frac{p^2}{2M} + \frac{1}{2}M\Omega^2 x^2 + \sum_i \left(\frac{1}{2}{p_i}^2 + \frac{1}{2}\omega_i^2 \left(q_i + \frac{\gamma_i}{\omega_i^2} x \right)^2 \right). \tag{6.37}$$

where H_{ref} is the Hamiltonian of the harmonic reference system. Obviously, the equilibrium distribution function is a Gaussian in x. For this reason, the harmonic reference system is sometimes called a Gaussian reference system.

Because we are interested in the dynamics of frequencies, let us examine how the reference system responds to perturbations. Recalling that x is ω_{OH} with units of length (Equation 6.21), we can write the Hamiltonian for the hole-buring experiment (Equation 6.32) as,

$$H = H_{ref} - \epsilon\theta(t)x. \tag{6.38}$$

The non-equilibrium distribution function, $P_{neq}(\mathbf{\Gamma}, t)$ is useful for computing the time-dependent average of x. $P_{neq}(\mathbf{\Gamma}, t)$ obeys the Liouville Equation,

$$\frac{\partial P_{neq}(\mathbf{\Gamma}, t)}{\partial t} = (i\mathcal{L}_{ref} + i\mathcal{L}_\epsilon)\, P_{neq}(\mathbf{\Gamma}, t), \tag{6.39}$$

where $\mathcal{L}_{ref}$ is the Liouvillian for the reference system and $\mathcal{L}_\epsilon$ is the Liouvillian for the perturbation. The formal solution is

$$P_{neq}(\mathbf{\Gamma}, t) = e^{(i\mathcal{L}_{ref} + i\mathcal{L}_\epsilon)t} P_{eq}(\mathbf{\Gamma}), \tag{6.40}$$

where $P_{eq}(\mathbf{\Gamma})$ is the usual Canonical distribution function. Taking the Fourier-Laplace transform of 6.40 returns

$$P_{neq}(\mathbf{\Gamma}, z) = \frac{1}{z - i\mathcal{L}_{ref} - i\mathcal{L}_{\epsilon}} P_{eq}(\mathbf{\Gamma}), \tag{6.41}$$

which can be re-written as the Dyson Equation,

$$G^{-1}(z) = G^{-1}_{ref}(z) + G^{-1}_{ref}(z) V G^{-1}(z). \tag{6.42}$$

In Equation 6.42, $G^{-1}(z)$ is the Fourier-Laplace transform of the propagator $e^{i\mathcal{L}t}$ and $V = i\mathcal{L}_{\epsilon}$ is the perturbing operator. Iterate Equation 6.42 to achieve an expansion for $G^{-1}(z)$ in terms of ϵ.

$$P_{neq}(\mathbf{\Gamma}, z) = \frac{1}{z - i\mathcal{L}_{ref}} P_{eq}(\mathbf{\Gamma}) + \frac{1}{z - i\mathcal{L}_{ref}} i\mathcal{L}_{\epsilon} \frac{1}{z - i\mathcal{L}_{ref}} P_{eq}(\mathbf{\Gamma}) + O(\epsilon^2). \tag{6.43}$$

Using the explicit form of the Liouvillian for the reference system, it is straightforward to show that the series in 6.43 terminates exactly at first order in ϵ. Taking the inverse Fourier-Laplace transform, and then taking the average of x over the time-dependent distribution yields

$$\overline{x(t)} = \langle x \rangle + \int_0^t dt' \, R(t') \epsilon \theta(t - t'), \tag{6.44}$$

which is the linear response result. Equation 6.44 is a linear relationship between input ($\epsilon\theta(t - t')$) and output ($\overline{x}(t) - \langle x \rangle$), and is the definition of a dynamic linear

system [2]. In the harmonic reference system, we have the *identity*

$$S_{ref}(t) = \frac{\langle \delta x(t) \delta x(0) \rangle}{\langle (\delta x^2) \rangle} \tag{6.45}$$

$$\frac{\langle \delta x(t) \delta x(0) \rangle}{\langle (\delta x^2) \rangle} = \frac{C_{\omega\omega}(t)}{C_{\omega\omega}(0)}. \tag{6.46}$$

For HOD in D_2O (or any system for that matter), the deviations in $S(T)$ from the normalized correlation function are a measure of dynamical nonlinearity. The harmonic reference system shows that this nonlinearity emerges through the anharmonicities in the potential of mean force or from nonlinear coupling to bath modes, although this latter possibility has a more clouded physical interpretation.

6.3.3 Gaussian statistics and linear response

We have seen that a Harmonic reference system generates a Gaussian equilibrium distribution and that this system obeys linear response exactly. In Chapter 4, we treated the frequency fluctuations as if they were a Gaussian random variable. We justified this approximation *ex post facto*, by showing that it was one approximation in a series of simplifications that we could make and still have a good agreement between computer simulation and experiment for the IR3PEPS experiment. The assumption of Gaussian fluctuations made computing the spectroscopy simple, because with this approximation, $\boldsymbol{R}^{(3)}(\tau_1, T, \tau_3)$ only depends on the two point correlation function, $C_{\omega\omega}(t)$.

[2]The linear relationship is more apparent in Laplace space. Taking Laplace transforms, Equation 6.44 becomes $\overline{x(z)} - \langle x \rangle = R(z)\epsilon\theta(z)$. The "transfer function" is $R(z)$

Gaining physical insight into the non-Gaussian character of the distribution requires a bit of statistics. Consider a finite time series for the frequency ω_{OH}, by discretizing the time interval, t so that $t_i = i\delta t$, $i = 1 \cdots N$ and $\omega_{\mathrm{OH}}^{(i)} = \omega_{\mathrm{OH}}(t_i)$. Without loss of generality, examine the distribution of frequency shifts, $\delta_i = \omega_{\mathrm{OH}}^{(i)} - \langle \omega_{\mathrm{OH}} \rangle$. Now introduce some compact notion

$$\boldsymbol{\delta} = (\delta_1, \cdots, \delta_N)\,. \tag{6.47}$$

Each of the δ_i is a statistical degree of freedom. δ_i is the sum of contributions to the frequency shift from many molecules.

$$\delta_i = \frac{1}{N_{atoms}} \sum_{j=1}^{N_{atoms}} Y_j, \tag{6.48}$$

where Y_j is the frequency shift induced on HOD from atom j at time t_i. If the number of atoms inducing a frequency shift is large (here large is relative to the Law of Large Numbers [24]), the Central Limit Theorem applies. In this limit, the distribution of the $\{Y\}$ is irrelevant, and the joint probability distribution for $P(\boldsymbol{\delta})$ is a multivariate Gaussian distribution,

$$P(\boldsymbol{\delta}) = \frac{1}{2\pi^{N/2} det(\boldsymbol{C})^{1/2}} exp(-\frac{1}{2}\boldsymbol{\delta}^T \cdot \boldsymbol{C}^{-1} \cdot \boldsymbol{\delta}), \tag{6.49}$$

where $\boldsymbol{C}^{-1}$ is the inverse correlation matrix of the time series, and

$$\boldsymbol{C}_{ij} = \langle \delta\,\omega_{\mathrm{OH}}(t_i) \delta\,\omega_{\mathrm{OH}}(t_j) \rangle \tag{6.50}$$

is the correlation function evaluated at time $|t_i - t_j|$. The distribution of δ is obtained from Equation 6.49 by evaluating it for $\boldsymbol{\delta} = (\delta_1, \cdots, \delta_1)$, and is obviously Gaussian. The moment-generating function is the Fourier transform of $P(\boldsymbol{\delta})$.

$$P(\boldsymbol{k}) = \int d\boldsymbol{x} P(\boldsymbol{\delta}) e^{i\boldsymbol{k}\cdot\boldsymbol{\delta}}, \tag{6.51}$$

$$P(\boldsymbol{k}) = exp(-\frac{1}{2}\boldsymbol{k}^T \cdot \boldsymbol{C} \cdot \boldsymbol{k}). \tag{6.52}$$

Derivatives of the moment-generating function yield arbitrary correlations. For example,

$$\langle \prod_m \delta_m \rangle = \prod_m \left(\frac{1}{i}\right)^m \frac{\partial}{\partial k_m}|_{k_m=0} P(\boldsymbol{k}). \tag{6.53}$$

By inspection, all odd correlations of the distribution, (e.g. $\langle \delta_i \delta_j \delta_k \rangle$) are zero. Probability distributions are most conveniently expanded in terms of cumulants [24]. The logarithm of the moment generating function is the cumulant generating function, $\kappa(\boldsymbol{k})$ which terminates exactly at second order,

$$\kappa(\boldsymbol{k}) = -\frac{1}{2}\boldsymbol{k}^T \cdot \boldsymbol{C} \cdot \boldsymbol{k}. \tag{6.54}$$

Equation 6.54 shows that $\boldsymbol{C}$ is also the matrix of second cumulants.

All cumulants of order higher than two are identically zero in the limiting distribution. This fact greatly simplifies the calculation of $\boldsymbol{R}^{(3)}(\tau_1, T, \tau_3)$ because Wick's Theorem applies. Wick's Theorem is a combinatorial rule for factorizing cumulants of arbitrary order [24] that provides an exact resummation of an expansion because all higher order even moments are combinatorics of the correlation matrix (function).

Sung and Silbey [30], for example, use an equivalent theorem called the "Linked Diagram Theorem" that is a diagrammatic resummation of $\boldsymbol{R}^{(3)}(\tau_1, T, \tau_3)$ where the diagrams are cumulants of the propagator.

Familiar recipes based on Wick's theorem apply to calculating $\boldsymbol{R}^{(3)}(\tau_1, T, \tau_3)$ with the adiabatic scheme developed in Chapter 4. Because the quantal degrees of freedom are already averaged out, there is no concern about time ordering or operator commutation and $\boldsymbol{R}^{(3)}(\tau_1, T, \tau_3)$ can be obtained by direct expansion. For example, the rephasing response function for the $\langle 1| \leftarrow \langle 0|$ transition is (Chapter 2)

$$R_{\text{rephasing}}(t_1, t_2, t_3) = \langle exp(i \int_0^{t_1} dt' \, \omega_{\text{OH}}(t') - i \int_{t_1+T}^{t_1+T+t_3} dt' \, \omega_{\text{OH}}(t'))\rangle. \qquad (6.55)$$

In Equation 6.55, the brackets denote the average with respect to the equilibrium distribution function. The cumulant approximation of Equation 6.55 is obtained by expanding the argument of the exponential. In the harmonic reference system, cumulants higher than second order vanish identically, so the result is

$$R_{\text{rephasing}}(t_1, t_2, t_3)_{ref} = \qquad (6.56)$$
$$exp(i\langle \omega_{\text{OH}}\rangle(t_1 - t_3) - \frac{1}{2}\langle i \int_0^{t_1} dt' \delta\omega_{\text{OH}}(t') - i \int_{t_1+T}^{t_1+T+t_3} dt' \delta\omega_{\text{OH}}(t')\rangle_c),$$

where $\langle \cdots \rangle_c$ denotes the second cumulant of the quantity between the brackets.

Nonlinear frequency dynamics appear as asymmetric line shapes in the 2D IR spectrum. When $\boldsymbol{R}^{(3)}(\tau_1, T, \tau_3)$ is not the same as the result obtained by cumulant expansion, it is another indicator, directly measurable by experiment, that the

dynamics are non-Gaussian and nonlinear. A technical problem emerges when computing the vibrational response functions, $\boldsymbol{R}^{(3)}(\tau_1, T, \tau_3)$ because they do not factor into simpler functions of the two time correlation function, $C_{\omega\omega}(t)$. To compare with experiment the asymmetries of the line shapes are important and we must compute expressions like 6.55 by direct averaging.

In replacing the full distribution of $P(\boldsymbol{\delta})$ with the limiting Gaussian distribution, the Central Limit Theorem implied that the specific distribution of all the atoms that induced the frequency shift was irrelevant. In Chapter 4 we showed that the geometry of the hydrogen bonding partner has a profound impact on the value of the frequency shift. The electric field at the proton from the hydrogen bonding partner (E_0) accounted for the majority of the frequency shift. The statistics of the coordinates associated with E_0 prevent the limiting distribution from being realized. For this reason, the distribution of ω_{OH} in Figure 6-2 is not Gaussian. Intuitively, however, we expect the deviations from the Gaussian approximation to be most significant at short times, when the OH oscillator has not yet experienced the collective environment of the liquid.

6.4 Nonlinear dynamics of ω_{OH}

The linear response solution for $S(T)$ is independent of the initial selection interval of ω_{OH}. When the dynamics are nonlinear and the frequency fluctuations not Gaussian, the spectral response will depend upon the initial selection frequency. Figure 6-10 is the result from MD simulation for $S(T)$ computed with a frequency distribution

beginning on the blue side ($\omega_{\text{Blue}} > 3600\,\text{cm}^{-1}$) and on the red side ($\omega_{\text{Red}} < 3300\,\text{cm}^{-1}$) compared to the result for the idealized harmonic reference system. At the beginning of the simulation, all frequencies within either of these ranges were identified and those trajectories propagated forward in time to obtain the time dependent distribution functions,

$$P_{\text{Red}}(\omega_{\text{OH}}, T) = \int d\omega_0\, P(\omega_0) P(\omega_{\text{OH}}, T | \frac{\omega_0}{2\pi c} < 3300\,\text{cm}^{-1}), \tag{6.57}$$

$$P_{\text{Blue}}(\omega_{\text{OH}}, T) = \int d\omega_0\, P(\omega_0) P(\omega_{\text{OH}}, T | \frac{\omega_0}{2\pi c} > 3600\,\text{cm}^{-1}), \tag{6.58}$$

Where the distribution function $P(\Omega, T|\frac{\omega_0}{2\pi c} < 3300\,\text{cm}^{-1})$ is the conditional probability of having a value of $\Omega = \omega_{\text{OH}}$ at time T *given* that ω_{OH} was less than 3300 cm^{-1} at $T = 0$. $S(T)$ was calculated from

$$\omega_{\text{OH}}^{Red}(T) = \int d\,\omega_{\text{OH}}\, \omega_{\text{OH}} P_{\text{Red}}(\omega_{\text{OH}}, T), \tag{6.59}$$

$$\omega_{\text{OH}}^{Blue}(T) = \int d\,\omega_{\text{OH}}\, \omega_{\text{OH}} P_{\text{Blue}}(\omega_{\text{OH}}, T). \tag{6.60}$$

Indeed, the results of $S(T)$ do depend on the initial probability distribution. The difference between both curves for $S(T)$ and the result for the harmonic reference system are most pronounced at early times. This is consistent with the notions developed in Section 6.3.3 and also in Chapter 4. For $T < 200$ fs, the HOD molecule is still strongly interacting with the hydrogen bonding partner and has not yet sampled the collective liquid environment. When $T > 200$ fs, more molecules contribute to the frequency shift and the frequency fluctuations become more Gaussian.

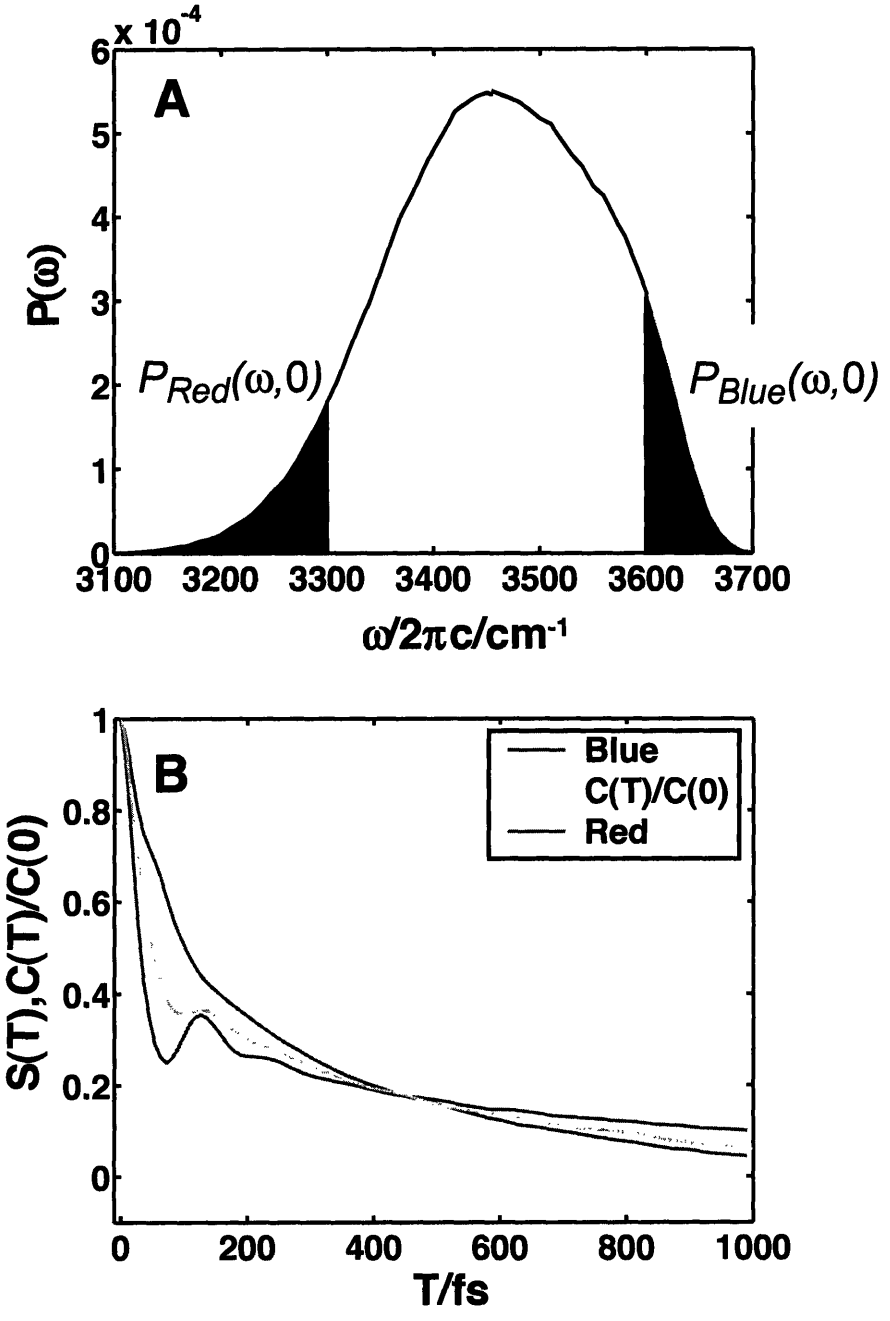

Figure 6-10: $S(T)$ for frequencies beginning on the extreme red and blue side and the comparison to the harmonic reference system. **(A)** is $P(\omega_{\mathrm{OH}})$ (black line) and shows the red and blue conditional probability distribution functions on the red and blue side. **(B)** The dynamics of ω_{OH} are nonlinear, but not dramatically nonlinear, as judged by the comparison to the harmonic reference system. The most pronounced differences are at early times ($T < 200$ fs), because on this time scale the HOD molecule has not yet explored the collective liquid environment.

Because the HOD molecule interacts with the hydrogen bonding partner in a specific way, we exploit this aspect of the problem with 2D IR spectroscopy to learn about hydrogen bonding dynamics from frequency shifts. Our arguments about the behavior of the frequency fluctuations in the limiting distribution described by the harmonic reference system are quite generic. Any spectroscopy designed to interrogate the dynamics of a chemical reaction should exhibit nonlinear frequency dynamics. The strength of coupling between the frequency and the reaction coordinate determines the extent of nonlinearity. The most popular approach for calculating nonlinear spectroscopies uses the cumulant approximation to $\boldsymbol{R}^{(3)}(\tau_1, T, \tau_3)$. This is an inappropriate approximation when one is interested in the dynamics of reactive systems, because the cumulant approximation discards all of the information about the coupling between the frequency and the reaction coordinate.

6.4.1 Brownian motion in the potential of mean force for ω_{OH}

We have seen that $S(T)$ is different on the red and blue sides of the line. We illustrated that one possibility where nonlinearities can appear is in the potential of mean force, $U(x)$. Might we be able to explain the nonlinear dynamics of ω_{OH} simply by an anharmonic potential of mean force?

If x evolves according to Brownian Dynamics, the finite difference solution to 6.27 and 6.28 advances x and p separately with a modified Velocity-Verlet algorithm [1] that acquires an additional stochastic term at each point in time for both x and p to

represent the dynamics the orthogonal coordinates of the bath induce. Fortunately, if we assume the bath modes are spectators, their correlations are Markovian, and we only treat x explicitly. The Velocity-Verlet algorithm is [1]

$$x(t+\delta t) = x(t) + c_1 \delta t v(t) + c_2 (\delta t)^2 \frac{F(t)}{M} + \delta x(t) \tag{6.61}$$

$$v(t+\delta t) = c_0 v(t) + (c_1 - c_2)\delta t \frac{F(t)}{M} + c_2 \frac{F(t+\delta t)}{M} \delta t + \delta v(t) \tag{6.62}$$

where $F(t) = -\frac{dU(x(t))}{dx(t)}$ is the deterministic force, $v(t)$ is the velocity at time t, δt is the stepsize, chosen to be small on the time scale of fluctuations judged by the size of the correlation time Γ^{-1}, and Gamma is determined from $\langle x(t)x(0)\rangle \propto e^{-\Gamma t}$, and $\delta x(t)$ and $\delta v(t)$ are random numbers chosen from a bimodal Gaussian distribution in x and v with a correlation coefficient $\rho_{x,v}$,

$$\rho_{x,v} = \delta t \frac{k_B \mathrm{T}}{M} (\Gamma \delta t)^{-1} (1 - e^{-\Gamma \delta t})^2. \tag{6.63}$$

$\rho_{x,v}$ is the correlation between x and v in phase space. The fluctuations in the two variables become uncorrelated as the mass of the coordinate M becomes very large. The coefficients are constants determined by the parameters Γ and δt,

$$c_0 = e^{-\Gamma \delta t}, \tag{6.64}$$

$$c_1 = (\Gamma \delta t)^{-1}(1 - c_0), \tag{6.65}$$

$$c_2 = (\Gamma \delta t)^{-1}(1 - c_1). \tag{6.66}$$

The order parameter x was defined by the slope, m, such that $x(3600\,\mathrm{cm}^{-1}) = +1$ and $x(3300\,\mathrm{cm}^{-1}) = -1$. I have chosen units where length and k_BT were unity and time was in fs. Γ was determined from the (approximate) short time constant of the decay of $C_{\omega\omega}(t)$ ($\Gamma = \frac{1}{50\mathrm{fs}}$). In these units, the mass is $M = 4.2809 \times 10^3$, and $\delta t = 1.0$ fs. To get arbitrary values for $U(x)$, I fit the PMF to a 10^{th} degree polynomial (Figure 6-11). I ran $\approx$ 1000 stochastic realizations of 1 ps duration trajectories of x. Averaging $x(T)$ over the realizations gave $\overline{x(T)}$ which I used to compute $S(T)$ from Equation 6.33.

Figure 6-12 shows the results from the Brownian Dynamics simulations. Indeed, these results are not even qualitatively comparable to those from the fully atomistic MD simulations. The beat on both the red and blue side is much stronger than in the MD simulation and occurs at a lower frequency ($\approx \frac{1}{200\ \mathrm{fs}}$). In the language of reaction dynamics, x is an order parameter, but it is not its own reaction coordinate. Nonlinearities in ω_{OH} cannot be explained from the evolution on an anharmonic potential of mean force.

6.5 2D IR spectroscopy of HOD in liquid D_2O

ω_{OH} is not its own reaction coordinate, but is coupled to the reaction coordinate for hydrogen bond breaking (Figure 6-13 A) or switching (Figure 6-13 B). The nature of this reaction coordinate will depend on which mechanism, stepwise or concerted, molecules undergo when trading hydrogen bonding partners. Conceptually, one could distinguish between the stepwise and concerted mechanistic possibilities by observing

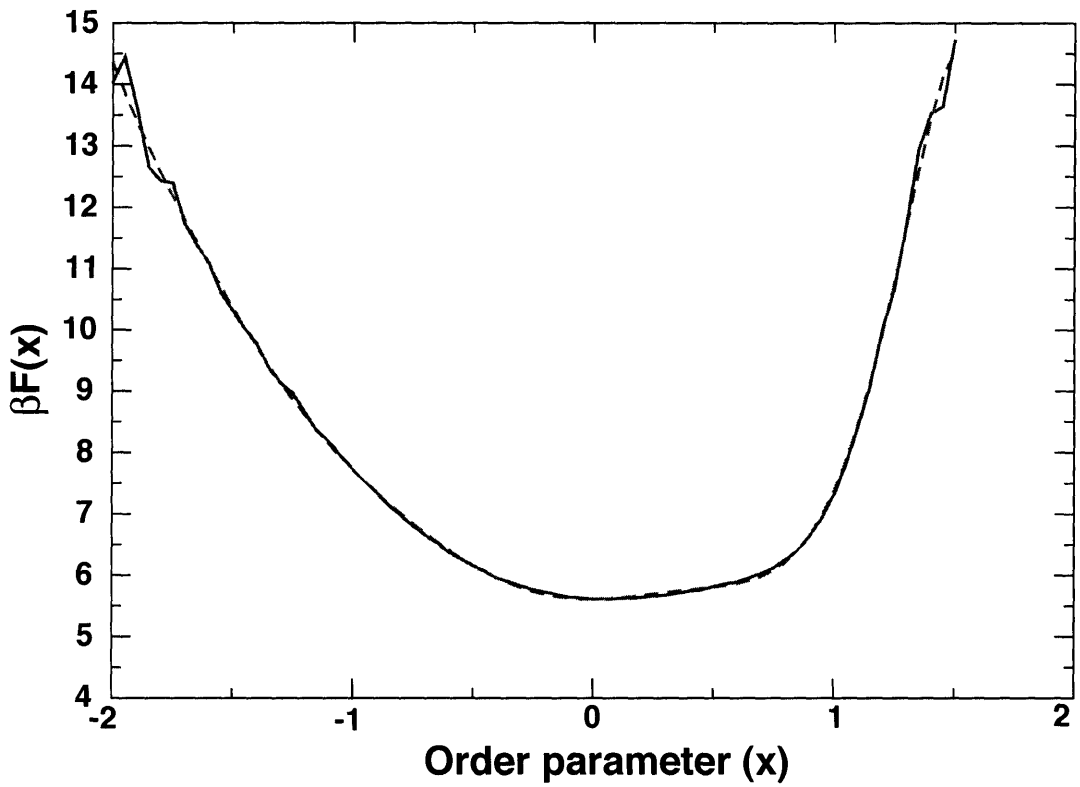

Figure 6-11: PMF for as a function of the frequency order parameter, x, and accompanying fit used in the Brownian Dynamics algorithm. The blue line is the PMF calculated from MD simulation and the dotted red line is the fit to a 10^{th} degree polynomial.

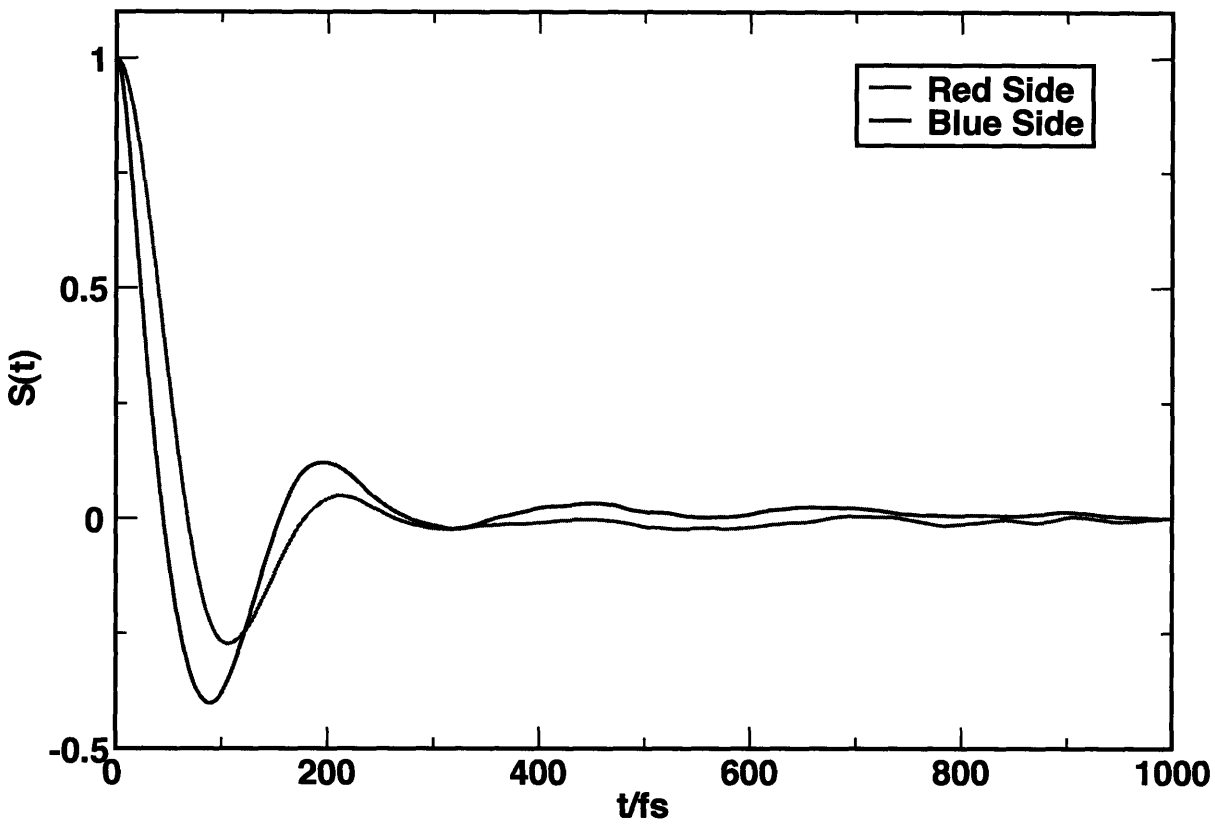

Figure 6-12: Time-dependent Stoke's shift, $S(t)$ calculated with Brownian Dynamics on the anharmonic PMF for x. The red and blue sides do not even qualitatively resemble the results from the fully atomistic MD simulation Figure 6-10. Therefore, x is not the reaction coordinate describing the dynamics of x.

how frequency distributions prepared in different regions of the free energy surfaces in Figures 6-13 and 6-13 evolve in time. The presence of a dynamical bottleneck between NHB and HB implies a separation of time scales for fast fluctuations within basins of attraction and for crossing the barrier between them. If this scenario were accurate, the persistence time of molecules prepared in the NHB state should exceed the time scale of intermolecular motions, τ_{mol}. On the other hand, if NHB species exist only as a transient fluctuation, molecules prepared on the blue side relax to line center on the time-scale of τ_{mol}. Basic intermolecular motions are librations (60 fs), hydrogen bond stretching (180 fs) and hydrogen bond bending (550 fs) [23, 10]. A reliable vibrational probe must remain coherent over these time scales. Our previous measurement of the time correlation function $C_{\omega\omega}(t)$, showed that the coherence time of ω_{OH} is 340 fs, longer than most intermolecular motions [18, 10].

Figures 6-2 and 6-13 show the quantitative connection between the populations of HB and NHB species as well as the equilibrium distribution of ω_{OH}, $P(\omega_{\mathrm{OH}})$, computed from MD simulation. Figures 6-13 A and B illustrate two possible scenarios consistent with the computed $P(\omega_{\mathrm{OH}})$. In Figure 6-13 A, a free energy barrier separates a metastable NHB state from the HB state [3]. 2D IR experiments are designed to distinguish spectral fluctuations of HB and NHB. If NHBs form a separate chemical species, they must be stable to thermal fluctuations so that ω_{OH} characteristic of NHBs remain in the blue region of the spectrum for times longer than characteristic intermolecular fluctuations, τ_{mol}.

2D IR spectroscopy probes the stability of NHB species by measuring the time-development of OH oscillators that initiate from HB and NHB environments. Analo-

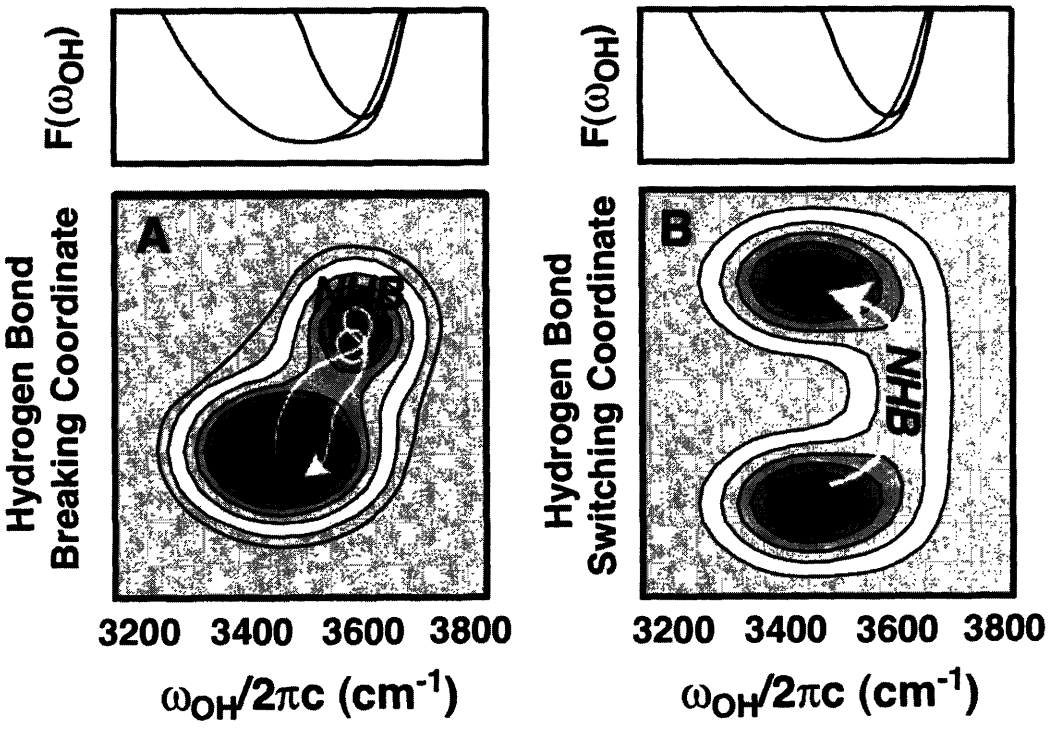

Figure 6-13: Free energy landscapes as a function of ω_{OH} and the hydrogen bond breaking (**A**) or switching reaction coordinates (**B**) corresponding to the stepwise and concerted pathways, respectively. 2D IR spectroscopy monitors trajectories of ω_{OH} (yellow lines). If a disordered liquid environment stabilizes NHBs ((**A**)), an initially HB molecule enters NHB and resides there before thermal agitation pushes it back over the barrier and into a hydrogen bond with another partner. In (**B**), NHB is not a stasble species but a transition state that trajectories pass through as they pass through as they switch hydrogen bonding partners. The top panel is the free energy as a function of ω_{OH}, which is identical for either mechanistic scenario.

gous to the correlation spectroscopy (COSY) experiment in NMR, 2D IR spectroscopy is a Fourier transform technique that uses an excitation sequence of femtosecond IR pulses with variable time delays. A 2D IR correlation spectrum, displayed as a function of two frequency axes (ω_1 and ω_3), is related to the conditional probability, $P(\omega_3, T|\omega_1)$, that given an initial excitation frequency ω_1, the target frequency ω_3 is observed after waiting a time T. The 2D IR line shape has both a positive peak from the fundamental transition ($|1\rangle \leftarrow |0\rangle$), and a negative peak from ($|2\rangle \leftarrow |1\rangle$) induced absorption.

More specifically, 2D IR spectroscopy measures the 2D line shape as a function of the waiting time, T. The contours of the 2D IR spectrum change as T increases because the frequencies shift as molecular environments evolve [14]. A distribution of absorption frequencies that is static during the T interval yields a diagonally elongated line shape (Fig. 6-14 A). When environments interconvert on a time scale much faster than T, the line shape for each resonance is symmetric with respect to reflection across the ω_1 and ω_3 axes (Fig. 6-14 B) [31].

$C_{\omega\omega}(t)$ shows both fast (50 fs) and slow dynamics (1.4 ps) [28, 35, 9, 2]. This system lies between the fast and slow limits Figs. 6-14 and B describe. The duration of the pulses determine the instrument response but not necessarily the time resolution of the measurement. Our pulses were fast enough (45 fs FWHM) to resolve the fastest spectral relaxations. Even so, the time resolution for the 2D IR experiment is not dictated by pulse length but by the time scales of spectral fluctuations. A finite time period $\Delta\tau$ is required to select a frequency resolution of width $\Delta\omega \approx \frac{2\pi}{\Delta\tau}$. $\Delta\tau$ defines the measurement time. The microscopic dynamics blur the transition frequencies

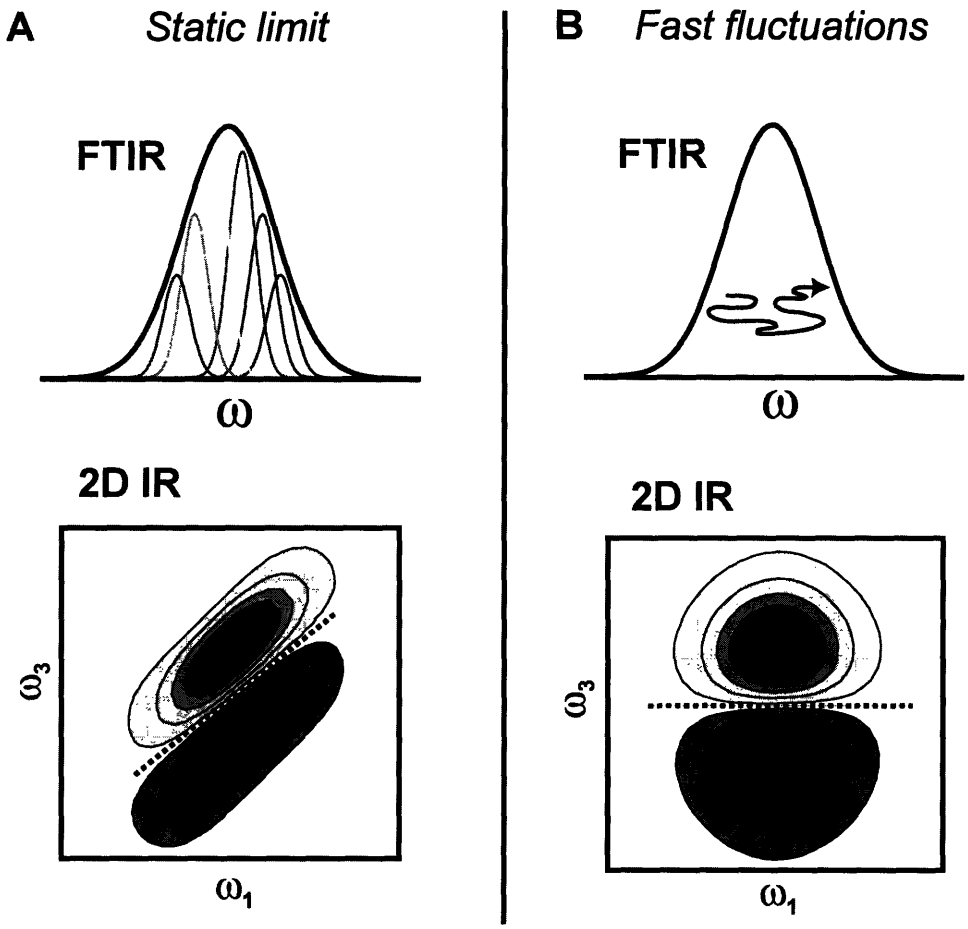

Figure 6-14: Cartoon of the 2D IR experiment in the fast and slow modulation limits. The dotted black line in both figures is the line of zero amplitude, or nodal line. The solid black line is the FTIR spectrum, which is nearly identical in either case. **(A)** is the limit where the frequency fluctuations are static on the time scale of the measurement, the frequencies in ω_3 will remain near where they were prepared initially along ω_1. The result is a line shape that is symmetric and elongated along the diagonal. The node between the fundamental and overtone peaks is parallel to the diagonal. In case **(B)**, the fluctuations are fast on the time scale of the measurement. Frequencies labeled in ω_1 migrate to the equilibrium distribution of ω_3, yielding a round line shape.

during $\Delta\tau$ so that the observation loses dynamic information over this interval. The shortest measurable time interval in a 2D IR experiment of the OH stretch of HOD in D_2O is $\approx$ 150 fs. This time is faster than all molecular motions except for librations.

Figure 6-15 A displays experimentally measured 2D IR spectra of the OH stretch of HOD in D_2O for a variety of waiting times. Even at early waiting times (T = 60 and 100 fs) that are smaller than typical intermolecular motions the spectra show discernible differences between the spectral shapes on the red and blue sides. Earlier waiting times are not shown because distortions in the signal arise from the nonresonant response of the D_2O when all pulses overlap. The line shape is broader towards the blue side of the line ($\frac{\omega_1}{2\pi c} > 3500\ cm^{-1}$) along the ω_3 and anti-diagonal axes than on the red side of the line ($\frac{\omega_1}{2\pi c} < 3300\ cm^{-1}$). Figure 6-15 C highlights the difference in the anti-diagonal widths with a plot of these slices from the red and blue side. The spectrum at T = 60 fs shows that even at small waiting times, frequencies beginning on the blue side have moved nearly back to band center. As T increases, both the red and blue sides of the line shape broaden as the frequencies travel back towards the center of the OH stretching band. The slope of the nodal line between the fundamental and overtone peaks during the T interval measures vibrational dephasing. The slope as a function of T agrees well with a calculation using our previously measured correlation function, $C_{\omega\omega}(t)$ (Fig. 6-15 D) [9].

MD simulations allow us to examine the microscopic origins of the 2D IR spectra in mechanistic detail [16, 17, 22, 9]. The simulation strategies we used to compute $C_{\omega\omega}(t)$ of an atomistic model in Chapter 4 [9] apply straightforwardly to calculations of 2D IR correlation spectra [8].

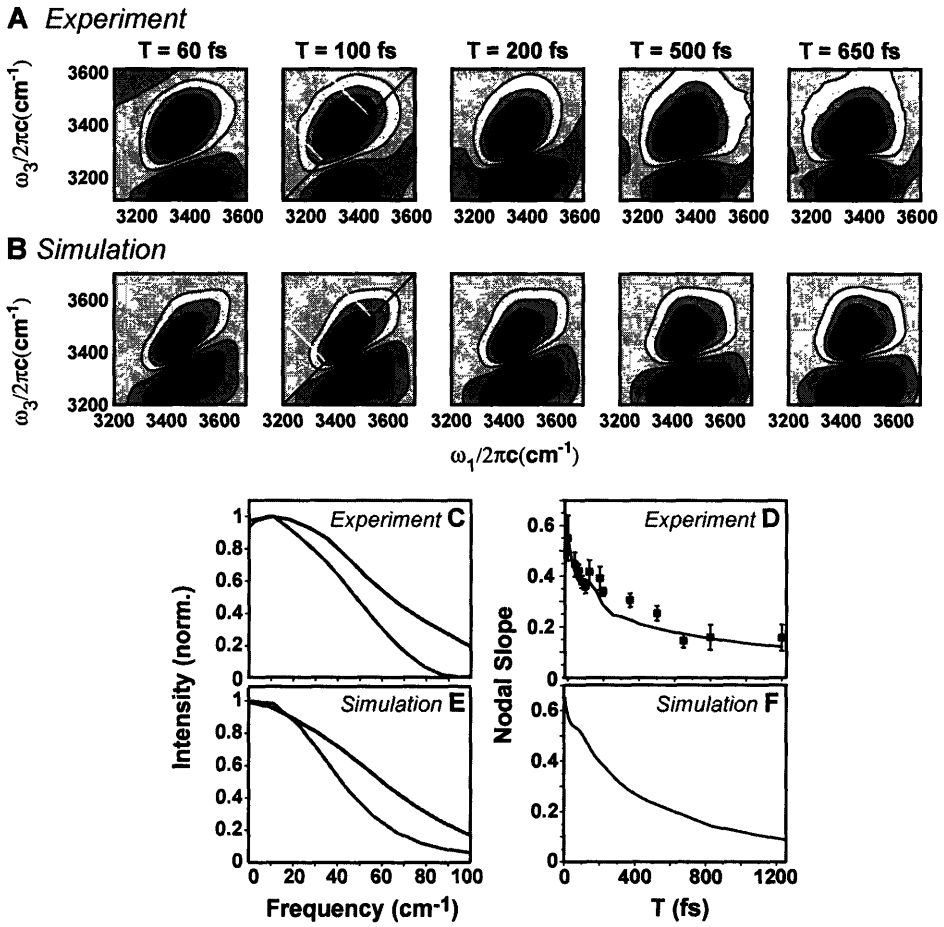

Figure 6-15: Comparison of experiment and simulation for the 2D IR spectra of HOD in liquid D_2O at a variety of waiting times. **(A,B)** 2D IR correlation spectra from experiments (20) compared to the 2D lineshape calculated from MD simulation for a variety of waiting times, T. The solid black line designates the diagonal axis ($\omega_1 = \omega_3$), and the white arrows orthogonal to it show where the anti-diagonal slices plotted in **C** and **E** were taken from the surfaces. Plots of the slope of the node between the fundamental and $\nu = |2\rangle \leftarrow |1\rangle$ for experiment **(D)** and simulation **(F)** as a function of waiting time, T. The slope of the node was calculated by fitting a straight line through the node of each surface between the limits $3250\,\mathrm{cm}^{-1} < \frac{\omega_1}{2\pi c} < 3450\,\mathrm{cm}^{-1}$. The squares in **D** are the experimental points and associated error bars. The solid line plotted along with the data in **D** is the predicted behavior using our previously measured $C_{\omega\omega}(t)$ [9, 10].

The 2D IR spectrum is a superposition of echo and grating phase matching directions. Within the Condon approximation, the response functions are

$$R_{\text{Rephasing}}(t_1, T, t_3) = \sum_{a,b,c,d} \langle e^{i\int_0^{t_1} dt' \omega_{ab}(t') - i\int_{t_1+T}^{t_1+T+t_3} dt' \omega_{cd}(t')} \rangle, \tag{6.67}$$

$$R_{\text{Nonrephasing}}(t_1, T, t_3) = \sum_{a,b,c,d} \langle e^{-i\int_0^{t_1} dt' \omega_{ab}(t') - i\int_{t_1+T}^{t_1+T+t_3} dt' \omega_{cd}(t')} \rangle. \tag{6.68}$$

Each term in the summand in Equations 6.67 and 6.68 is a double-sided Feynman diagram σ_u and a, b, c, and d are the resonant states of the diagrams consistent with the phase matching directions $\boldsymbol{k}_{\text{echo}} = -\boldsymbol{k}_1 + \boldsymbol{k}_2 + \boldsymbol{k}_3$ and $\boldsymbol{k}_{\text{grating}} = \boldsymbol{k}_1 - \boldsymbol{k}_2 + \boldsymbol{k}_3$, where the subscripts on the wavevectors denote the time ordering of the electric fields they represent. For reasons discussed in previous sections, Equations 6.67 and 6.68 must be computed by direct averaging in the simulation. When the pulse durations are short relative to the decay of R_{echo} and R_{grating} their temporal envelopes may be approximated by Dirac δ functions so that the 2D IR spectrum is

$$S_{\text{2D IR}}(\omega_1, T, \omega_3) \approx Real(R_{\text{Rephasing}}(-\omega_1, T, \omega_3)) + Real(R_{\text{Nonrephasing}}(\omega_1, T, \omega_3)), \tag{6.69}$$

The Fourier transform is of the rephasing response function, for example is

$$R_{\text{Rephasing}}(\omega_1, T, \omega_3) = \int_{-\infty}^{\infty} dt_1 \int_{-\infty}^{\infty} dt_3 e^{i\omega_1 t_1 + i\omega_3 t_3} R_{\text{Rephasing}}(t_1, T, t_3) \tag{6.70}$$

where ω_1 and ω_3 are the conjugate Fourier frequencies to time delays t_1 and t_3, respectively. The minus sign for ω_1 in Equation 6.69 cancels the sign difference

between the first term in the argument of the exponentials in Equations 6.67 and 6.68.

Computed line shapes, plotted in Fig. 6-15 A, closely resemble the corresponding experimental results in several key features. Most importantly, the blue side of the line shape broadens along the ω_3 axis more rapidly than the red side does. The anti-diagonal slices in Fig. 6-15 E, which compare particularly well with experiment, highlight this fact. The slope of the nodal line decays with a time dependence similar to $C_{\omega\omega}(t)$ (Fig. 6-15 F).

Time resolution in the computer simulation of 2D experiments is effectively unlimited, because ω_{OH} is simply a function of instantaneous atomic positions. Spectral dynamics can therefore be examined in greater detail. In particular, we can examine the full distribution $P(\omega_3, T|\omega_1)$ by propagating configurations for which ω_{OH} initially lies in a small interval around ω_1 [22]. To contrast the dynamics of high (blue) and low (red) frequency extremes of the 2D line shape we focused on two distributions of initial frequencies termed $P_{\mathrm{Red}}(\omega, T)$ and $P_{\mathrm{Blue}}(\omega, T)$ for the red and blue sides of the line, respectively. $P_{\mathrm{Red}}(\omega, T)$ begins with $\frac{\omega_{\mathrm{Red}}}{2\pi c c} < 3300\ \mathrm{cm}^{-1}$ while $P_{\mathrm{Blue}}(\omega, T)$ contains only $\frac{\omega_{\mathrm{Blue}}}{2\pi c} > 3600\ \mathrm{cm}^{-1}$ initially. These time dependent frequency distributions appear in Fig. 6-16. The shapes of these distributions as they approach equilibrium differ qualitatively. As anticipated from the 2D IR line shapes, $P_{\mathrm{Blue}}(\omega, T)$ broadens more rapidly than $P_{\mathrm{Red}}(\omega, T)$. The underdamped oscillation in $C_{\omega\omega}(t)$ from the hydrogen bond stretch is pronounced for $P_{\mathrm{Red}}(\omega, T)$ but absent in $P_{\mathrm{Blue}}(\omega, T)$. Instead, the blue distribution quickly moves into the red side with a long tail, while the weight of $P_{\mathrm{Blue}}(\omega, T)$ for frequencies greater than $3600\ \mathrm{cm}^{-1}$ decrease steadily.

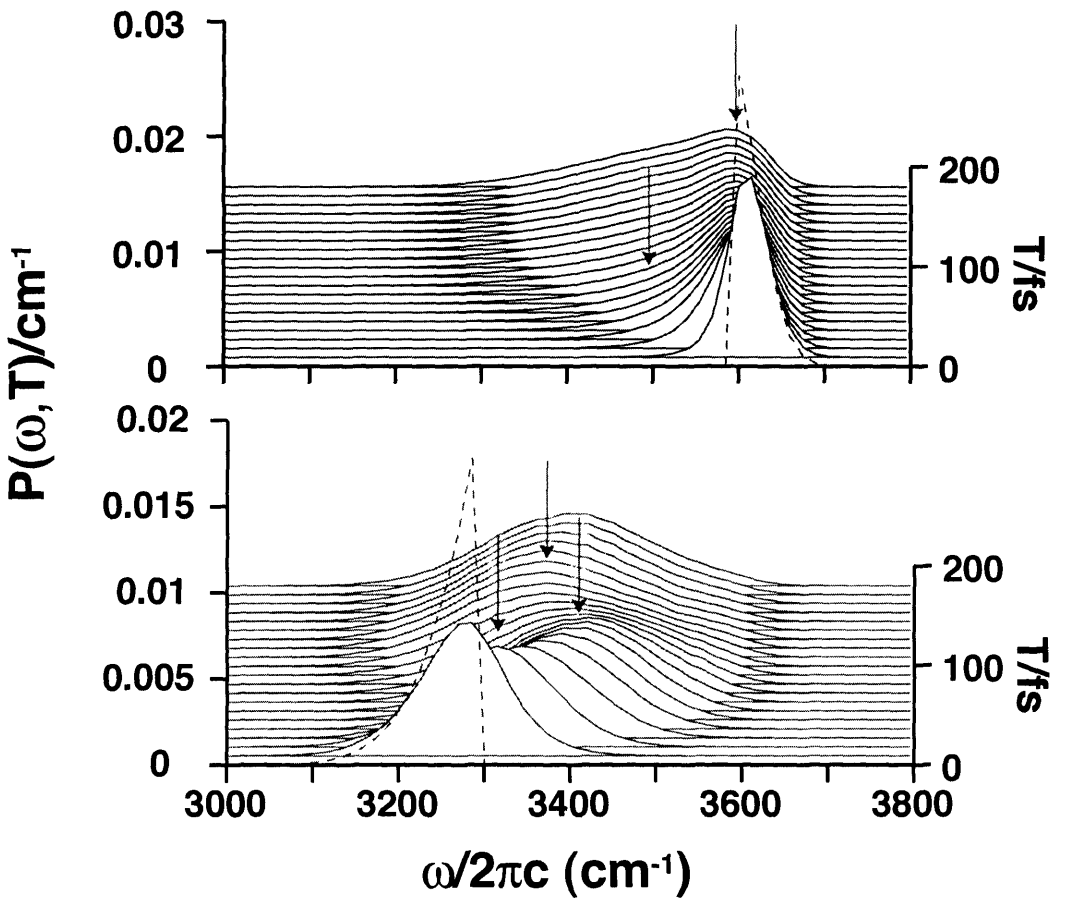

Figure 6-16: Time dependent probability distribution that originate on the red and blue sides of the spectrum. The black arrows draw attention to the salient features in the distribution functions. The dotted lines indicate the initial distribution at $T = 0$ fs. On the red side, the beat at $\approx$ 125 fs is apparent in the recoil of the frequency distribuiton. The width of this distribution widens prior to 200 fs, but remains relatively compact on the return to equilibrium. On the blue side, however, the distribution widens significantly at times prior even to 100 fs, indicating that there are a significant number of molecules that return to the hydrogen bonds rapidly.

In some respects the numerical results for the time-dependent distribution functions seems consistent with the scenario sketched in Fig. 6-13 B. One might infer that only intact hydrogen bonds have underdamped vibrational modes and that the growing tail of $P_{\text{Blue}}(\omega, T)$ and steady decrease of high frequency amplitude reflects passage over the free energy barrier separating HB and NHB species. The microscopic details accessible in molecular dynamics simulations allow us to determine the origins of computed spectral features directly. But to do so in terms of hydrogen bond dynamics, we must categorize HB and NHB species. The geometrical criteria provide conventionally accepted definitions of HB and NHB [20], and are useful for diagnosing the stability of NHB in either of the scenarios depicted in Figs. 6-13 B and 6-13 C.

If the NHBs comprise a metastable state, then short trajectories initiated from this state should remain in NHB with high probability. The putative dynamical bottleneck impeding hydrogen bond formation should become even more pronounced if we continuously remove kinetic energy from the system by quenching the system to a nearby local minimum of the potential energy surface as these trajectories evolve [8].

Running dynamics with zero velocity (quenching) finds the nearest local minimum in the multi-dimensional potential energy. When all the velocities are zero, the RATTLE algorithm for the dynamics becomes [1]

$$\boldsymbol{r}_i(t+\delta t) = \boldsymbol{r}_i(t) - \frac{\delta t^2}{2m_i}\left(\nabla_i V(\boldsymbol{r}_i, \cdots, \boldsymbol{r}_N) - \boldsymbol{g}_i\right). \tag{6.71}$$

In Equation 6.71 all of the $\boldsymbol{r}_i$ are the atomic positions, $V(\boldsymbol{r}_i, \cdots, \boldsymbol{r}_N)$ is the potential energy function, $\boldsymbol{g}_i$ is the force of constraint on atom i that keeps the bond lengths fixed and m_i is the mass of atom i. Equation 6.71 is a "steepest descent" algorithm that finds the closest minimum of the potential energy (i.e. where $\nabla_i V - \boldsymbol{g}_i = 0$ for all i), when the positions are "quenched," giving the condition

$$\boldsymbol{r}_i^*(t + \delta t) - \boldsymbol{r}_i^*(t) = 0. \tag{6.72}$$

The resulting collections of values, $\boldsymbol{R}^* = \{\boldsymbol{r}_1^*, \cdots, \boldsymbol{r}_N^*\}$, are configurations of the liquid that minimize the potential energy function. They are called the "inherent structures" of the liquid [6].

In the inherent structures from typical quenched equilibrium H_2O or D_2O configurations roughly 99 % of the molecules participate in four hydrogen bonds. These inherent structures do not have the long-range order of ice, demonstrating that even disordered liquid environments can accommodate a saturated network of hydrogen bonds. It follows that only a small fraction of NHBs maintain distances and angles characteristic of broken hydrogen bonds upon quenching. Figure 6-17 illustrates our quenching procedure for the high frequency distribution, $P_{\text{Blue}}(\omega, T = 0)$. Roughly 7 % of the equilibrium configurations begin with $\omega > \omega_{\text{Blue}}$. Of these 70 % begin NHB (Fig. 6-2 A), but only 10 % remain NHB after quenching. The remaining NHBs are not members of a separate metastable state, belonging instead to the basin of attraction of intact hydrogen bonds.

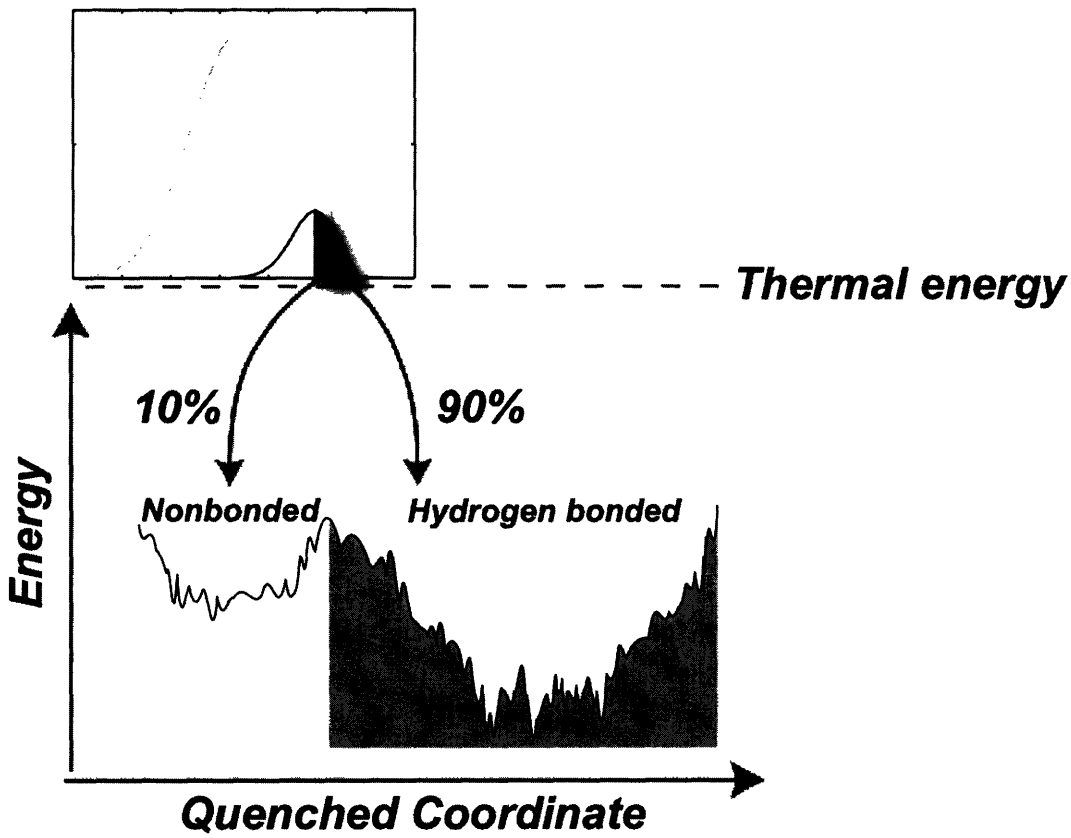

Figure 6-17: Quenching the blue distribution to the nearest inherent structure. The blue side of the distribution is only $\approx$ 7 % of the total population, and out of these only 10 % quench to NHBs.

	$\langle h \rangle$ at equilibrium	$\langle h \rangle$ for the inherent structures
Blue side	0.32	0.92
Entire Ensemble	0.89	> 0.99

Table 6.1: Hydrogen bond fractions ($\langle h \rangle$) at thermal equilibrium and among the inherent structures. The blue side corresponds to ≈ 7 % of the total population, those configurations with $\omega_{OH} > 3600$ cm^{-1}. The entire ensemble is the fraction of formed hydrogen bonds for all hydrogen bond possibilities (including $D_2O \cdots D_2O$ bonds).

We assert that the only stable broken hydrogen bonds are those NHBs that do not form hydrogen bonds upon quenching. A configuration in the basin of attraction for NHB should move even closer to that attractor upon quenching, and should certainly not convert to HB. The fates of NHB species at equilibrium (i.e., in unquenched dynamics) support this distinction, and validate the segregation into inherent structures. If entropy were an important factor for the reaction, the classification by inherent structures would fail to produce dynamics that behaved differently at equilibrium.

If a NHB at equilibrium is trapped inside the HB basin of attraction, it will become HB upon quenching. We have classified configurations with $\omega > \omega_{\text{Blue}}$ as either untrapped (NHB when quenched) or trapped (HB when quenched). Figure 6-18 shows the fraction of these two groups of configurations that are hydrogen bound as a function of time along equilibrium trajectories, along with the equilibrium fraction of hydrogen bonds (89 %). The stable group clearly persists as NHB over longer times. But even this rare collection decays quickly, with a rate of $\approx$ (200 fs)$^{-1}$. Broken hydrogen bonds that persist for 1 ps, approximately τ_{rxn} obtained in Section 6.1.2, or longer are indeed extremely rare.

A simple signature of a stable NHB species would be barriers in the order param-

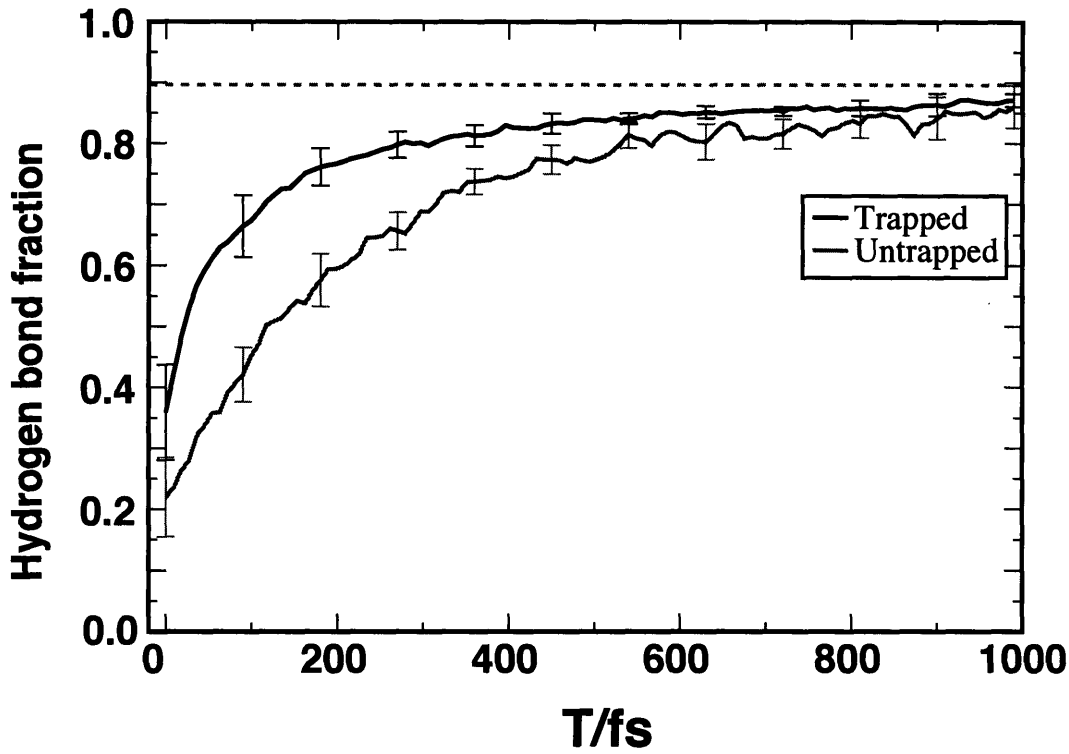

Figure 6-18: Equilibrium dynamics of untrapped (red line) and trapped (black line) configurations on the blue side of the line. When a thermal configuration belongs to the basin of attraction for NHB, is quenches to NHB but if it is confined to the HB basin then the quenching configuration is trapped in the HB basin of attraction. The dotted line is the equilibrium hydrogen bond fraction. Even the rare configurations that quench to NHB wells relax back to the equilibrium hydrogen bond fraction in 200 fs. The species that quench into HB relax back faster, with a rate of $\frac{1}{100\,\text{fs}}$. The designation by inherent structures is meaningful because entropy does not play a significant role. The difference between the equilibrium dynamics for trapped and untrapped configurations confirms this notion. It is likely that there are only a few degrees of freedom relevant to the hydrogen bonding state of one molecule.

eters that we presume can distinguish HB from HNB. These order parameters are the R_{OO} distance and hydrogen bonding angle $\cos(\alpha)$, the O$\cdots$H interatomic distance, and the potential energy of the dimer pair. Though the heights of the barriers may not be realistic and they may not occur at the presumed bottleneck, we the order parameters should not be orthogonal to the reaction coordinate. If NHBs are a stable chemical species, there should be some barriers in the free energy as a function of the order parameters.

First, consider the atomic pair radial distribution functions. The reversible work theorem relates the potential of mean force to the radial distribution function, $g_{ij}(r)$ [4].

$$exp(-\beta W_{ij}(r)) = g_{ij}(r). \tag{6.73}$$

In Equation 6.73, $W_{ij}(r)$ is the potential of mean force (PMF) – the reversible work required to separate atoms i and j by a distance r. It is also the free energy as a function of the separation distance, r between atoms i and j (see Equation 6.12. The radial distribution function is the density correlation function between atomic pairs i and j,

$$g_{ij}(\boldsymbol{r}_i, \boldsymbol{r}_j) = \langle \rho(\boldsymbol{r}_i)\rho(\boldsymbol{r}_j) \rangle. \tag{6.74}$$

In an isotropic fluid, $g_{ij}(\boldsymbol{r}_i, \boldsymbol{r}_j)$ depends only on the separation vector $r = |\boldsymbol{r}_i - \boldsymbol{r}_j|$. Figure 6-19 is a diagram of both the radial distribution function and the PMF for the interatomic O$\cdots$H distance for *all* pairs. The PMF displays a barrier roughly 2 k_BT at $r_{OH} \approx 2.45$Å. Some have suggested that a plausible cutoff to distinguish HB from NHB is at the maximum of the PMF, 2.45 Å[19].

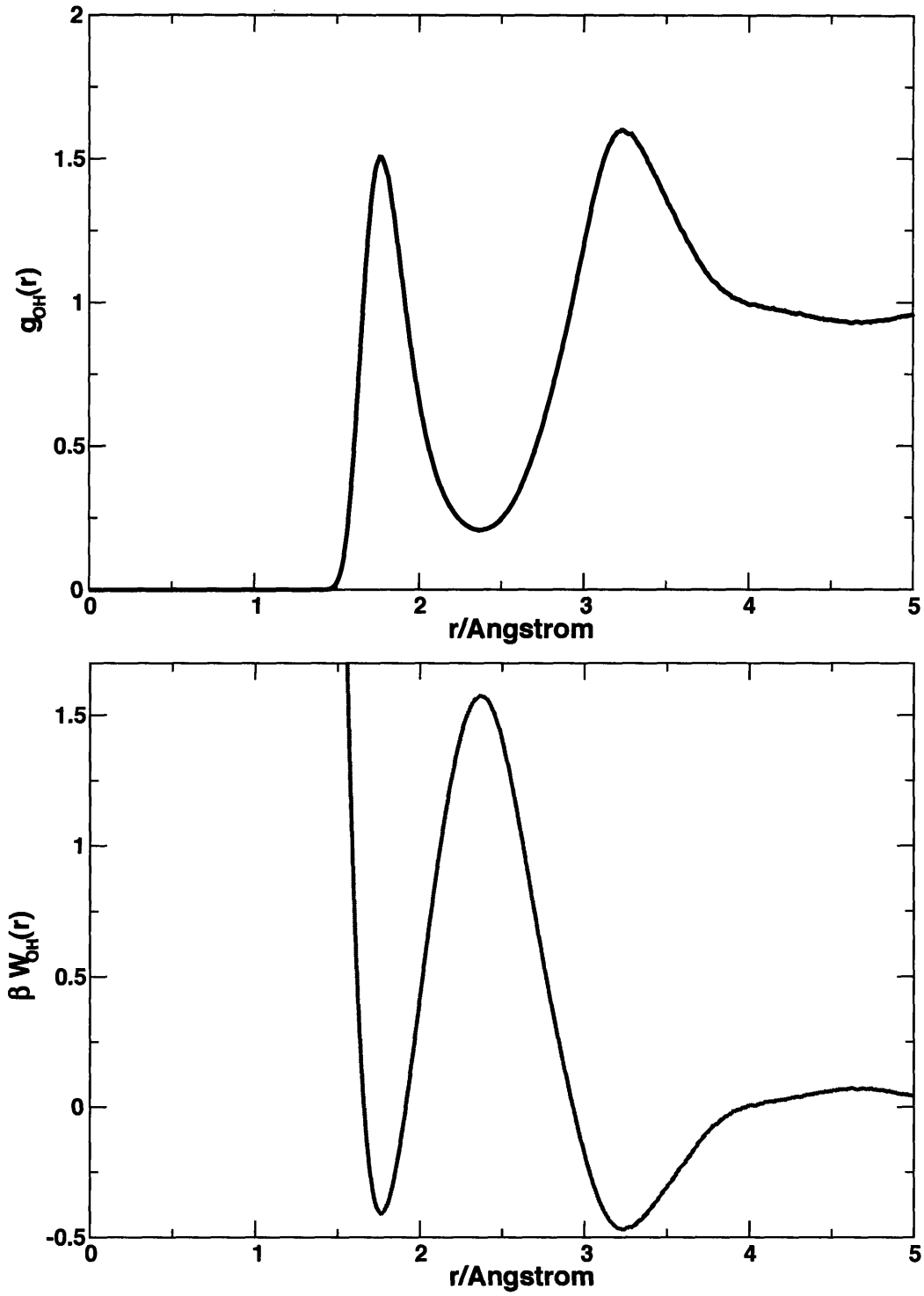

Figure 6-19: Radial distribution function and potential of mean force for the O$\cdots$H separation of all atomic pairs. There is an apparent barrier in the intermolecular O$\cdots$H coordinate.

Figure 6-20 is the the radial distribution function and PMF for the interatomic O$\cdots$O separation of all pairs. A reasonable criterion, and one that we adopt, is to place a cutoff on R_{OO} that restricts attention to HBs and NHBs within the first solvation shell, defined by the first minimum of $g_{OO}(r)$. This places the cutoff at R_{OO} = 3.5 Å[19].

The radial distribution functions are calculated for all pairs in the simulation and not restricted to only include the hydrogen bonding partner. Therefore, the PMF from $g_{OO}(r)$ is different than the free energy as a function of R_{OO}, the interatomic oxygen distance between the HOD molecule and *only* the hydrogen bonding partner. Figure shows the free energy as a function of O$\cdots$H if we only include the proximal hydrogen bonding partner. There is no free energy barrier in this coordinate. For every oxygen, there are two hydrogens on the same molecule. Comparing Figure 6-21 to Figure 6-19 shows that the apparent maximum in $W_{OH}(r)$ and second peak in $g_{OH}(r)$ corresponds to the distance between the oxygen of an accepting hydrogen bond and the hydrogen atom more distant than the one donating to this hydrogen bond. Indeed, the cutoff values for the intermolecular O$\cdots$H distance inferred from the radial distribution function appear misleading. The work of Csajka and Chandler [5] shows that the value of O$\cdots$H $\approx$ 2.25 Å would coincide more closely with dynamics of hydrogen bonds identified with the R_{OO} and $\cos(\alpha)$ criterion.

By only calculating the probability distribution function for the proximal hydrogen bonding partner, the potentials of mean force for R_{OO}, $\cos(\alpha)$ and the dimer potential energy V_{pair}, are obtained by applying Equation 6.12. Figure 6-23 is a diagram of the free energy as a function of R_{OO}, Figure 6-24 shows the free energy as a function

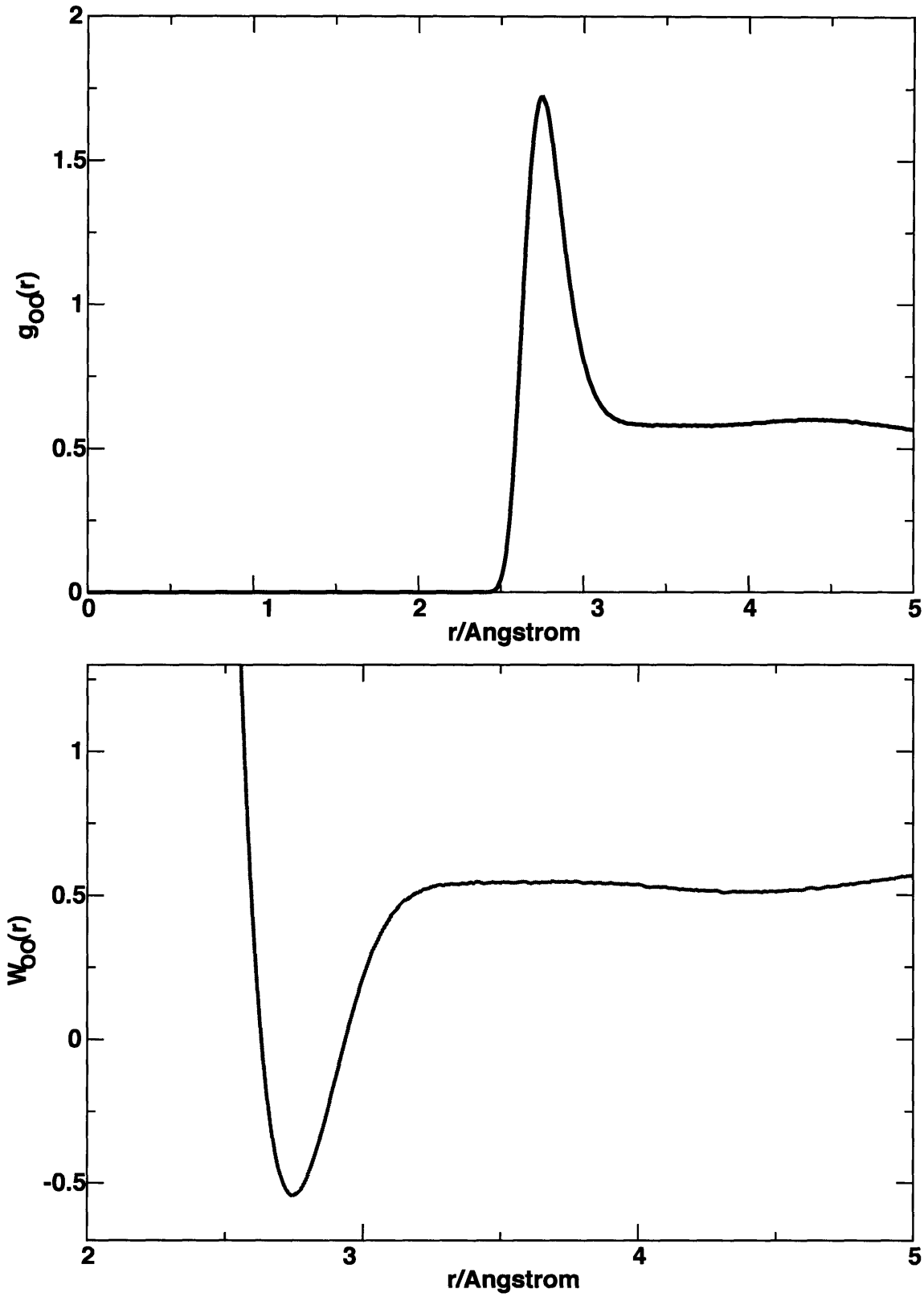

Figure 6-20: Radial distribution function and potential of mean force for the O$\cdots$O separation between all atomic O$\cdots$O pairs. There is a very modest barrier in $W_{\mathrm{OO}}(r)$ of $\approx 0.1\ k_B T$ at $r_{\mathrm{OO}} = 3.5$ Å.

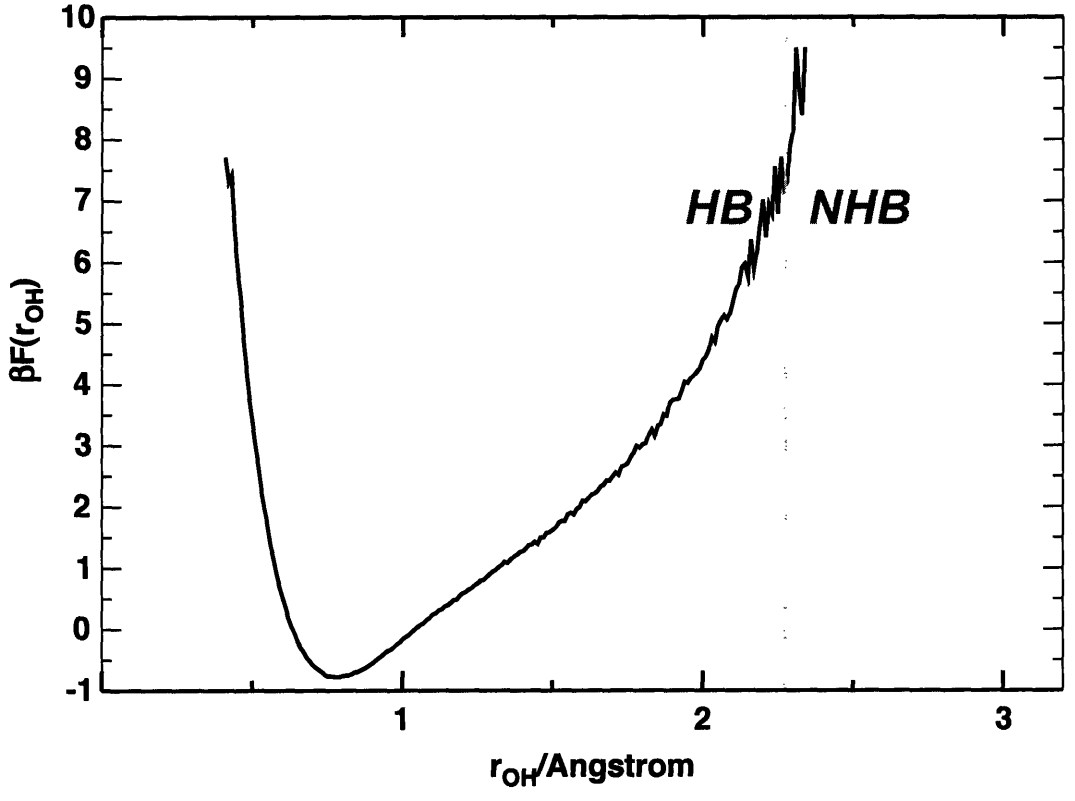

Figure 6-21: Free energy as a function of O$\cdots$H separation for only HOD and its proximal hydrogen bonding partner. Unlike Figure 6-19, it does not have a barrier. The barrier in Figure 6-19 is from the second hydrogen atom on a donating molecule. Thus, it represents the barrier to molecular rotation.

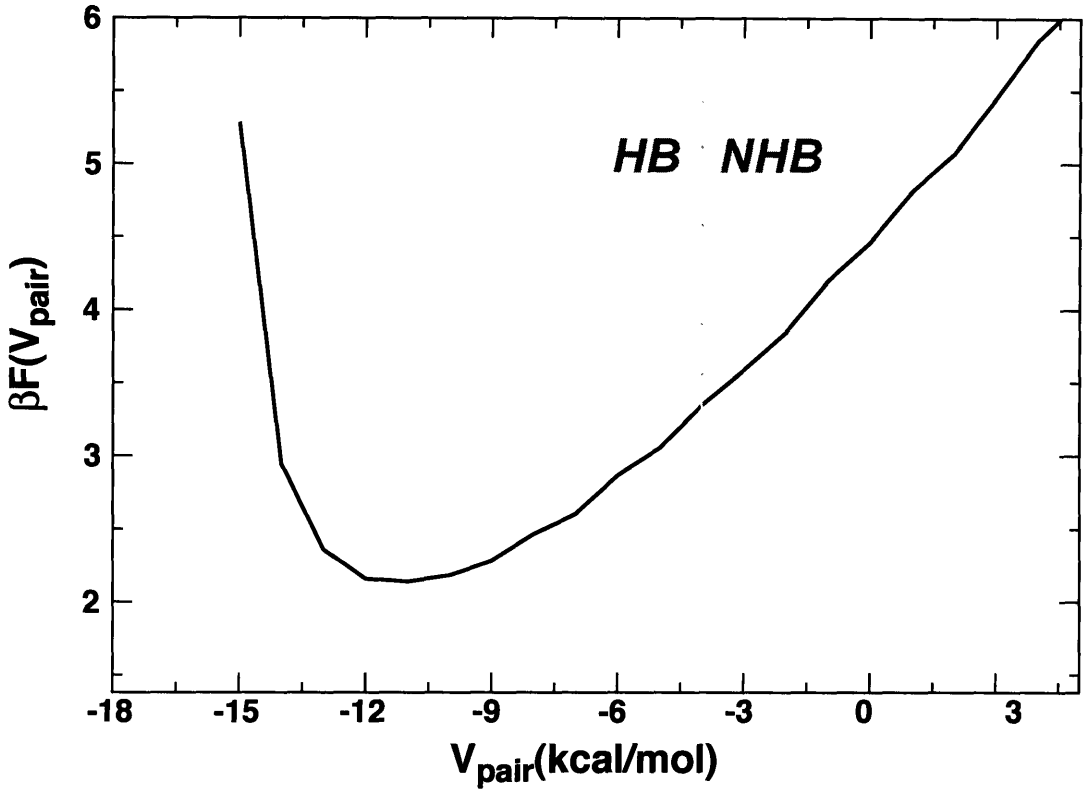

Figure 6-22: Free energy as a function of the pair potential energy between only HOD and it's proximal hydrogen bonding partner. There is no barrier in this coordinate.

of $\cos(\alpha)$, and Figure 6-22 is a graph of the free energy as a function of V_{pair}. None of these free energies exhibit a barrier, shedding doubt on the possibility that NHBs exist as chemically stable species.

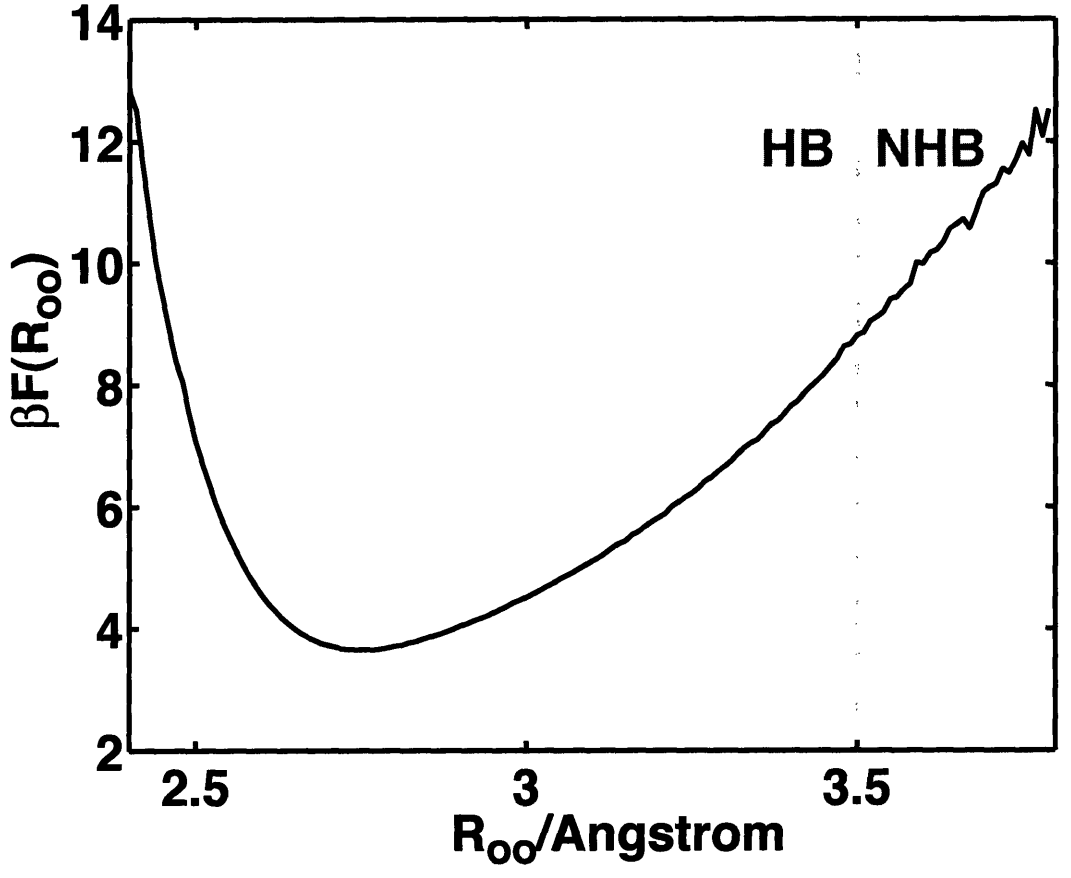

Figure 6-23: Free energy as a function of R_{OO} between only HOD and its proximal hydrogen bonding partner. The dotted line shows the critical value of R_{OO} conventionally used in conjunction with a cutoff in α to determine if a pair is bound or not.

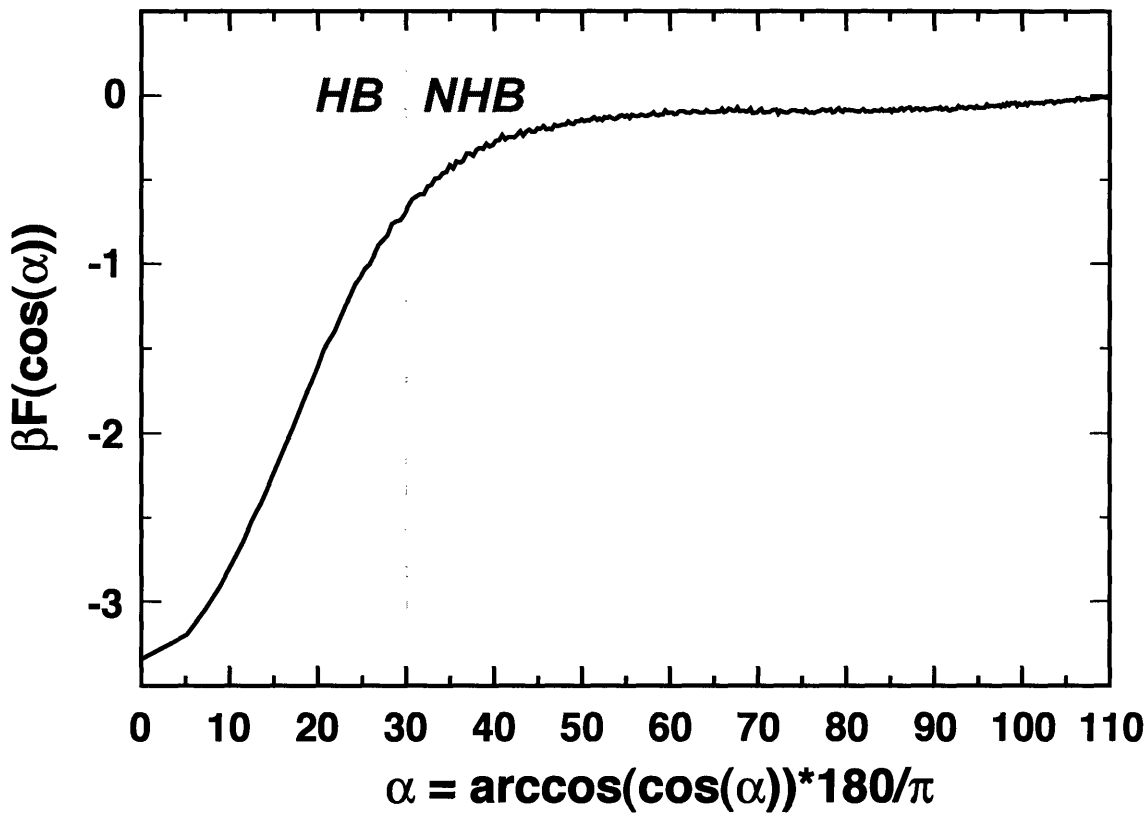

Figure 6-24: Free energy as a function of $\cos(\alpha)$ between only HOD and its proximal hydrogen bonding partner. The dotted line shows the critical value of $\alpha = 30°$ used in conjunction with a cutoff in R_{OO} to determine if a pair is bound or not by the geometric criterion.

6.6 Conclusions

When the absorption frequency is viewed as an order parameter, the methods of reaction dynamics developed to describe the statistics of biased random walks on reactive free energy landscapes apply straightforwardly to the vibrational spectroscopy of water. For HOD in D_2O, the OH absorption frequency, ω_{OH} is the order parameter. It can distinguish between HBs and NHBs with reasonable fidelity 6-2. In Section 6.4.1 we learned that it is not its own reaction coordinate. Chapter 4 and Section 6.3.3 showed that the specific interactions of HOD with its hydrogen bonding partner prevented the statistics of the fluctuations from reaching the limiting Gaussian distribution. These specific interactions made it impossible to even qualitatively describe the dynamics of ω_{OH} on an anharmonic PMF. The strong coupling between ω_{OH} and the hydrogen bonding coordinates is what the 2D IR spectroscopy exploits to measure hydrogen bonding dynamics in water. As such, popular second cumulant approximations for $\boldsymbol{R}^{(3)}(\tau_1, T, \tau_3)$ discard the very information the experiment is designed to measure. Recent experimental and theoretical work [27, 2, 16] that claims to measure hydrogen bond dynamics in water by focusing on $C_{\omega\omega}(t)$ should be re-examined.

Our findings illustrate a shortcoming in the analysis of hydrogen bond dynamics in water from MD simulations. MD simulations that use popular geometrical criteria fail to distinguish between configurations that quench into a HB and those that quench into an NHB. Figure 6-25 displays the distributions of $\cos(\alpha)$ and R_{OO} for the configurations with $\omega_{OH} > \omega_{Blue}$. Because there is significant overlap, there is no obvious pattern in the geometries between HOD and its nearest hydrogen bonding

partner that determines what the fate of a given hydrogen bond will be upon quenching. The $T = 0$ value in Figure 6-18 is the hydrogen bond fraction for configurations with $\omega_{OH} > \omega_{Blue}$. It is non zero for both trapped and untrapped configurations, indicating that some NHBs that remain NHBs when quenched, but also that some HBs quench into NHBs. It represents another failing of the standard geometric criteria to provide qualitative information about the hydrogen bond in water.

2D IR spectra measure dynamical nonlinearities of ω_{OH} in the asymmetry of the 2D line shapes. Our 2D IR data, as well as qualitatively similar data from Fayer and co-workers [27, 2], cannot be explained by a single transition whose frequency fluctuations obey Gaussian statistics. If the OH line shape is composed of two species corresponding to HB species on the red side and NHB species on the blue side, it is plausible that their fluctuations would be different and result in asymmetries in the 2D IR line shape. Empirical observations have shown that free OH resonances are much narrower than their hydrogen bound counterparts. In general, stronger hydrogen bonds are accompanied by a red shift and broader line width [28]. The rapid broadening of the 2D line shape on the blue side is inconsistent with the notion that NHBs experience small fluctuations within the NHB well, because frequencies initially on the blue edge appear throughout the line shape within a few hundred femtoseconds. Instead, the data support a picture where the NHBs form hydrogen bonds on the time scale of τ_{mol}. The short persistence time of these NHB species is consistent with Stillinger's description of hydrogen bond dynamics in water as a switching of allegiances [29]. Here strained or broken hydrogen bonds correspond to OH oscillators in the blue edge of the OH line shape. Intermolecular motions, likely

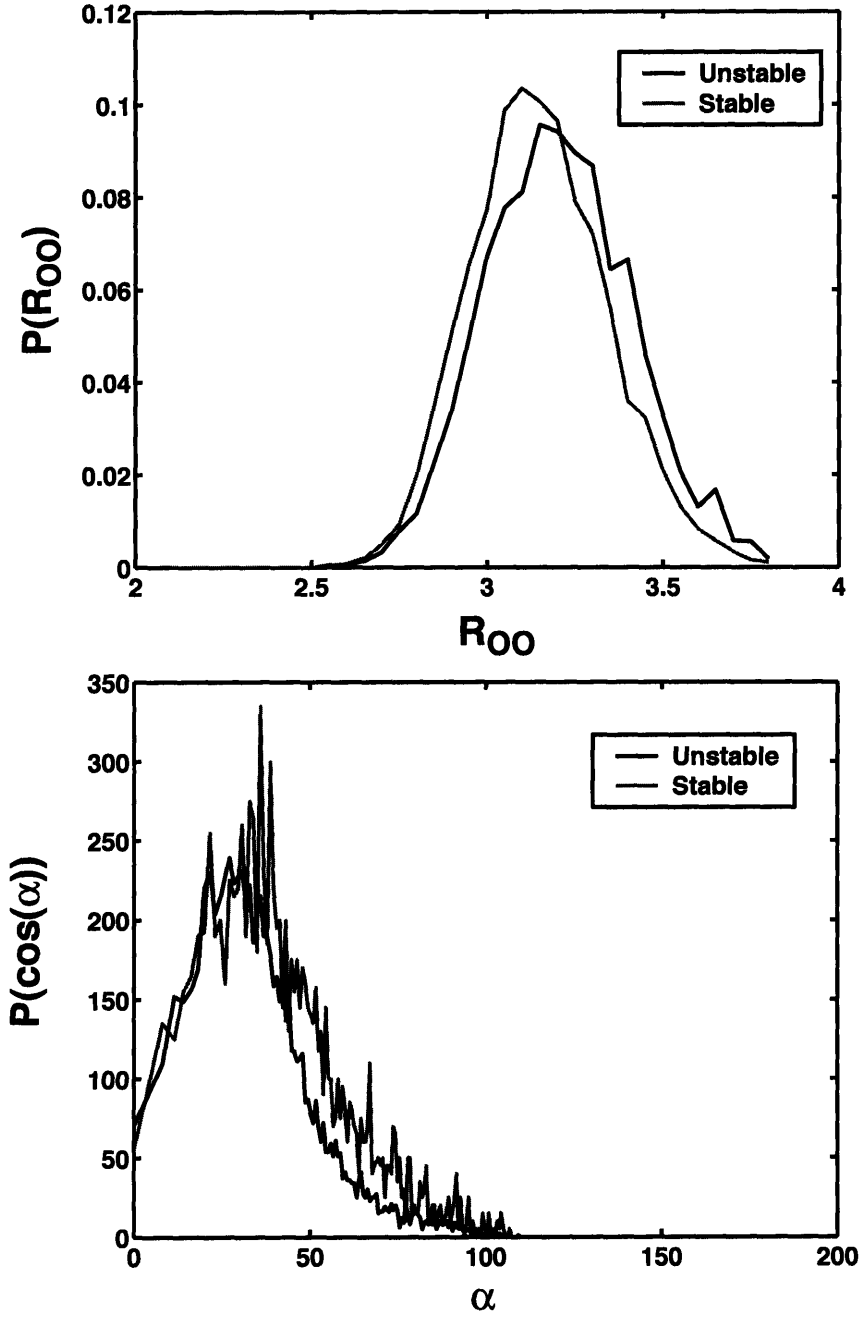

Figure 6-25: Distributions of geometrical order parameters for untrapped and trapped configurations at equilibrium. The two distributions overlap significantly so that there is no clear distinction based on either $\cos(\alpha)$ or R_{OO} that can successfully predict the fate of an equilibrium configuration upon quenching.

librations, may then push the oscillator into a new HB or back to the original HB. In either case the result is a red shift in ω_{OH} on the time scale of τ_{mol}.

The asymmetry in the 2D IR spectra reveals that the 2D line shape is composed of two initially distinct species with different microscopic dynamics. Decomposing spectroscopic line shapes into components that represent contributions from presumed molecular environments is a method of analysis prevalent in the spectroscopy of water. Although this method is tempting, our results underscore the danger of this approach. The most useful picture of hydrogen bond connectivity in water comes from measurements that observe spectroscopic signatures through the time scale of molecular fluctuations. In contrast, our results imply that NHB species identified in recent x-ray absorption experiments [32] relax back to band center on τ_{mol} and are intrinsically unstable.

Explicit microscopic information available in MD simulations allows us to examine the features in the 2D IR spectra in mechanistic detail. Our MD simulations show that neither the instantaneous geometric criteria for separating HB from NHB nor the value of the OH frequency can determine the stability of an assumed NHB. A typical configuration of the liquid has several instances of water molecules with apparently broken hydrogen bonds. In fact, these are just frequent excursions within the basin of attraction for hydrogen bound molecules. Previous MD studies using geometric criteria have found a weak relationship between the kinetics of hydrogen bond breaking and the number of hydrogen bonds with the donor and acceptor [20]. Conclusions derived from the two-state model, indeed many studies of hydrogen bond kinetics in water [20, 19, 34], attach a meaning to broken hydrogen bonds that should

be reconsidered. Though there are many specific definitions of hydrogen bonds, there are no free energy barriers in any of the order parameters used to make the distinction of NHB from HB. Quenching configurations before and after switching demonstrates that hydrogen bonds do reorganize in concert [23]. NHBs that persist for much longer than τ_{mol} are rare, and even these specimens find hydrogen bonding partners within $\approx$ 200 fs. For natural fluctuations at equilibrium, a broken hydrogen bond that is stabilized by liquid disorder appears to be more of a curiosity than a key player.

Acknowledgement

I thank Joe Loparo, Chris Fecko, and Sean Roberts for providing the experimental 2D IR data and for thoughtful discussions.

Bibliography

[1] M.P Allen and D.J. Tildesley. *Computer Simulation of Liquids.* Oxford University Press, 1989.

[2] John B. Asbury, Tobias Steinel, C. Stromberg, S. A. Corcelli, C. P. Lawrence, J. L. Skinner, and M. D. Fayer. Water dynamics: Vibrational echo correlation spectroscopy and comparison to molecular dynamics simulations. *Journal of Physical Chemistry A*, 108:1107–1119, 2004.

[3] Peter G. Bolhuis, David Chandler, Christoph Dellago, and Phillip L. Geissler. Transition path sampling: throwing ropes over rough mountain passes, in the dark. *Annual Review of Physical Chemistry*, 53:291–318, 2002.

[4] David Chandler. *Introduction to modern statistical mechanics.* Oxford University Press (New York), 1987.

[5] Felix S. Csajka and David. Chandler. Transition pathways in a many-body system: Application to hydrogen-bond breaking in water. *Journal of Chemical Physics*, 109:1125–1133, 1998.

[6] P.G. Debenedetti and F. H. Stillinger. Supercooled liquids and the glass transition. *Nature*, 410:259–267, 2001.

[7] Christopher Dellago, Peter G. Bolhuis, and Phillip L. Geissler. Transition path sampling. *Advances in Chemical Physics*, 123:1–78, 2002.

[8] J. D. Eaves, A. Tokmakoff, and P. Geissler. Electric field fluctuations drive vibrational dephasing in water. *In preparation*, 2004.

[9] C.J. Fecko, J.D. Eaves, J.J. Loparo, A. Tokmakoff, and P.L. Geissler. Local and collective hydrogen bond dynamics in the ultrafast vibrational spectroscopy of liquid water. *Science*, 301:1698–1702, 2003.

[10] C.J. Fecko, J.L. Loparo, S. R. Roberts, and A Tokmakoff. Submitted. *Journal of Chemical Physics*, 2004.

[11] G.R. Fleming and M. Cho. Chromophore-solvent dynamics. *Annu. Rev. Phys. Chem.*, 47:109–34, 1996.

[12] G. M. Gale, G. Gallot, F. Hache, N. Lascoux, S. Bratos, and J-Cl. Leicknam.

Femtosecond dynamics of hydrogen bonds in liquid water: A real time study. *Phys. Rev. Lett.*, page 1068, 1999.

[13] Phillip L. Geissler, Christoph Dellago, and David. Chandler. Kinetic pathways of ion pair dissociation in water. *Journal of Physical Chemistry B*, 103:3706–3710, 1999.

[14] J. D. Hybl, A. Yu, D. A. Farrow, and D. M. Jonas. Polar solvation dynamics in the femtosecond evolution of two-dimensional fourier transform spectra. *J. Phys. Chem. A*, 106(34):7651–7654, 2002.

[15] R. Laenen, C. Rauscher, and A. Laubereau. Dynamics of local substructures in water observed by ultrafast ir holeburning. *Phys. Rev. Lett.*, 80:2622–2625, 1998.

[16] C. P. Lawrence and J. L.. Skinner. Ultrafast infrared spectroscopy probes hydrogen-bonding dynamics in liquid water. *Chemical Physics Letters*, 369:472–477, 2003.

[17] C. P. Lawrence and J. L.. Skinner. Vibrational spectroscopy of hod in liquid d2o. iii. spectral diffusion, and hydrogen-bonding and rotational dynamics. *Journal of Chemical Physics*, 118:264–272, 2003.

[18] J. J. Loparo, C. J. Fecko, J. D. Eaves, S. T. Roberts, and A. Tokmakoff. Reorientational and configurational fluctuations in water observed on molecular length scales. *Physical Review B*, 2004.

[19] Alenka Luzar. Resoluving the hydrogen bond conundrum. *J. Chem. Phys.*, 113(23):10663–10675, 2000. And references therein.

[20] Alenka Luzar and David. Chandler. Hydrogen-bond kinetics in liquid water. *Nature (London)*, 379:55–7, 1996.

[21] P. Mazur and I. Oppenheim. Molecular theory of brownian motion. *Physica*, 50:241, 1970.

[22] K. B. Moller, R. Rey, and J. T. Hynes. Hydrogen bond dynamics in water and ultrafast infrared spectroscopy: A theoretical study. *J. Phys. Chem. A*, 108:1275–1289, 2004.

[23] I. Ohmine. Liquid water dynamics: Collective motions fluctuation and relaxation. *J. Phys. Chem.*, 99:6767, 1995.

[24] Linda E. Reichl. *A Modern Course in Statistical Physics.* John Wiley and Sons-Interscience, 2nd edition, 1992.

[25] Nurit Shental and Eran Rabani. Mode-coupling theory for reaction dynamics in liquids. *Journal of Chemical Physics*, 120(14):6642, 2004.

[26] Jon M. Sorenson, Greg Hura, Robert M. Glaeser, and Teresa Head-Gordon. What can x-ray scattering tell us about the radial distribution functions of water? *J. Chem. Phys.*, 113(20):9149, 2000.

[27] T. Steinel, J.B. Asbury, S.A. Corcelli, C.P. Lawrence, J.L. Skinner, and M.D. Fayer. Water dynamics: dependence on local structure probed with vibrational echo correlation spectroscopy. *Chem. Phys. Lett.*, 386:295–300, 2004.

[28] Jens Stenger, Dorte Madsen, Peter Hamm, Erik T. J. Nibbering, and Thomas

Elsaesser. A photon echo peak shift study of liquid water. *J. Phys. Chem. A*, 106(10):2341–2350, 2002.

[29] Frank H. Stillinger. Water revisited. *Science*, 209(4455):451–457, 1980.

[30] Jaeyoung Sung and R. J. Silbey. Four-wave mixing spectroscopy for a multi-level system. *J. Chem. Phys.*, 115:9266–9287, 2001.

[31] A. Tokmakoff. Two-dimensional vibrational lineshapes from third-order nonlinear spectroscopy. *J. Phys. Chem. A*, 104(18):4247–4255, 2000.

[32] P Wernet, D Nordlund, U Bergmann, M Cavalleri, M Odelius, H Ogasawara, LA Naslund, TK Hirsch, L Ojamae, P Glatzel, LGM Pettersson, and Nilsson A. The structure of the first coordination shell in liquid water. *Science*, 304(5673):995–999, May 14 2004.

[33] S. Woutersen, U. Emmerichs, and H.J. Bakker. Femtosecond mid-ir pump-probe spectroscopy of liquid water: evidence for a two-component structure. *Science*, 278:658–60, 1997.

[34] Huafeng Xu, Harry A. Stern, and B.J. Berne. Can water polarizability be ignored in hydrogen bond kinetics? *J. Phys. Chem. B*, 106:2054–2060, 2002.

[35] Sergey Yeremenko, Maxim S. Pshenichnikov, and Douwe A. Wiersma. Hydrogen-bond dynamics in water explored by heterodyne-detected photon echo. *Chem. Phys. Lett.*, 369:107–113, 2003.

[36] Robert Zwanzig. *Nonequilibrium statistical mechanics.* Oxford University Press (New York), 2001.

Appendix A

Appendix A

A.1 Expansions in internal coordinates

A practical problem emerges when computing the derivatives of the intermolecular potential in internal coordinates. Internal coordinates are functions of bond stretches and angles, for example. However, the intermolecular potential is a function of atomic Cartesian coordinates. More generically, internal coordinates are generalized coordinates that exclude overall translation and rotation of the molecule. Particular subtleties arise in the direct expansion when applying the chain rule of partial differentiation.

We illustrate the method employed to expand the hydride stretch coordinate to second order, but emphasize that the method is simple and general. Direct expansions are sometimes not applied even to simple systems [1, 3]. Instead, one finds the expansion numerically by evaluating the potential energy at several small displacements of the internal coordinate, gaining a more exact representation of H_{sb} at the expense of

computational efficiency. More importantly, it is much easier to analyze an analytical expression and determine which terms provide the largest perturbations than it is to backtrack through numerical computations. As long as the coupling between the vibration and the environment is a smoothly varying function, a low-order Taylor series approximation is sufficiently accurate. Direct expansion scales as $(M-1)O(N^2)$, where M is the desired expansion order. It can be applied to systems with many atomic degrees of freedom that define an internal vibrational coordinate. Including, but not limited to, small peptides and proteins in solution.

Begin with the derivative of the potential in internal coordinates. The potential is a function of atomic Cartesian coordinates, $V = V(\boldsymbol{r}_1, \cdots, \boldsymbol{r}_N)$. N is the number of atoms in the molecule. Let k be the number of equations of constraint. Because the equations that constrain the overall translation and rotation of the molecule are holonomic, the transformation equations between the atomic coordinates and generalized (internal) coordinates are

$$\begin{aligned} \mathbf{r}_1(t) &= \mathbf{r}_1(Q_1, \cdots, Q_{3N-k}; t), \\ &\vdots \\ \mathbf{r}_N(t) &= \mathbf{r}_N(Q_1, \cdots, Q_{3N-k}; t). \end{aligned} \tag{A.1}$$

We assume that these equations, along with the k equations of constraint are invertible (the Jacobian of the transformation in Equations A.1 is non-zero). We are interested in the derivative of the potential with respect to some internal coordinate Q_j. It is convenient to express the derivative operator by using the chain rule for partial

derivatives.

$$\frac{\partial}{\partial Q_j} = \sum_{i=1}^{N} \frac{\partial \boldsymbol{r}_i}{\partial Q_j} \cdot \nabla_i. \tag{A.2}$$

Applying the operator in Equation A.2 to the intermolecular potential provides an expansion in the set of Q_j to any order. If there is more than one generalized coordinate, H_{sb} is a multidimensional function whose expansion is facilitated by defining the operator,

$$D = \sum_{i=1}^{3N-k} Q_i \frac{\partial}{\partial Q_i}, \tag{A.3}$$

and writing

$$H_{sb}\left(Q_1, ..., Q_{3N-k}\right) = \sum_{j=1}^{M} D^j \frac{H_{sb}\left(Q_1, ..., Q_N\right)}{j!}, \tag{A.4}$$

where M is the desired order of the expansion and D^j is the operator in Equation A.3 raised to the jth power and upon expansion all of the Q_j in the derivatives are evaluated at their equilibrium values in Equation A.4.

We demonstrate this technique by solving for the hydride stretch and give expressions for F and G used in the computation. Recall that we wrote the system-bath Hamiltonian that couples the vibrations to the environment as $H_{sb} = FQ + GQ^2$, where Q and Q^2 are both operators in the system eigenstate basis. For a stretch, the constraint is that the center of mass of the vibration remains fixed. We write this constraint as $\boldsymbol{R}_{com} = \frac{r_H m_H + r_O m_O}{m_O + m_H}$. We use the constraint equation explicitly by shifting to the center of mass frame and writing the atomic positions relative to the

center of mass

$$\boldsymbol{r}'_H = -\frac{m_O}{m_O + m_H}\boldsymbol{r}, \tag{A.5}$$

$$\boldsymbol{r}'_O = \frac{m_H}{m_O + m_H}\boldsymbol{r}. \tag{A.6}$$

With these substitutions, it is easy to express the derivatives in Equation A.2. The result is

$$\frac{\partial}{\partial Q} = \mu\hat{\boldsymbol{r}}_{HO} \cdot \left(\frac{\nabla_H}{m_H} - \frac{\nabla_O}{m_O}\right), \tag{A.7}$$

where μ is the reduced mass and $\hat{\boldsymbol{r}}_{HO}$ is the unit vector pointing from the oxygen to the hydrogen. To generate the first term in the expansion, F, we apply the derivative operator to the potential.

$$F = -\mu\hat{\boldsymbol{r}}_{HO} \cdot \left(\frac{\boldsymbol{F}_H}{m_H} - \frac{\boldsymbol{F}_O}{m_O}\right), \tag{A.8}$$

where $\boldsymbol{F}_H$ is the force on the hydrogen (oxygen). Evaluating this term with the Velocity-Verlet algorithm is free because the atomic forces are available at each time step. The expression for F is the same one that Rey *et al.*[2] used in their study of the vibrations of the CN^- anion in water. Evaluating the second derivative, G, costs only $O(N^2)$, where evaluating H_{sb} for several values of Q costs $O(N^2)$ at each step. We write

$$G = \frac{1}{2}\frac{\partial^2 V}{\partial Q^2} = \frac{\mu^2 \boldsymbol{r}_{HO}\boldsymbol{r}_{HO}}{2} : \left(\frac{\nabla_O\nabla_O V}{m_O^2} - \frac{2\nabla_H\nabla_O V}{m_O m_H} + \frac{\nabla_H\nabla_H V}{m_H^2}\right), \tag{A.9}$$

where the : is the tensor contraction for the dyads on either side of the operator. Ewald summation of V partitions the sum over molecules and their periodic images by a pair-wise sum and a sum in reciprocal wavevector space, $V = V_{pair} + V_{\boldsymbol{k}}$.

$$V = \frac{1}{2}\sum_{i=1}^{N}\sum_{j=1}^{N}\phi(|\boldsymbol{r}_i - \boldsymbol{r}_j|) + \sum_{\boldsymbol{k}} A(k)|S(\boldsymbol{k})|^2, (i \neq j) \tag{A.10}$$

In the above, $S(\boldsymbol{k}) = \sum_l z_i e^{i\boldsymbol{k}\cdot\boldsymbol{r}_l}$ is the ionic structure factor, z_l is the charge of atom l, $A(k)$ is an amplitude, and $\phi(|\boldsymbol{r}_i - \boldsymbol{r}_j|)$ is the pair potential energy between atoms i and j. The double gradient operator on V contains three types of terms.

$$\nabla_\alpha \nabla_\beta V_{pair} = -\left(\phi''(r_{\alpha\beta})\,\boldsymbol{r}_{\alpha\beta}\boldsymbol{r}_{\alpha\beta} + \frac{\phi'(r_{\alpha\beta})}{r_{\alpha\beta}}(\mathbf{1} - \boldsymbol{r}_{\alpha\beta}\boldsymbol{r}_{\alpha\beta})\right), (\alpha \neq \beta) \tag{A.11}$$

$$\nabla_\alpha \nabla_\alpha V_{pair} = \sum_{\beta\neq\alpha}\left(\phi''(r_{\alpha\beta})\,\boldsymbol{r}_{\alpha\beta}\boldsymbol{r}_{\alpha\beta} + \frac{\phi'(r_{\alpha\beta})}{r_{\alpha\beta}}(\mathbf{1} - \boldsymbol{r}_{\alpha\beta}\boldsymbol{r}_{\alpha\beta})\right), \tag{A.12}$$

$$\nabla_\alpha \nabla_\beta V_{\boldsymbol{k}} = \sum_{\boldsymbol{k}} 2\boldsymbol{k}\boldsymbol{k}A(k)\left(Real\left(z_\alpha z_\beta e^{i\boldsymbol{k}\cdot\boldsymbol{r}_{\alpha\beta}} - z_\alpha\delta_{\alpha\beta}e^{i\boldsymbol{k}\cdot\boldsymbol{r}_\alpha}\right)\right) \tag{A.13}$$

Substituting A.13 in to A.9 yields the second term in the Taylor expansion for the intermolecular potential.

Bibliography

[1] K. Kwac and M. Cho. Molecular dynamics simulation study of n-methylacetamide in water I: Amide I mode frequency fluctuation. *J. Chem. Phys.*, 119(4):2247–2255, 2003.

[2] R. Rey and J. T. Hynes. Vibrational phase and energy relaxation of cn- in water.

J. Chem. Phys., 108:142, 1998.

[3] Rossend Rey, Klaus B. Moller, and James T.. Hynes. Hydrogen bond dynamics in water and ultrafast infrared spectroscopy. *Journal of Physical Chemistry A*, 106:11993–11996, 2002.

Bibliography

Joel D. Eaves
Department of Chemistry
Massachusetts Institute of Technology
77 Massachusetts Ave.
Room 6-030
Cambridge, MA 02139
email: joel@mit.edu
phone: 617-253-7372, fax: 617-253-7030

Education

2004 Ph. D. in physical chemistry, *Vibrational Dynamics in Water From the Molecule's Perspective*, Andrei Tokmakoff, advisor, Department of Chemistry, MIT, Cambridge, MA.

1999 B. S. in physics, University of Wisconsin – Madison, Madison, WI.

1999 B. S. in chemistry, University of Wisconsin – Madison, Madison, WI.

Teaching Experience

January 2004 Designed and taught a short course on computational techniques in physical sciences.

Fall and Spring semesters of 1999 Teaching assistant for 5.61 (Quantum Mechanics) and 5.62 (Statistical Mechanics).

Research Experience

Dec 2004 - present Postdoctoral research scientist with David Reichman, Department of Chemistry, Columbia University.

Summer 1999 - Nov 2004 Research assistant with Andrei Tokmakoff and Phillip Geissler, Chemistry Department, Massachusetts Institute of Technology:

- Designed and constructed ultrafast laser apparatus. Performed femtosecond spectroscopy experiments.
- Developed new computational strategies to explore the molecular origins of vibrational dephasing in water.

Fall 1997-Summer1999 Research assistant with Fleming Crim, Department of Chemistry, University of Wisconsin at Madison:

- Designed and performed high resolution gas phase spectroscopic experiments.

Summer 1997 Research Assistant, Gaea Technologies, Princeton University:

- Worked with Georgia Fisanick to develop a speckle interferometer useful for detecting minute fractures in structural elements of bridges and buildings.

Journal Publications

1. "Fluctuating charges and the vibrational spectroscopy of water," J.D. Eaves, E.D. Harder, A. Tokmakoff and B.J. Berne, *In preparation*, 2004.

2. "Electric fields drive vibrational dephasing in water," J.D. Eaves, A.Tokmakoff, and P.L. Geissler, *In preparation*, 2004.

3. "Hydrogen bonds in liquid water are broken only fleetingly, " J.D. Eaves, J. L. Loparo, C.J. Fecko, S.R. Roberts, A. Tokmakoff, and P.L. Geissler, *submitted, Nature*, 2004.

4. "Reorientational and configurational fluctuations in water observed on molecular length scales," J.J. Loparo, C.J. Fecko, J.D. Eaves and S.R. Roberts, *accepted, Phys. Rev. B*, 2004.

5. "Local and collective hydrogen bond dynamics in the ultrafast vibrational spectroscopy of liquid water," J.D. Eaves, C.J. Fecko, J.J. Loparo, A. Tokmakoff, and P.L. Geissler, *Science*, **301**, 1698–1702, 2003.

6. "Polarization-selective femtosecond Raman spectroscopy of low-frequency motions in hydrated protein films," J.D. Eaves, C.J. Fecko, A.L. Stevens, P. Peng, A. Tokmakoff *Chem. Phys. Lett.*, **376**, 20–25, 2003.

7. "Isotropic and anisotropic Raman scattering from molecular liquids measured by spatially-masked Kerr effect spectroscopy," C.J. Fecko, J.D. Eaves, and A. Tokmakoff, *J.C.P.*, **117**(3), 1139–1154, 2002.

Research Presentations

1. "Vibrational dynamics in water from the molecule's perspective," Coherent Multidimensional Vibrational Spectroscopy Conference, Madison, WI. (2004).

2. "Best poster talk," Gordon Research Conference on liquids, Plymouth, NH. (2003).

Awards

- MIT Departmental graduate fellowship (1999)
- Emille Fisher academic award in chemistry (1998)
- Hilldale fellowship for undergraduate research (1998)